The Dissertation Committee for Amir Hosseini Certifies that this is the approved version of the following dissertation:

Silicon Nanomembranes for Optical Phased Array (OPA) Applications

Committee:

Ray T. Chen, Supervisor

Seth Bank

Mikhail Belkin

Gennady Shvets

Andrea Alu

Silicon Nanomembranes for Optical Phased Array (OPA) Applications

by

Amir Hosseini, B.S.; M.S.

Dissertation

Presented to the Faculty of the Graduate School of

The University of Texas at Austin

in Partial Fulfillment

of the Requirements

for the Degree of

Doctor of Philosophy

The University of Texas at Austin

August, 2011

Dedication

Dedicated to the one only I know!

Acknowledgements

I would like to thank my advisor, Dr. Ray T. Chen, for his continuous support and guidance in my doctoral study. I will always be thankful for the opportunities he provided for me by the admission to his research group and the recognitions that would not be possible without his generous support. I also thank my committee members, Dr. Seth Bank, Dr. Mikhail Belkin, Dr. Gennady Shvets, and Dr. Andrea Alu for serving on the committee and advices on my dissertation.

I thank my colleagues in the Optical Interconnect Group at University of Texas at Austin, particularly David Kwong and Yang Zhang for their valuable collaborations and efforts in fabricating the photonic devices.

Finally, I would like to express my gratitude to my family for their love and support during and before my graduate studies. Special appreciations go to my mother for all the right decisions she helped me make.

Amir Hosseini

University of Texas at Austin

Austin, TX

Silicon Nanomembranes for Optical Phased Array (OPA) Applications

Amir Hosseini, Ph.D.

The University of Texas at Austin, 2011

Supervisor: Ray T. Chen

Theory, design, fabrication and characterization of on-chip optical beam steering systems are presented in this dissertation. Silicon photonics is being considered for integration with conventional CMOS technology for large-band width and low loss on and off-chip communications. We choose silicon nanomembrane, or silicon-on-insulator (SOI) substrates for implementation of large-angle and agile beam steeres. While working on the targeted device, we contributed to the theory, modeling, engineering and implementation of different building blocks.

Multimode-interference couplers (MMIs) constitute important parts of this dissertation. These devices are commonly used as on-chip beam splitters, optical switches and on-chip static phase shifters. The MMIs' principles of operation are suited in more details and design rules are derived for the first time. MMI based beam splitters with number of outputs as large as 12 are fabricated and tested on SOI wafers. Traditionally, MMIs devices were designed by means of computationally expensive numerical simulations. Numerically and experimentally, we show that our analytical design rules

make design of MMIs with low insertion loss and highly uniform outputs possible without additional optimization processes.

Optical phased arrays include phase shifter blocks. In the first prototype, we use micro-heaters for tuning the optical phase. The bread-loafing effect, which is generally considered an undeniable phenomenon in the silicon industry, is engineered to realize a mechanical structure to efficiently direct heat toward the silicon waveguides. We also investigate slow light photonic crystal based delay lines to be used as phase shifters. An important drawback of such devices is the low coupling efficiency between slow-light photonic crystal waveguides and fast light strip waveguides. We numerically and experimentally investigate the coupling efficiency, and show for the first time that a few-period long fast-light photonic crystal waveguide without any group index tapering suffices for efficient coupling.

The prototype is fabricated, packaged and tested and optical beam steering angle over ±30degrees is demonstrated. Finally, preliminary investigations for 3D implementation of the beam steerer system are presented to clarify the approaches to take for future works.

Table of Contents

List of Figures

List of Tables

Chapter 1: Project Framework and Research Goals

My thesis will report the results of my research in the framework of a Multidisciplinary University Research Initiative (MURI) program titled as "Three Dimensionally Interconnected Silicon Nanomembranes for Optical Phased Array (OPA) and Optical True Time Delay (TTD) Applications". Two major goals for employing silicon nanomembranes in this program are:

1. Formation of an optical phased array (OPA) for laser beam steering
2. Formation of optical true time delay (TTD) lines for phased array antenna

The project involves several research groups from four universities led by our group, Professor Ray Chen's Optical Interconnect Group. The full results of this project will be realized by the collaboration of several researchers. Thank to Prof. Chen, I have been able to get evolved in several other projects, such as slow light in photonic crystal waveguides and photonic device transfer on flexible substrate (please refer to the list of publications). However, my dissertation will be focused on on-chip large angle beam steering. This dissertation will report the results, which are primarily my contributions. In order to integrate my works, I will briefly mention other contributions of my teammates by explicitly referring to them.

This thesis proposal reports my 2-year research results, including a two-dimensional large angle ($>30^{\circ}$) optical beam steering system design for silicon nanomembrane-based implementation, fabrication and characterization of the beam steering device, and the

work that will be completed in next year. This chapter introduces the project, provides some background information and set the project goals.

Optical Phased Array for Optical Beam Steering

Optical beam steering systems started by mechanical beam directing and stabilization mechanisms. However, despite the accumulated technology in this field, mechanical beam steering for optical sensor systems and laser radar remains complex and expensive. In addition to have limited scanning speed (~KHz), such systems are incapable of rapid random pointing [1]. Optical phased arrays (OPAs) represent an enabling technology that makes possible simple, affordable, and lightweight laser beam steering with very precise stabilization, random-access pointing and programmable multiple simultaneous beams. OPA-based optical beam steering systems were first implemented using nematic crystal (LC) cells pioneered by Paul McManamon [1]-[3]. In Chapter 2, I discuss the limitations of LC OPAs with detailed explanations and the necessity of OPA implementation based on single mode waveguide arrays for both fast (~GHz) and large angle (>60°) steering. Figure 1.1 summarizes recently demonstrated single-staged OPA based optical beam steering systems performance in terms of maximum steering angle.

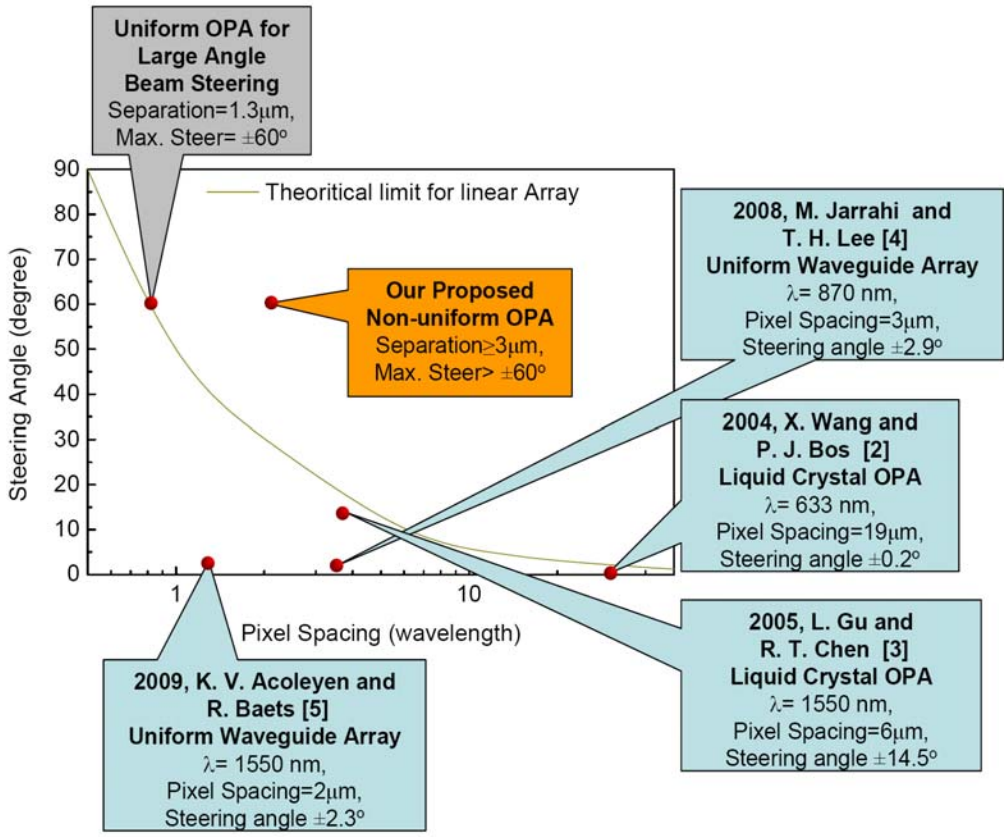

Fig. 1.1, Maximum steering angle and center-to-center pixel spacing for various recent OPAs and the proposed OPA.

Optical phased waveguide arrays (OPWA) are other implementation for OPA devices [4], [5]. In both cases of LC OPAs and OPWAs there is a theoretical limit for linearly phased uniform arrays. Figure 2.1 shows a schematic of a uniform phased array of K identical radiating elements uniformly spaced with a distance d between adjacent elements. In general, each element i is fed by a signal of amplitude and phase a_i and ψ_i, respectively. However, in the case of OPAs, due to the limitations for precise control of the amplitudes, all elements are fed by the same amplitudes, $a_1=a_2...=a_K$. If the input phase values ψ_i are given by

$$\phi_i = k_0(K-i)d\sin(\theta) \tag{1}$$

where, $k_0 = 2\pi/\lambda_0$, λ_0 is the free space wavelength, the result of interference of all the array elements' radiation form a wavefront propagating at an angle θ with the normal to the antenna array.

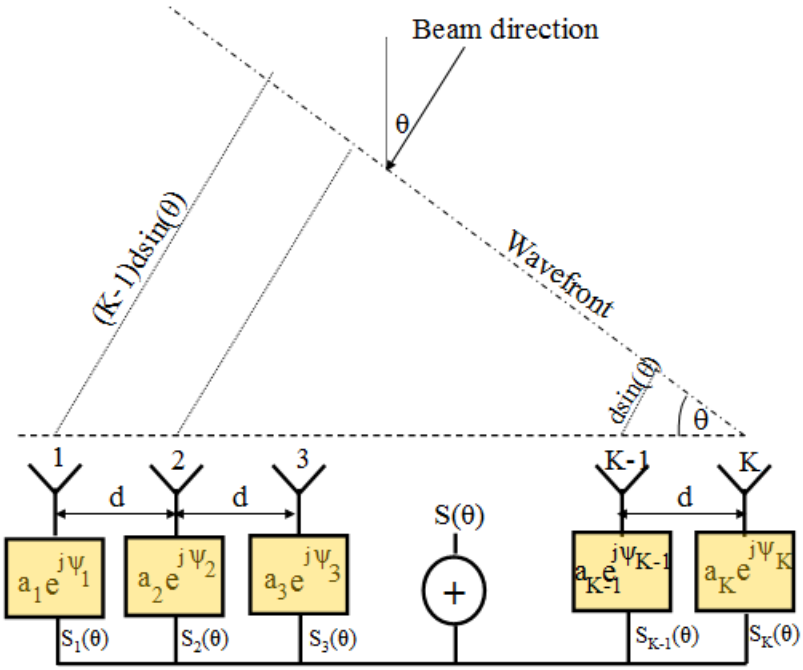

Fig. 1.2, Schematic of a phased array consisting of K elements**.**

In addition to the main radiation lobe peak at θ, grating lobe peaks happen at all θ_g given by

$$\frac{\pi d(\sin\theta_g - \sin\theta)}{\lambda_0} = \pm\pi, \pm 2\pi, \pm 3\pi .... \tag{2}$$

The maximum steering angle is limited to the grating lobe free angular domain around $\theta=0^\circ$. The maximum steering angle dictated by the grating lobes versus the pixel spacing

normalized to the operating wavelength (d/λ_0) is shown in Fig. 1. Chapter 2 is dedicated to a non-uniform array design that can provide large steering angle beyond this uniform array limit.

We also note array elements need to be fed by known phase shifts. This requires an exact knowledge of the phase of each optical waveguide feeding an element prior to the phase shifter module. The most practical way is to use 1×K couplers to equally divide the output power of a coherent light source between the waveguides, whose signal are then phased shifted and then radiated by the array elements. This also requires an exact knowledge of the effect of the 1×K couplers on the phase of each optical channel. The theoretical studies on the output channel phases for multimode interference couplers (MMIs) and the effects of non-idealities on the output phase profile are discussed in Chapter 3.

Another important factor in determining the maximum steering angle is imposed by the ability of phase shifter module of the beam steering system to provide the required phase shift. As can be seen in Fig. 1, some of the preciously presented uniform OPAs did not reach their theoretical steering angle potential, mainly due to the insufficient phase shift provided. The challenges of efficient phase shifters are discussed briefly in Chapter 4. Our final goal is to employ silicon nanomembranes for two dimensional optical beam steering angles over $\pm 60^\circ$ and $\pm 45^\circ$ in the horizontal and vertical directions, respectively.

References

1. P. McManamon, T. Dorschner, D. Corkum, L. Friedman, D. Hobbs, M. Holz, S. Liberman, H. Nguyen, D. Resler, R. Sharp, and E. Watson, “Optical phased array technology,” Proceedings of the IEEE, vol. 84, no. 2, pp. 268–298, 1996.
2. X. Wang, B. Wang, J. Pouch, F. Miranda, J. E. Anderson, and P. J. Bos, “Performance evaluation of a liquid-crystal-on-silicon spatial light modulator”, Opt. Eng., vol. 43, pp. 2769, 2004.
3. M. Jarrahi, R. Fabian W. Pease, D. A. B. Miller, and T. H. Lee, “Optical switching based on high-speed phased array optical beam steering”, Appl. Phys. Lett., vol. 92, pp. 014106, 2008.
4. K. Van Acoleyen, W. Bogaerts, J. Jágerská, N. Le Thomas, R. Houdré, and R. Baets, “Off-chip beam steering with a one-dimensional optical phased array on silicon-on-insulator,” Opt. Lett., vol. 34, pp. 1477-1479, 2009.
5. L. Gu, X. Chen, W. Jiang, B. Howley, and R. T. Chen, “Fringing-field minimization in liquid-crystal-based high-resolution switchable gratings”, Appl. Phys. Lett., vol. 87, pp. 201106, 2005.

Chapter 2: Waveguide Arrays Design for Large Angle Optical Beam Steering

Introduction

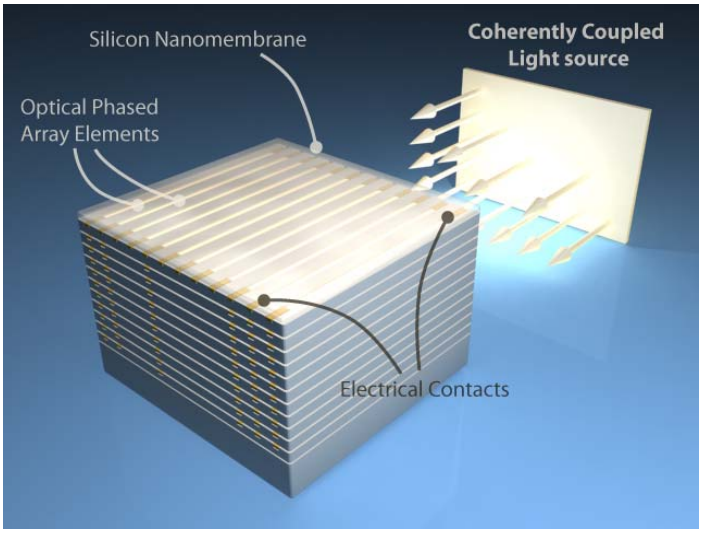

Fig. 2.1, A schematic of silicon nano-membrane-based OPA beam steering.

Optical phased arrays represent an enabling technology that makes possible simple, affordable, and lightweight laser beam steering with precise stabilization, random access pointing and programmable multiple simultaneous beams. Traditionally, optical beam steering has been achieved through mechanically controlled MEMS system [1] and liquid crystal (LC) based optical phased arrays (OPAs) [2]-[4]. Mechanical beam steering provides high steering efficiency and relatively large scanning angle. However, high precision rotating stages are required, which increase the device complexity and are not fast enough for high speed applications. LC OPAs provide rapid random access steering without the expensive and complex mechanical systems [5]. However, LC OPAs suffer

from low steering speed (typically a few milliseconds response time) and limited steering angle (typically not more than 10°) [4]. A GHz optical beam steering system employing phased waveguide array was recently demonstrated with a maximum steering angle of about 6° [6]. The important issue with phased array waveguides is the strong coupling between the adjacent waveguides when the waveguide spacing is reduced to about one-half the operating wavelength, which is necessary for wide angle beam steering. Therefore, the optical coupling jeopardizes the side-lobe level and steering efficiency by imposing a lower limit on the waveguide spacing as will be discussed later in this paper. Other techniques such as beam steering with electro-wetting micro-prisms [7] and polymeric slab waveguide based thermally-induced beam steering [8] have response time in the order of tens of milliseconds.

So far, the large angle beam steering systems have been based on multi-stage systems combining LC OPAs with holographic glass and birefringent prisms [5], for which, alignment and packaging are very challenging.

In order to suppress the side-lobes at large steering angles, different unequally-spaced array structures were proposed [9], [10]. However, an unequally-spaced array realized by random placement of array elements [9] would not result in the optimum OPA performance. An array structure formed by gradually doubling the inter-element spacing along the array can suppress the side-lobes [10], but as we show, it severely reduces the steering efficiency. Additionally, the effects of optical radiator structure, finite fabrication accuracy and the achievable performance have not been investigated.

In this paper, we report a technique to minimize the side-lobe-level (SLL) in unequally-

spaced optical phased waveguide arrays (USOPWAs) while achieving a steering angle of ±45° and avoiding the optical coupling by designing an unequally-spaced array composed of sub-arrays with non-overlapping grating lobes. By optimizing both the array structure and the individual waveguide structure, we present a design methodology for large angle optical beam steering with minimal performance dependence on the steering angle. Finally, we discuss the maximum performance achievable by USOPWAs and compare it with that of the other non-mechanical beam steering technique based on LC OPAs.

Unequally-spaced Array Structure

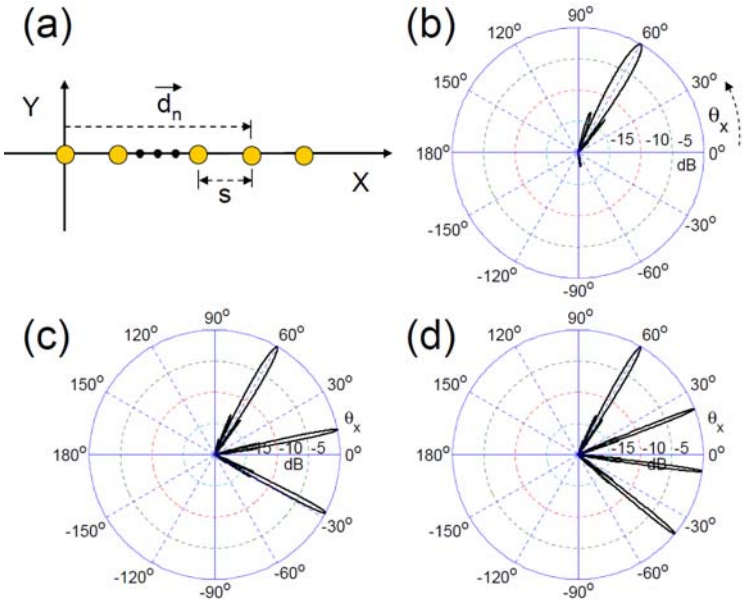

Fig. 2.2, (a) A schematic of a uniform 1D array. Array factor diagrams for 1D uniform arrays, assuming $\beta_n / \left|\vec{d}_n\right| = \frac{156^\circ}{(\lambda/2)}$, (b) N=32 and s=λ/2, (c) N=16 and s=3λ/2, (d) N=16 and s=2λ.

A schematic of a silicon nano-membrane-based OPA system is shown in Fig. 2.1. Similar to their microwave counterparts, linear optical phased arrays consist of 1D or 2D arrays of single-mode waveguides operating at the designated wavelengths. The far field radiation (R) of an optical phased waveguide array (OPWA) is determined by the individual waveguide far field radiation (S), or the "envelope", as well as the array factor (A), $R(\theta x,\theta y)=A(\theta x,\theta y)\cdot S(\theta x,\theta y)$. At a given direction determined by a unit vector $\hat{r}$, the array factor is given as $A=\sum_{n=1}^{N} e^{j(\vec{K}\cdot\vec{d}_n+\beta_n)}$, where, $\vec{K}$ is the wave-vector ($\vec{K}=\frac{2\pi}{\lambda}\hat{r}$), and $\vec{d}_n$ is the translational vector of the nth radiator position, βn is the input optical signal phase of the nth element, and λ is the wavelength. Beam steering can be done by changing the phase shift imposed on each array element. The total number of waveguides is N.

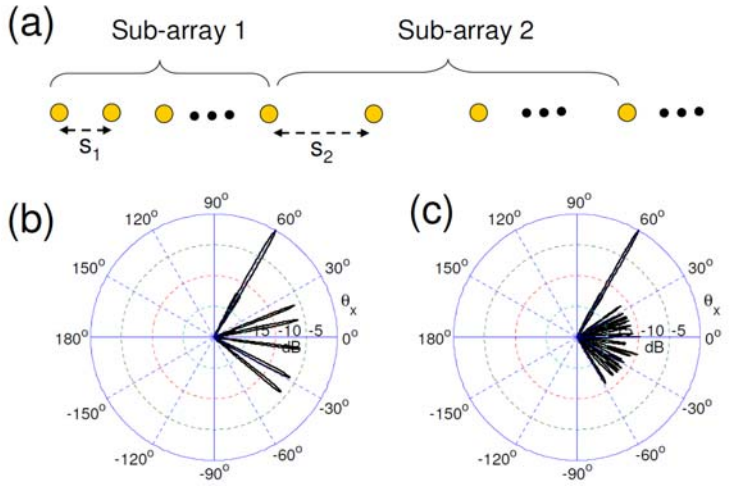

Fig. 2.3, (a) A schematic of the proposed (1D) USOPWA structure. Array factor diagrams for (b) M=2, N=32, q_1=3, q_2=4, s0=λ/2, $(\beta_2-\beta_1)/q_1=156^{\circ}$ and (c) M=4, N=32 q_1=3, q_2=4, q_3=5, q_4=7, s_0=λ/2 and $(\beta_2-\beta_1)/q_1=156^{\circ}$.

Consider a uniform 1D OPWA in the x-direction ($\vec{d}_n = ns\hat{x}$), as shown in Fig. 2.2(a). A criterion for determining the maximum inter-element spacing for the laser beam being steered to a given scan angle θx0 (measured as the angle to the Z axis in the XZ plane), is to set the spacing so that the nearest grating lobe occurs at horizon [11], which leads to

$$\frac{s}{\lambda} \le \frac{1}{1+\sin\theta_{x0}}. \tag{1}$$

This means that the spacing (s) should not be greater than one-half the wavelength for wide scanning angles. Figure 2.2(b) shows the array factor of a uniform 1D OPWA with s= λ/2, and the beam being steered at $\theta_{x0}=60^{\circ}$.

Although this requirement can be easily met in the case of microwave phased arrayed antennas, it imposes a fundamental limit in the case of OPWAs. Since optical waveguides can not support modal sizes smaller than one-half the wavelength, s=λ/2 spacing between adjacent optical waveguide would result in severe waveguide optical mode coupling and therefore, far field pattern (R) distortion.

In case of 1D arrays, $\vec{K}\cdot\vec{d}_n = \frac{2\pi|\vec{d}_n|}{\lambda}\sin\theta_x$. Considering β_n=0, for any s>λ, the grating lobes occur at $\theta_{xp} = \sin^{-1}\frac{P\lambda}{s}$, for P=±1, ±2 …, and s>|Pλ|. In the case of $\frac{\beta_n}{|\vec{d}_n|} = c$ (c is a constant), which is also the case in linear phased arrays, the main lobe occurs at $\theta_{x0} = \sin^{-1}\frac{c\lambda}{2\pi}$, independent of s, and the grating lobe angles are given by

$$\theta_{xp} = \sin^{-1}\left[\frac{P\lambda}{d} - \sin\theta_{x0}\right]. \quad (2)$$

Now consider an unequally-spaced array consisting of M sub-arrays, where the sub-arrays themselves are uniform arrays with spacing $s_1=q_1s_0$, $s_2=q_2s_0$…and $s_M=q_Ms$, and q_i are integer numbers greater than or equal to two [see Fig. 2.3(a)]. If $\frac{\beta_n}{|\vec{d}_n|}=c$ is the same for all sub-arrays, the main lobes associated with all the sub-arrays occur at the same angle. Then if the greatest common divisor (gcd) of every qi and qj (i≠j) is 1, no two sub-arrays will have a common grating lobe angle according to (2). Thus, the main lobes of all the sub-arrays add up constructively, while there is no overlap between the peak grating lobes of each sub-array resulting in one a main lobe and some equi-ripple side-lobes. Although the side-lobe-level (SLL), defined as the ratio of the second largest lobe intensity to the maximum intensity (main lobe) [8], is 0dB for each sub-array, the total array factor can have a much smaller SLL.

To illustrate the idea behind the USOPWAs, consider two uniform 1D arrays with s=3λ/2 and s=2λ, for which the array factors are shown in Figs. 2.2(c) and 2.2(d), respectively. In each case there is at least one grating lobe in the array factor, and thus SLL=0. However, the grating lobes in Figs. 2.2(c) and 2.2(d) do not occur at the same angles and are narrow enough not to overlap. Placing these two uniform arrays along each other to form an unequally-spaced array with $s_0=\lambda/2$, $q_1=3$ and $q_2=4$, reduces SLL to -6dB as shown in Fig. 2.3(b).

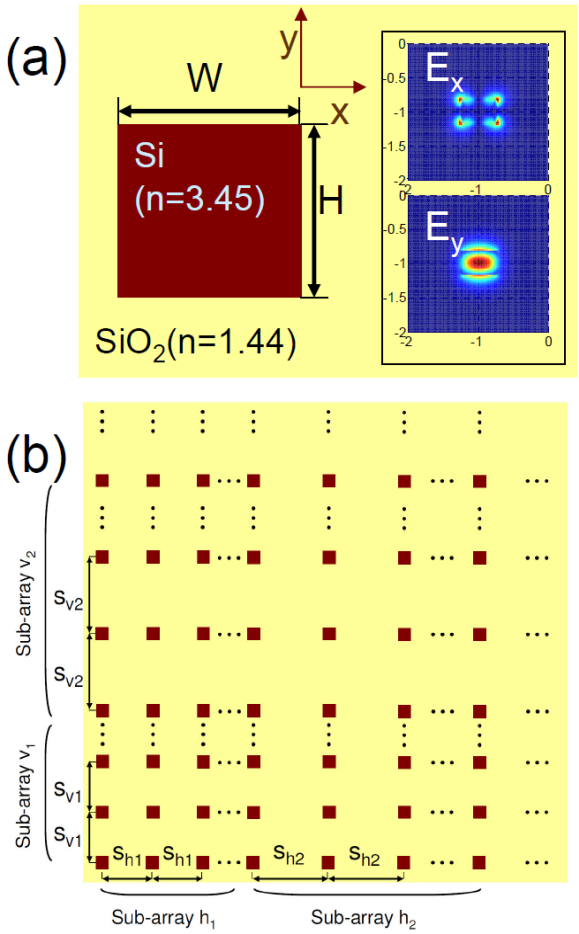

Fig. 2.4, (a) A schematic of a silicon nano-membrane waveguide; the fundamental TM mode field profiles are shown in the inset. (b) A 2D unequally-spaced optical phased waveguide array**.**

In fact, for narrow enough sub-arrays' grating lobes, doubling the number of sub-arrays with non-overlapping grating lobes, can improve the SLL by 6dB. Obviously, the grating lobes corresponding to each sub-array can be arbitrarily narrowed by increasing the number of elements in each sub-array. Figure 2.3(c) shows the array factor of a USOPWA consisting of 4 sub-arrays with non-overlapping grating lobes. As will be

discussed later, the lowest SLL achievable by this technique can not be better than that of a uniform array with $s=s_0$. For the USOPWA shown in Fig. 2.3(c), SLL decreases by increasing M, and finally saturates at the SLL of the far field diagram in Fig. 2(b) (SLL~-14dB).

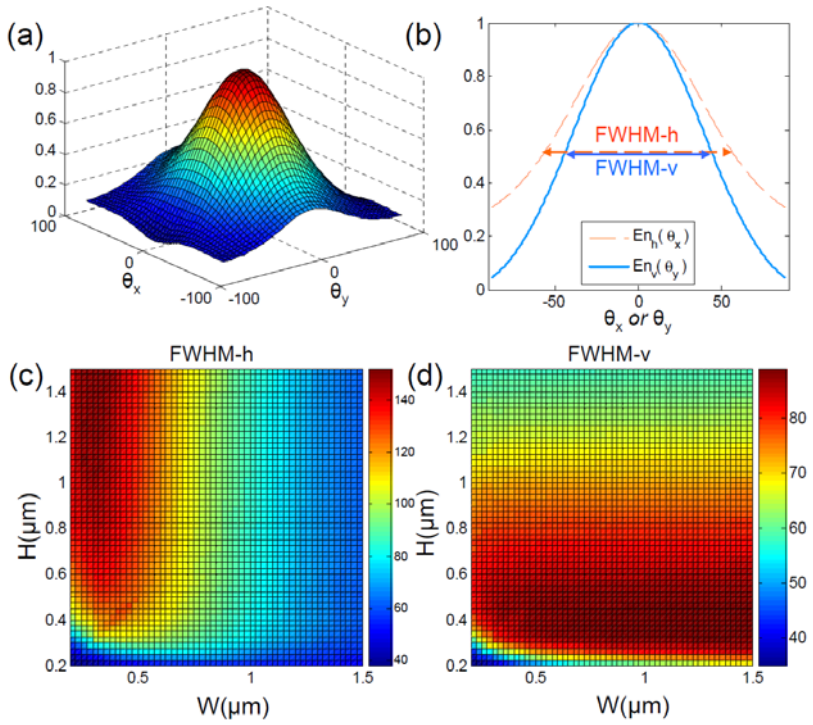

Fig. 2.5, (a) 2D far field radiation of the waveguide shown in Fig. 4(a) assuming W=500nm and H=350nm. (b) Horizontal (En_h) and vertical (En_v) envelopes as functions of θ_x and θ_y, respectively. (c) and (d) variations of FWHM of En_h and En_v [demonstrated in (b)], respectively, versus W and H depicted in Fig. 4(a). All the angles are in degrees and the envelope values in (a) and (b) are normalized.

Here we formulate the non-uniform array design methodology:

- *N*: the total number of radiators
- *M*: number of sub-arrays
- s_i: spacing in sub-array *i,* for *i*=1, 2…

- $s_i = q_i s_0$
  - fabrication resolution$< s_0 < \lambda/2$
  - smallest possible integer numbers q_i such that: $\gcd(q_i, q_j)=1$ ($i \neq j$), and $q_1 < q_2 \ldots < q_M$
- $s_1 >$ modal size.

Note that s_0 must be smaller than $\lambda/2$ in order to avoid overlapping sub-array grating lobes. However, the lowest value of s_0 is determined by the fabrication process, or how precisely the waveguides can be placed in the array. In contrast, s_1 does not depend on the fabrication process, but is constrained by the optical coupling between the waveguides; In other words, s1 must be large enough to avoid waveguide modal field profile overlaps. This condition automatically ensures no optical coupling in all the sub-arrays as well as the first one because $s_1 < s_2 \ldots < s_M$.

For example, in the case of the waveguide shown in Fig. 2.4(a), a center-to-center spacing of 2.4μm~1.5λ (for single mode operating waveguide dimensions W and H < 600nm at λ=1.55μm) diminishes the optical coupling between adjacent waveguides. Assuming, a fabrication resolution of 0.8μm [12], and therefore, s_0=0.8μm, we set s_1 and q_1 to be 2.4μm and 3, respectively. For M=2 [Fig. 2.3(b)], based on the design methodology described above, q_2=4. For M=4 [Fig. 2.3(c)], q_2, q_3 and q_4 are calculated to be 4, 5 and 7. Note, that once q1 is calculated from s0 and s1, qi values (i>1) need to be integer numbers with no common divisor (rather than 1) with each other or q_1 to avoid overlapping grating lobes. In addition, qi values should be the smallest integer numbers possible to avoid unnecessary increasing of the number of side-lobes associated with each

sub-array, which lowers the power efficiency (the ratio of the power radiated in the desired angle to the power radiated in all directions). Throughout the paper s_1=2.4μm and λ=1.55μm are assumed. Note that the presented non-uniform array structure is the first technique to address the optical coupling problem and finite fabrication precision at the same time.

The effect of modal size on the performance of an OPWA is two-fold. A lager modal size means narrower envelope and consequently, smaller allowable steering angles. Also, a larger modal size imposes a lower limit on the inter-element spacing in the array, and thus again, decreases the maximum allowable steering angles. The main importance of the proposed USOPWA design technique is that it allows the inter-element spacing in the array to be large enough to avoid coupling problems between adjacent waveguides, while at the same time still allowing large steering angles. In Section III we optimize the waveguide structure for the widest envelop at λ=1.55μm.

It is worth mentioning that ultra-small modal sizes (modal size<<λ/2) in plasmonic waveguides would allow for large steering angles achievable by conventional uniform waveguide arrays. However, extremely high propagation loss (~0.3dB/μm) in plasmonic waveguides limits their applicability for practical devices [13], [14].

Optimized Waveguide Structure

Silicon-on-insulator (SOI) is an important component of fabricating high performance optical devices due to the high refractive index difference between Si (n=3.45) and SiO_2

(n=1.44). Fabrication of these single-crystal layers of Si on a buried oxide layer is commonly done using the Smart Cut method of hydrogen ion implantation. The ability to stack SOI layers may allow three-dimensional integration of optical devices. This can be accomplished through a number of methods. Alternating depositions of poly-crystalline Si and amorphous SiO_2 can be used, but these growth techniques allow for grain boundaries and surface roughening that contribute to optical degradation [15]. Extension of the Smart Cut method by multiple hydrogen ion implantations has been performed by Malevill et al. [16] but it requires multiple high temperature anneals and can be prohibitively expensive. Nanomembrane transfer is a simpler approach that does not require high temperature anneals, and yet still provides heterostructures with single-crystal Si films that contain high quality interfaces and low surface roughness [15]. In this method, multiple Si-nanomembrane OPAs can be stacked to allow 2D optical beam steering. Since 2D beam steering based on waveguide arrays requires 3D fabrication techniques, including stacking of layers of optical waveguide on top of each other, we assume a standard silicon process to estimate the performance of the USOPWAs (see Fig. 2.4).

A schematic of a silicon waveguide structure assumed here is shown in Fig. 2.4(a). A wider envelope allows for larger scanning angles. In order to calculate the envelope, we use Rsoft FEMSIM to generate the waveguide field profiles, and then we calculate the envelope $R = \left|E^2\right| \propto \left|E_\theta^2\right| + \left|E_\phi^2\right|$ using [17]:

$$
\begin{aligned}
E_\theta &= j\frac{e^{-j\frac{2\pi}{\lambda}r}}{r\lambda}\left[\left(f_x\cos\phi + f_y\sin\phi\right) + \eta\cos\theta\left(g_y\cos\phi - g_x\sin\phi\right)\right] \\
E_\phi &= j\frac{e^{-j\frac{2\pi}{\lambda}r}}{r\lambda}\left[\cos\theta\left(f_y\cos\phi - f_x\sin\phi\right) - \eta\left(g_x\cos\phi + g_y\sin\phi\right)\right] \\
\vec{f}(\theta,\phi) &= \int \vec{E}_t(\vec{r})e^{j\vec{K}\cdot\vec{r}}dr \\
\vec{\mathrm{g}}(\theta,\phi) &= \int \vec{H}_t(\vec{r})e^{j\vec{K}\cdot\vec{r}}dr
\end{aligned}
\tag{3}
$$

where, $\vec{E}_t$ and $\vec{H}_t$ are the tangential electric and magnetic field components, and $\eta=120\pi$ is the intrinsic impedance. The integrals are numerically computed over the waveguide cross-sectional plane. Also, note that $\cos\theta = \cos\theta_x \cos\theta_y$ and $\sin\phi = \sin\theta_x / \sqrt{\sin^2\theta_x + \sin^2\theta_y}$. Without loss of generality, we assume the waveguide is excited by the fundamental transverse magnetic (TM) input fiber mode, for which the main electric component is the y-direction [see Fig. 2.4(a) insets] [18].

A 2D far field radiation pattern (the envelope) is shown in Fig. 2.5(a). We define the horizontal [$En_h(\theta_x)$] and vertical [$En_v(\theta_y)$] envelopes as the variations of the far field radiation pattern at $\theta_y=0^\circ$ and $\theta_x=0^\circ$, respectively [Fig. 2.5(b)]. Figures 2.5(c) and (d) depict the full-width-half-maximum (FWHM) of $Enh(\theta_x)$ and $Env(\theta_y)$, FWHM-h and FWHM-v, respectively, versus the waveguide width (W) and height (H). As the electromagnetic mode extents out of the waveguide area for W and $H \le 300nm$, the envelope becomes narrow (~40° in both directions). In the case of the TM mode, the field profile extent in the vertical direction is more than that in the horizontal direction [see Fig. 2.4(a) insets]. Thus the envelope is wider in the horizontal direction than in the

vertical direction (FWHM-v<FWHM-h) [see Fig. 2.5(b)]. As the narrower envelope determines the worst case SLL and the power efficiency, the optimized waveguide dimensions should maximize FWHM-v, while maintaining single-mode condition, $W,H<\lambda/N_{eff}$, where, N_{eff} is the effective refractive index. From Figs. 2.5(c) and (d), we find that for W=500nm and H=350nm, the FWHM-h and FWHM-v values are 118° and 98°, which allow for about $|\theta_y|\leq 45^\circ$ and $|\theta_x|\leq 60^\circ$ beam steering in the vertical and horizontal directions, respectively, with maximum 3dB envelope variations. Based on the variations of the envelope in Fig. 2.5(a), we expect the worst-case array performance at $\theta_y=\pm 45^\circ$ and $\theta_x=0^\circ$.

If the waveguide is excited by a TE mode, all the above arguments hold true if we replace x by y and horizontal by vertical and vice versa.

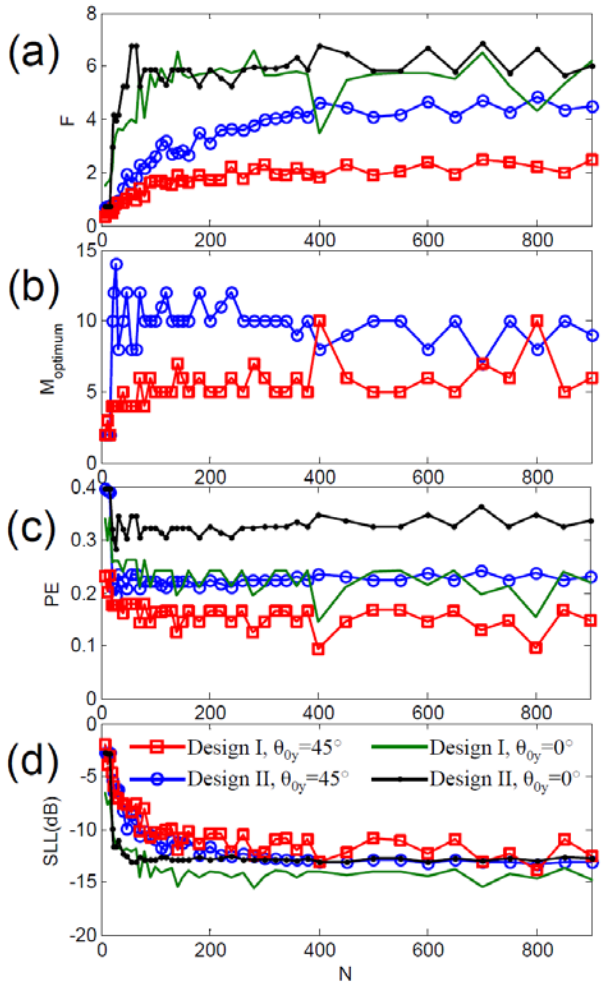

Fig. 2.6, Variations of the maximum figure of merit (*F*), the optimum M, power efficiency (PE), and side-lobe-level (SLL) versus N, in (a)-(d), respectively, for Design I (s0=800nm, q1=$\lceil s_1/s_0 \rceil$=3) and Design II (s0=50nm, q1=$\lceil s_1/s_0 \rceil$=48) for the beam steered at $\theta_{0y}=45^\circ$ and $\theta_{0x}=0^\circ$ and also non-steered beam ($\theta_{0y}=0^\circ$ and $\theta_{0x}=0^\circ$). The optimum M is the same for both steered and non-steered beams in (b).

Optimized Array Design and Performance Analysis

A 2D generalization of the proposed USOPWA is shown in Fig. 2.4(b). For 2D arrays, the array elements are arranged in the XY plane, and similar to 1D cases θ_x (θ_y) is the

angle to the Z axis in the XZ (YZ) plane.

We consider two parameters to evaluate the performance of the USOPWA, SLL and the power efficiency (PE), which is defined as the power in the main peak to the power radiated in all angles. For a fixed total number of radiators (N), as the number of sub-arrays (M) increases, the SLL decreases, however, since the overlap between the grating lobes of the sub-arrays increases, PE reduces. To find the optimum M that minimizes the SLL and maximizes the power efficiency, we define a dimensionless figure of merit (F) as

$$F = \frac{PE}{SLL}. \tag{4}$$

Note that s0 is parameter determined by the fabrication process and therefore, we do not take it into account as an independent variable in the optimization process. PE can be numerically calculated by dividing the summation of the radiation field power within the FWHM of the peak in desired angle by the summation over the radiation field power in all directions.

Now, we consider two designs, Design I: s_0=800nm and Design II: s_0=50nm. In each case, we let N vary, and we find the M value that maximizes F for the worst case scenario (main peak of the steered beam at $\theta_{0y}=45^\circ$ and $\theta_{0x}=0^\circ$). Note that 800nm and 50nm are conservative fabrication resolution assumptions for nano-imprint fabrication techniques and electron beam lithography, respectively [12]. The variations of F, the optimum M value, PE and SLL with N are shown in Fig. 2.6. The performance of Designs I and II for the non-steered beam is also depicted.

In Fig. 2.6(a) the curves corresponding to the steered beam, saturates as N increases, with some relatively small fluctuations. These fluctuations are due to the fact that any M value that is not a divisor of N is not acceptable. Therefore, as M fluctuates [see Fig. 2.6(b)] so does F.

A smaller s_0 allows for higher PE by reducing the number of grating lobes associated with each sub-array. Therefore, the performance of a USOPWA with a smaller s_0 suffers less from the falling envelope at large angles [Fig. 2.6(a)]. Furthermore, the optimum M is higher for a smaller s_0 as shown in Fig 2.6(b). Figure 2.7(a) shows that the degradation of PE from the non-steered beam compared to the worst case is only about 30% for both designs.

As the SLL of the array factor is independent from the steering angle (θ_0), degradation of the SLL with increasing the steering angle is mainly determined by the envelope. At small s_0 values, the side-lobes are more concentrated around the main lobe and therefore, degradation of the SLL as the steering angle changes becomes less significant as shown in Fig. 2.6(d). For the non-uniform array structure presented in [9], our calculations show a PE of 0.016, indicating that SLL was decreased at the expense of severe PE degradation. Based on Fig. 6(a), the F curves of the non-steered beam saturate at around N=128 and N=64 for Design I and II, respectively. Figures 2.7(a) and (b) depict PE and SLL values versus the steering angle ($\theta_{0x}=0^\circ$ and varying θ_{0y}) at these knee N values of the F curves ({s0=800nm, N=128, M=4} and {s0=50nm, N=64, M=8}). Table 2.1 lists the SLL and PE values for these two designs at different steering angles.

Note that the steering efficiency, defined as the main peak intensity of the steered beam

to the main peak intensity of the non-steered beam [4], is more than 65% in both cases at $\theta_{0x}=0^{\circ}$ and $\theta_{0y}=45^{\circ}$. That is because in the case of USOPWAs, the dependence of the steering efficiency on the steering angle is merely due to the envelope.

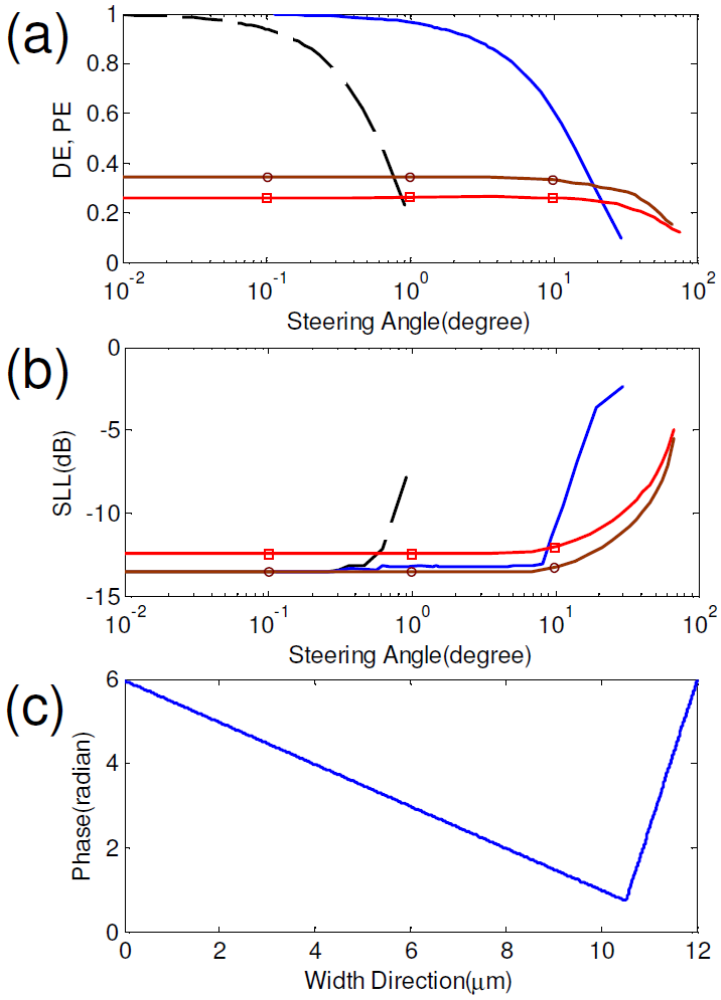

Fig. 2.7, (a) and (b), variations of the diffraction efficiency and SLL versus the steering angle for the liquid crystal (LC) based beam steerer; the black dashed line is for the device (w=20μm, L_f=10μm and maximum angle of 0.23°) from [3]; the blue solid line is the DE curve for the refractive-mode, high-Δn LC with optimized thickness and ideal phase profile (w=1.5μm, L_f=1.5μm, d=2.1μm, Δn=0.35) from [4]. Variations of PE and SLL for Design I (N=128, M=4) and Design II (N=64, M=8) with the steering angle in the vertical direction (θ_{0y}) are depicted by the squared and the circled lines, respectively. (c) Ideal phase profile assumed for the optimized LC OPA [the solid curve in (b) and (c)] with q=8.

Fabrication Issues

Fabricating the basic waveguides is within the state of the art of current technology. That is, we need to pattern 350nm thick silicon single crystal with lines that are 500nm wide. For our application the required tolerance on the waveguide width variation is not yet completely understood but usually a waveguide width tolerance of wavelength (in the Si)/50 should be adequate. This comes to about 10nm so is just within the capabilities of nano-imprint fabrication techniques and present day optical lithography, respectively [12] and well within the capabilities of electron beam lithography (see, for example the current ITRS roadmap www.itrs.net/Links/2008ITRS/Home2008.htm). The spacing requirements depend on the value of so. We assume for now that the tolerance on spacing is about s/10. For design I so has a value of 800nm so the spacing tolerance is easily met. For design II, which is the more desirable when side-lobe suppression is critical, this comes to 5nm so could be challenging. However center lines spacing is usually the easiest dimension to control because it is directly related to the interferometer on the stage of the mask making tool or, when using electron beam direct-write) of the electron beam tool. The required defect densities also should be reachable. The area of the waveguide array is less than that of current IC's requiring more than 20 levels of patterned structure.

Thus patterning a single layer waveguide array to meet the OPA requirements appears within the current state of the art although more analysis on the effects of dimensional imperfections is needed.

Making a multi-level structure such as that shown in fig. 4(b) might well be more challenging. It is similar to the problems presently being faced by those developing 3-D integrated cirtcuitry in that we need multiple levels of features made in device-quality single crystal silicon or germanium and embedded in SiO_2. There are two scenarios. One in which there is active circuitry in the structure and one where there is not. The crucial difference is that in the former we are restricted to temperatures compatible with devices already in the assembly; this is usually about 400C. The ability to employ higher temperatures in the bonding of multiple layers allows greater choice in the materials and processes used. It may be necessary to employ some chemical mechanical polishing to assure sufficiently flat and planar surfaces. The other challenge, common to both scenarios, is the need to overlay accurately the different layers. If we have only a 10nm tolerance then the problem becomes very challenging. Even achieving 100nm tolerance between levels is only just being approached by some of the groups pursuing 3-D integrated circuitry. Thus here again we need more understanding of the required tolerances in layer-to-layer overlay as well as continued effort on achieving nanometer scale overlay precision

Comparison with Liquid Crystal based beam steering systems

Another category of nonmechanical, low power and low size-weight laser beam steering systems is the liquid-crystal optical phased array (LC OPA), with typical ~KHz speed, proposed by McManamon [4]. In terms of speed, OPWA systems (GHz) can outpace LC OPA systems (KHz) by orders of magnitude [6]. However, there are several applications

for which LC OPAs are fast enough, such as laser radar, missile countermeasures, and free space laser communications [4]. Yet as mentioned before, limited steering angle is a remaining challenge for LC OPA laser beam steering. In every non-mechanical beam steering system proposed so far, as the steering angles increases, the appearance of the grating lobes increases the SLL and decreases the power efficiency. Proper voltage profile and electrode structure can increase the maximum steering angle of the LC OPA system. However, to what extent one can improve an LC OPA system performance has not yet been discussed. In this section we compare the theoretical performance of LC OPAs and USOPWAs at large angles. For LC OPAs, we consider the inevitable fly-back region, and assume an ideal linear phase profile and negligible fringing fields. For the USOPWAs, we consider both envelope and array factor effects, and assume an ideal phase distribution for the waveguides in the array.

We can compare the PE defined above with the diffraction efficiency (DE) reported from [3] and [4] for the LC OPAs, since the DE is the ratio of the power in the desired diffraction order to the total diffracted power. Figure 2.7(a) shows the variations of DE for a device from [3] and a reported optimized design from [4]. For the optimized reflective mode LC OPA structure (LC layer thickness d=2.1μm), high birefringence (Δn=0.35), both pixel size (w) and fly-back region size (Lf) of 1.5μm, and an ideal phase profile out of the fly-back region [Fig. 7(c)] are assumed. The DE curves in Fig. 2.7(a) were calculated from the analytical expression in [3]:

$$DE = \left(\frac{\sin \pi / q}{\pi / q} \right)^2 \left(1 - \frac{L_f}{qw} \right)^2 \tag{3}$$

Where, q is the number of pixels between two resets. When the beam is steered to 30°, DE is degraded more than 90% compared to the non-steered beam (steering efficiency less than 10%). Note that here, we have neglected the fringing field effects that distort the phase profile, specially, in the case of 2D beam steering, where the distorted phase profile in one direction can affect the phase profile in the other direction. Moreover, we assume that the fly-back region is limited to one pixel, and does not affect the phase profile of the period after the reset. Rather than the DE degradation problem, the SLL is also severely degraded at large steering angles in LC OPA. Fig. 2.7(b) depicts SLL as a function of the steering angle for the two abovementioned LC OPAs.

Table 2.1, Unequally-spaced array based beam steering performance.

Design	*F*-curve knee N value	M	Array size (μm)	$\theta_{0x}=0^\circ$ $\theta_{0y}=0^\circ$		$\theta_{0x}=0^\circ$ $\theta_{0y}=45^\circ$		$\theta_{0x}=60^\circ$ $\theta_{0y}=0^\circ$	
				SLL(dB)	PE(%)	SLL(dB)	PE(%)	SLL(dB)	PE(%)
I	128	4	114	-12.1	26.3	-8.5	18.0	-9.0	21.0
II	64	8	300	-13.4	34.6	-9.4	23.4	-10.1	25.7

In order to estimate the theoretical limits of the LC OPA performance, we assume, a reflective LC with Δn=0.5, w/d=0.5 and L_f=w (a valid assumption for small pixel sizes), with the ideal phase profile. The steering angle is given as

$$\theta_0 = \sin^{-1}\left(\frac{2d\Delta n}{qw}\right) = \sin^{-1} 2/q, \tag{4}$$

Assuming q=4 and θ=30°, DE becomes 45%. Given that not more than ¾ of the power is radiated to the desired angle, the SLL will be no better an -6dB. Note that for w/d<1, the

phase profile strongly deviates from the ideal ramp and that reduces the DE. In addition, 4 pixels are not enough to produce a desired phase profile. Therefore, the physical limits of the LC OPAs do not allow for an efficient beam steering at scanning angles larger than 30°. Also, $\Delta\theta_0 / \Delta q \approx -2/\sqrt{q^2-1}$ becomes larger as q decreases (at large angles), and fundamentally, beam steering with a resolution better than about 5° is not possible at θ_0 more than 25° using single stage LC OPAs. Figures 2.7(a) and (b) show that the performance (DE, SLL and resolution) of the LC OPA strongly depends on the steering angle.

Summary

we presented an unequally-spaced OPA design for high-efficient large optical beam steering at 1.55μm, with minimal performance dependence on the steering angle. Assuming fabrication precision of 800nm and 128 array elements, we demonstrated a beam steering with a worst-case power efficiency and side-lobe-level of about 18.0% and -8.5dB during $\pm 60^{\circ}$ and $\pm 45^{\circ}$ 2D optical beam steering, which correspond to degradation of about 32% and -3.6dB, respectively, with respect to those of the non-steered beam. Increasing the number of array elements and smaller fabrication resolution can improve the performance. The OPA performance dependence on the steering angle is only due to the far-field pattern of single elements, which can be further improved using waveguide structures that support smaller modal sizes.

References

1. Y. Petremand, P.-A. Clerc, M. Epitaux, R. Hauffe, W. Noell, and N. F. de Rooij, “Optical beam steering using a 2D MEMS scanner”, Proc. SPIE, vol. 6715, pp. 671502, Oct. 2007.
2. P. F. McManamon, T. A. Dorschner, D. L. Corkum, L. J. Friedman, D. S. Hobbs, M. Holz, S. Liberman, H. Q. Nguyen, D. P. Resler, R. C. Sharp and E. A.Watson, “Optical phased array technology,” Proc. IEEE, vol. 84, no. 2, pp. 268–298, Feb. 1996.
3. X. Wang, B. Wang, J. Pouch, F. Miranda, J. Anderson, and P. Bos, “Performance evaluation of a liquid-crystal-on-silicon spatial light modulator,” Opt. Eng., vol. 43, pp. 2769-2774, Nov. 2004.
4. X. Wang, B. Wang, P. Bos, P. F. McManamon, J. J. Pouch, F. A. Miranda, and J. E. Anderson, “Modeling and design of an optimized liquid-crystal optical phased array”, J. Appl. Phys., vol. 98, pp. 073101, Oct. 2005.
5. P. F. McManamon, “Agile Nonmechanical Beam Steering,” Optics & hotonics News, vol.17, pp. 24-29, Mar. 2006.
6. M. Jarrahi, R. Fabian, W. Pease, D. A. B. Miller, and T. H. Lee, “High-speed optical beam-steering based on phase-arrayed waveguides”, J. Vac. Sci. Technol. B, vol. 26, pp. 2124-2126, Dec. 2008.
7. N. R. Smith, D. C. Abeysinghe, J. W. Haus, and J. Heikenfeld, “Agile wide-angle beam steering with electrowetting microprisms," Opt. Exp., vol. 14, pp. 6557-6563, 2006.
8. G. Cocorullo, M. Iodice, “Thermally induced optical beam steering in polymeric slab waveguide”. Fibres and Optical Passive Components, Proc. of IEEE/LEOS, 2005.
9. F. Xiao, W Hu, and A. S. Xu, “Optical phased-array beam steering controlled by wavelength,” App. Opt., vol. 44, no. 26, pp. 5429–543, Sept. 2005.
10. J. H. Abeles and R. J. Deri, “Suppression of sidelobes in the far feld radiation patterns of optical waveguide arrays,” App. Phys. Lett., vol. 53, no. 15, pp. 1375-1377, Oct. 1988.
11. R. J. Mailloux, Phased Array Antenna Handbook, 1993.
12. H. Schift, “Nanoimprint lithography: An old story in modern times? A review”, J. Vac. Sci. Technol. B, vol. 26, pp. 458-480, Mar. 2008.
13. J. A. Dionne, L. A. Sweatlock, H. A. Atwater, and A. Polman, “Plasmon slot waveguides: Towards chip-scale propagation with subwavelength-scale localization”, Phys. Rev. B, vol. 73, 035407, Jan. 2006.
14. Hosseini, A. Nieuwoudt, Y. Massoud, “Optimizing Dielectric Strips Over a Metallic Substrate for Subwavelength Light Confinement”, IEEE photonic Tehnol. Lett, vol. 19, no. 7, pp. 522 – 524, Apr 2007.
15. W. Peng, M. M. Roberts, E. P. Nordberg, F. S. Flack, P. E. Colavita, R. J. Hamers, D. E. Savage, M. G. Lagally, and M. A. Eriksson, "Single-crystal silicon/silicon dioxide multilayer heterostructures based on nanomembrane transfer," Appl. Phys. Lett., vol. 90, 183107, May 2007.

16. C. Maleville, T. Barge, B. Ghyselen, A. J. Auberton, H. Moriceau, and A. M. Cartier, “Multiple SOI layers by multiple Smart-Cut (R) transfers,” Proc. of IEEE International SOI Conference, Wakefield, p. 134, 2000.
17. S. J. Orfanidis, Electromagnetic Waves and Antennas, 2004.
18. Y. Vlasov and S. McNab, “Losses in single-mode silicon-on-insulator strip waveguides and bends,” Opt. Exp. ,vol. 12, pp. 1622-1631, 2004.

Chapter 3: Output Formulation for Symmetric Multimode Interference Coupler

Introduction

Multimode interference (MMI) based devices have been widely used in photonic integrated circuits (PICs) as compact size passive components power splitters [1], [2], 90° hybrid couplers [3] and mode-matching stages [4]. MMI-based active devices such as optical switches [5], [6] and phased array multiplexers [7] have been theoretically studied and experimentally demonstrated. The interest in MMI based devices stems from properties such as compact size, low power imbalance, stable power splitting ratio, low cross talk, large optical bandwidth, and high tolerance to fabrication process [2], [8], which render such devices suitable for integration in PICs with complex passive networks including power splitters and signal routing. Compared to Y-branches, MMI splitters are smaller and benefit from scalability as the number of the output ports grows.

Several studies investigated the quality of the output signals in MMI couplers based on power uniformity [3], [9] and image resolution [10]. Also, several techniques have been proposed to improve the signal quality, such as tapered multimode waveguide [11], graded-index waveguide [12] and deeply etched air trenches at the boundary of the multimode section [2]. In addition to power splitter, MMI coupler can be used in more complex photonic components where the phase of the output signal is also important, such as 90° hybrid couplers [3].

In addition to power splitter, MMI coupler can be used in more complex photonic components where the phase of the output signal is also important, such as 90° hybrid couplers [3]and in high-speed phased array optical beam steering [13]. Despite the effort in investigating the power profile at the MMI output ports, there have been no studies on the output phase profile. In many applications, the knowledge of the phase pro file is important. The phase differences of MMI output ports can severely distort the performance of compact optoelectronic devices that employ a multimode waveguide region to generate several channels with linear phase profiles such as optical spatial quantized analog-to-digital converters [14] and GHz Optical beam steerers [15]. The knowledge of the MMI output phase profile will provide a means to apply appropriate phase shifts in order to attain the desired phase profile.

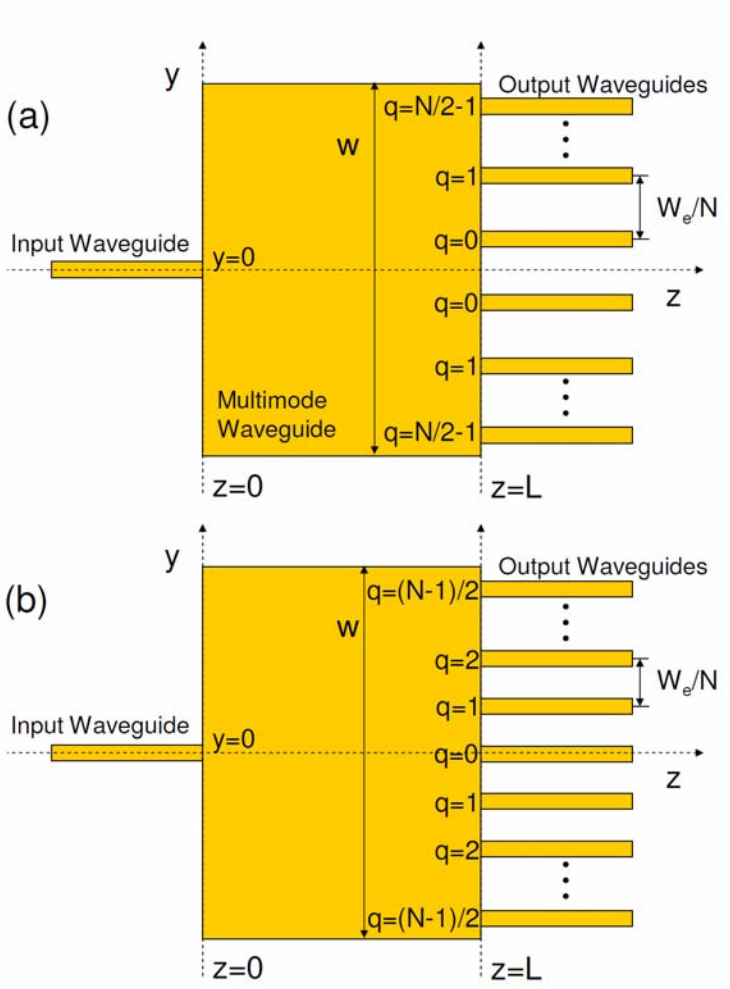

Fig. 3.1, Schematics of 1 × N symmetric MMI coupler, (a) even N, (b) odd N.

Symmetrically excited one-to-N MMI couplers are the most common power splitters in photonic circuitries, where the number of output ports has been reported from 2 to as large as 64 [16]. In this paper, we derive an analytical formula for the symmetrically excited MMI output phase profile, and compare the results with beam propagation simulations. Additionally, we report a complete description of the output field profile at the symmetric N-fold imaging length in ideal MMI couplers. Our analysis is most

accurate for high index contrast waveguides. However, image enhancing techniques, such as etched air trenches introduced to define the edges of the MMI coupler [2], make the presented analysis applicable to low index contrast waveguides, such as polymer based structures. Such etched air trenches reduce the lateral penetration depth into the cladding so that the effective width of all the guided modes is approximately the same as the actual width of the MMI coupler, and therefore improve the output power uniformity. Finally, we discuss the effect of this technique on the output phase profile, which determine the controllability of the output phased array.

Multimode Interference Couplers

Self-imaging is a phenomenon in multimode waveguides by which an input field profile is reproduced in single or multiple images at periodic intervals along the propagation direction of the guide [3]. This effect has been exploited in different MMI based structures. Several MMI coupler structures have been theoretically studied and experimentally fabricated [1]–[3], [9], [10], [16]. In Fig. 3.1 the multimode waveguide section consists of a W -wide core of refractive index nc, embedded in between cladding layers of n_0. In the case of 3D waveguides, an equivalent 2D representation can be made by techniques such as the effective index method or the spectral index method [3]. The multimode section can support maximum M + 1 number of modes. For each mode p, the dispersion relation is given as

$$\beta_p^2 + \kappa_{yp}^2 = \left(\frac{2\pi n_c}{\lambda_0} \right)^2, \tag{11}$$

where, β_p is the propagation constant of the the pth mode, λ_0 is a free-space wavelength. κ_{yp} is the lateral wavenumber of the pth mode, given as $\kappa_{yp} = (p+1)\pi/W_e$, where W_e is the effective width for mode m including the penetration depth due to the Goose-Hahnchen shift [2]. The propagation constant β_p can be approximated as

$$\beta_p \approx \beta_0 - \frac{p(p-2)}{3L_\pi}, \tag{12}$$

where, $L_\pi=\pi/(\beta_0-\beta_1)\approx 4n_c W_e^2/3\lambda_0$. Given the orthogonality of the propagating modes, any input field profile at z = 0, can be written as a linear combination of the propagating modes,

$$\Phi(y, z=0) = \sum_{p=0}^{M} c_p \phi_p(y), \tag{13}$$

where cp is the excitation coefficient of the pth mode by the given input field profile, calculated as the overlap integrals of the pth mode and the input field profile [3]. Each excited mode accumulates phase shift according to its propagation constants and therefore, the field profile at any z = L can be represented by

$$\begin{aligned} &\exp(-j\beta_0 L)\sum_{p=0}^{M} c_p \phi_p(y) \exp\left(-j(\beta_p - \beta_0)L\right) \approx \\ &\exp(-j\beta_0 L)\sum_{p=0}^{M} c_p \phi_p(y) \exp\left(j\frac{p(p+2)\pi}{3L_\pi}L\right). \end{aligned} \tag{14}$$

At $L = 3rL_\pi$ with r =1, 2, ..., all the exponential terms in (4) becomes in-phase with one another and a single image of the input field profile is formed. Generally, an N-fold image of the input field profile is formed At $L = 3L_\pi/N$. In the case of symmetric

excitation, $\Phi(y,Z=0) = \Phi(y,Z=0)$, only the even modes p =2m, for integer m, are excited. This type of excitation can be realized by a symmetric input filed profile fed to the center of the multimode waveguide Fig. 3.1. This has been known to result in short 1xN couplers, where N is the number of output ports [3]. The required length for such a coupler is given as which is four times shorter than the general case. $L = 3rL_\pi/4N$, r integer.

In the case of 1xN couplers, the output power is ideally designed to be equally divided among the output ports and therefore, the field amplitude at the output ports is $1/\sqrt{N}$. In reality, however, the approximation in (2) becomes inaccurate especially for the higher order modes in low refractive index contrast waveguides. In these cases, the Goose-Hahnchen effect becomes mode dependent and the accumulated phase shift of each mode is different from the ideal case by an error of

$$\Delta\varphi_p \approx \frac{\lambda_0^2 (p+1)^4 \pi}{2Nn_c^2 W_{eff}^2}\left[1/8 - \frac{\lambda_0 n_c^2}{6\pi W_w (n_c^2 - n_0^2)^{1.5}}\right] \tag{15}$$

for the N-fold imaging length $L = 3rL_\pi/N$ [9]. The existence of these modal phase errors is inherent in the dispersion law of the dielectric slab waveguides. Additional phase errors happen when the observation plane is shifted away from the paraxial plane [10]. In the case of the symmetric excitation, the accumulated phase error at the N-fold imaging length is $\Delta\psi_p/4$. This error would result in non-uniformity in the output power distribution. The phase profile of the output ports and the effect of non-ideal effects on the output phase profile have not been investigated. In the next section we derive a closed form formula for the output field profile.

Symmetric MMI Coupler Phase Profile

Consider the 1xN MMI coupler shown in Fig. 3.1. In order to analyze the output properties, such as image resolution, contrast, etc, Ulrich and Kamiya approximated the multimode waveguide propagating modes field profiles with cosine functions,

$$\phi_p(y) = \cos(\kappa_{yp} y), \tag{16}$$

which allowed them to apply the Fourier transform properties to the field presentation in [10]. In this paper we adopt the same technique to take the position (in the y-direction) of the images formed into account.

Consider one of the N images of the input field at an N-fold imaging length and shifted in the y-direction to y = yq. Based on (3), this image can be presented as $B\Phi(y-y_q, z=0)$

$B\Phi(y-y_p, z=0) = B\sum_{p=0}^{M} c_p \varphi_p(y-y_q)$, where $B = \frac{\exp(j\theta_q)}{\sqrt{N}}$, assuming uniform power distribution. As shown in Figs. 1(a) and (b) for the N images formed at the output ports the lateral shifts of the position with respect to the input image are yq =±We/2N, ±3We/2N..., ± (N-1)We/2N for even N, and yq =0, ±We/N, ±2We/N, ±(N-1)We/2N for odd N. Therefore, at an N-fold imaging length (L_0) the field profile $\Phi(y,L_0)$ is

$$\frac{1}{\sqrt{N}} \sum_{q=0}^{N/2-1} \exp(j\theta_q) \sum_{p=0}^{M} c_p \left(\cos\left[\kappa_{yp} (y - \frac{(2q+1)W_e}{2N}) \right] + \cos\left[\kappa_{yp} (y + \frac{(2q+1)W_e}{2N}) \right] \right), \tag{17}$$

for even N, and

$$\frac{1}{\sqrt{N}}\exp(j\theta_0)+\frac{1}{\sqrt{N}}\sum_{q=1}^{(N-1)/2}\exp(j\theta_q)\times \sum_{p=0}^{M}c_p\left(\cos\left[\kappa_{yp}(y-\frac{qW_e}{N})\right]+\cos\left[\kappa_{yp}(y+\frac{qW_e}{N})\right]\right), \tag{18}$$

for odd N. In (7) and (8), the symmetry of the structure have been taken into account by letting $\theta_{-q} = \theta_q$. We can simplify (7) and (8) using the trigonometric identity cos(a+b)= cos(a)cos(b)-sin(a)sin(b). We also note that when the multimode waveguide is symmetrically excited, only the even modes of the multimode region are excited, and therefore $c_p = 0$ for odd p values. We can rewrite (7) and (8) with $c_p = c_{2m}$

$$\frac{2}{\sqrt{N}}\sum_{q=0}^{N/2-1}\exp(j\theta_q)\times \sum_{=0}^{M}c_{2m}\cos(\kappa_{yp}y)\cos\left[\frac{(2m+1)(2q+1)}{2N}\pi\right], \tag{19}$$

for even N, and

$$\frac{1}{\sqrt{N}}\exp(j\theta_0)+\frac{2}{\sqrt{N}}\sum_{q=1}^{(N-1)/2}\exp(j\theta_q)\times \sum_{m=0}^{M/2}c_{2m}\cos(\kappa_{yp}y)\cos\left[\frac{(2m+1)q}{N}\pi\right], \tag{20}$$

for odd N. We can also rewrite the field profile from (4) at a symmetric N-fold imaging length, $L_0 = 3L_\pi/4N$, considering p =2m

$$\Phi(y,L_0)=\sum_{m=0}^{M/2}c_{2m}\phi_{2m}(y)\exp(j\frac{m(m+1)}{N}\pi). \tag{21}$$

Note that we have dropped the common factor $\exp(-j\beta_0 L_0)$, for simplicity, but we will add it back later. Using the reciprocity law for quadratic Gauss sums we can show that in the case of even N

$$\sum_{m=0}^{M/2} C_{2m}\phi_{2m}(y)\exp\left[j\frac{m(m+1)}{N}\pi\right] =$$
$$\frac{2\exp(j\frac{N-2}{4N}\pi)}{\sqrt{N}}\sum_{m=0}^{M/2} C_{2m}\phi_{2m}(y)\times \tag{22}$$
$$\sum_{q=0}^{N/2-1}\exp\left(-j\frac{q(q+1)}{N}\pi\right)\cos\left(\frac{(2m+1)(2q+1)\pi}{2N}\right).$$

Comparing (12) and (9), one can conclude that

$$\exp(j\theta_q) = \exp(j\frac{N-2}{4N}\pi)\times\exp(-j\frac{q(q+1)}{N}\pi). \tag{23}$$

Taking in the common factor, $\exp(-j\beta_0 L_0)$, into account,

$$\theta_q = -\beta_0 L_0 + \frac{N-2-4q(q+1)}{4N}\pi, \tag{24}$$

for q = 0, 1..., N/2-1, where q is assigned to the output ports as shown in Fig. 3.1(a). Note that the phase profile is symmetric with respect to the line y = 0.We can identify that the phase profile has a propagation accumulated phase term, a constant term depending on the number of output channels, which is the same for all the channels, and a term that quadratically depends on the channel number (starting from the middle of the waveguide). In the case of odd N, one can show

$$\sum_{m=0}^{M/2} C_{2m}\phi_{2m}(y)\exp\left[j\frac{m(m+1)}{N}\pi\right] =$$
$$\frac{\exp(j\frac{N-1}{4N}\pi)}{\sqrt{N}}\sum_{m=0}^{M/2} C_{2m}\phi_{2m}(y)\times \tag{25}$$
$$\left(1+2\sum_{q=1}^{(N-1)/2}\exp\left(-j\frac{q^2}{N}\pi\right)\cos\left(\frac{(2m+1)q\pi}{N}\right)\right).$$

Similarly, in the case of odd N, comparing (15) and (10) one can conclude that

$$\theta_q = -\beta_0 L_0 + \frac{N-1-4q^2}{4N}\pi, \tag{26}$$

for q = 0, 1, ...(N - 1)/2, where the q values are assigned to the output ports as shown in Fig. 1(b). Again, the phase profile is symmetric with respect to the line y = 0. Although the discussion in this paper is based on dielectric waveguides, similar results are expected in the case of self-imaging in other waveguiding structures, such as multimode photonic crystal waveguides, which can be realized by removing several periods in the transverse direction [17].

Simulation Results and Discussion

In order to investigate the MMI structure output phase we performed 3D semi vectorial beam propagation method (SVBPM) simulations using the BeamPROP module in RSoft CAD. Figure 3.2(a) shows the field propagation profile of a 1-to-6, S_i/S_iO_2 MMI coupler. The refractive indices of the core and cladding layers are $n_c = n_{Si} = 3.47$ and $n_0 = n_{SiO2} = 1.45$, respectively. A cross-section diagram of the multimode waveguide is shown in the inset of Fig. 2.2(c). The input and output ports consist of waveguides with 2.5μmxh cross-sections, where h =0.25μm is the thickness of the multimode waveguide [Fig. 3.2(c) inset]. In order to compare the BPM simulation results with the analytical formula derived in the Section III, we take one of the middle output ports (for even N) [port number 3 in Fig. 3.2(a)].

to be phase reference, for which the phase is set to 0. Figure 3.2(c) compares the output phase profile from the BPM simulations with that calculated using (14).

Note that the high core/cladding layers refractive index contrast in the S_i/S_iO_2 MMI coupler results in well-defined edge along the length of the multimode waveguide. In order to investigate the phase profile in case of low refractive index contrast, we simulated a polymer waveguide structure composed of ZPU12-RI series polymer materials from ChemOptics [2], where the core and the cladding layers are ZPU12-460 (n_c =1.46) and (ZPU12-450) (n_0 =1.45), respectively. For this MMI structure, with input and output waveguides of 5μm×h cross-section and h =5μm. This MMI structure is adopted from [2] with no air trench along the multimode waveguide. Figure 3.2(b) shows the field propagation profile of the ZPU12-RI MMI coupler and Fig. 3.2(c) compares the simulated output phase profile with the analytical calculations derived in Section III.

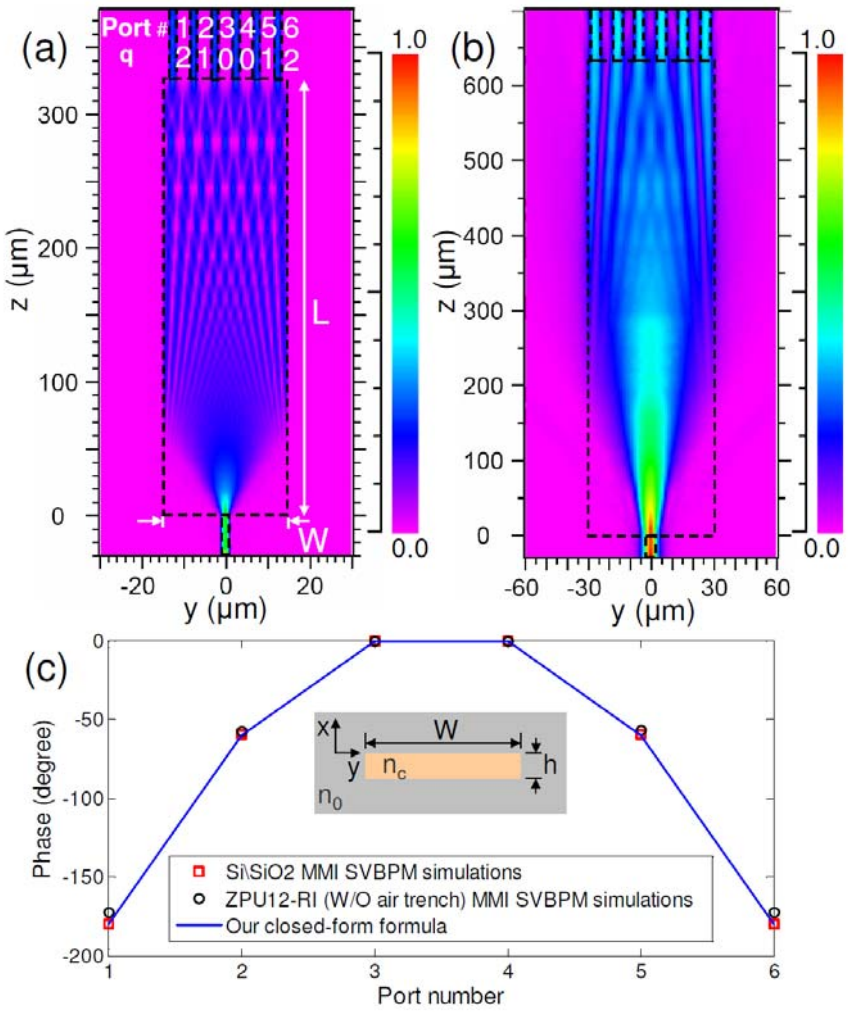

Fig. 3.2, Beam propagation simulation results , (a) field propagation profile at x =0for the Si/SiO2 MMI with N =6, W =30μm L =325μm and h =0.25μm, (b) field propagation profile at x =0for the ZPU12-RI MMI with N =6, W =60μm L =625μm and h =5μm. (c) Phase profile from Beam Propagation Method simulation of the MMI structures in (a) and(b) and the ideal phase profile form the analytical model with q values shown in (a). A cross-section diagram of the multimode waveguide is shown in the inset of (c).

Table I compares the BPM simulation results with the analytical calculations for several Si/SiO2 and ZPU12-RI MMIs with output number varying from N =3 to N =12. In the

case of Si/SiO2 MMIs, the MMI width W = Nx5μm and the MMI height h =0.25μm. In the case of the ZPU12-RI MMIs, W=Nx10μm and h =5μm. In all cases the MMI length is $L = 3L_{\pi}/4N$, and the input waveguide is excited by a TE-polarized mode. λ_0 =1600nm and $\Delta x = \Delta y = \Delta z = \lambda_0 / (20 n_{core})$ .The output ports that correspond to q =0 are taken as the reference, for which the phase is zero. According to Fig. 1, for the middle output port in the case of odd N values and for the two equivalent output ports in the middle in the case of even N values q is 0.

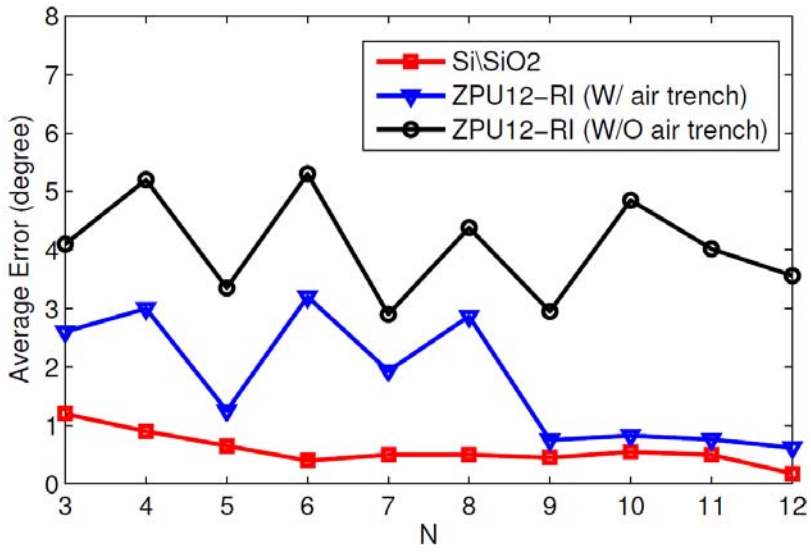

Fig. 3.3, The average output phase profile error of the Si/SiO2 MMIs, ZPU12RI MMIs without air trenches and ZPU12-RI MMIs with air trenches with respect to the analytical model.

In the case of the Si/SiO2 MMIs, the output phase values are within about 1○ of the calculated values from the analytical models in (14) and (16). In the case of the ZPU12-RI MMIs, the average phase profile error with respect to the analytical models is about 5◦. This error can be attributed to modal phase errors expressed in (5), and also the deviation of the modal field profiles [$\varphi_p(y)$] from the cosine-shape functions as the

penetration of the evanescent field into the cladding layers is more in lower refractive index contrast waveguides. The modal phase errors are the main cause of non-uniformity in the output amplitudes [9], [10]. Table I indicates that the output phase deviates more from the ideal self-imaging guide analytical model as the output port is shifted away from the paraxial plane (y =0). Therefore, the main source of errors in the phase profile is the deviation of the modal field profiles from the cosine-shape functions. In fact, for large N, the output phase values for the ports in the middle of the MMI structure are almost the same as those in the Si/SiO2 MMIs and ZPU12RI MMIs.

Wang and Chen showed that etching deep air trenches along the multimode waveguide to define the edges of the MMI coupler substantially reduced the lateral penetration depth into the cladding in the case of low contrast refractive index structures [2]. Therefore, the effective width of all the guided modes is approximately the same as the actual width of the MMI coupler. Hence, the presence of air trenches improves image quality. In order to investigate the effect of such air trenches on the output phase profile, we simulated the same ZPU12-RI MMI structures but with air trenches along the multimode waveguide sides using the 3D SVBPM simulator. The resulted output phase values are presented in Table I. Introducing the air trenches specially improves the modal field profiles away from the paraxial plane and therefore, correction in the output phase values is more significant in the outer ports (large q) compared to that of the ports in the middle (small q) of the MMI structure.

Figure 3 illustrates the average output phase error of the Si/SiO2 MMIs, ZPU12-RI MMIs without air trenches and ZPU12-RI MMIs with air trenches with respect to the

analytical model as the number of outputs changes from N =3 to N =12. In the case of the PU12-RI MMIs with air trenches the output phase of the middle ports are close to the ideal values at large N values, similar to the PU12-RI MMIs withair trenches. Therefore, the correction of the output phase of the outer ports by introducing the air trench, results in a smaller average output phase profile error as the N increases.

Summary

We derived analytical formulations for the output phase profile of symmetrically excited one-to-N multimode interference couplers. We showed that the output phase increases quadratically from the middle of the MMI waveguide, which needs to be taken into account for phase-dependent applications such as optical phased arrays. We compared the analytical calculations with the results of beam propagation simulations for different MMI structures and found that the effect of the penetration of the field into the cladding layers at the side walls was more than the modal phase errors on the output phase profile. However, even in the case of low refractive index contrast of $\Delta n = 0.01$, the output phase was within the 10° intervals from the predicted values.

Table 3.1, closed-form analytical formulation results vs. BPM simulations. All the numbers are in degrees.

		Analytical Model									
Analytical Model	θ_j	N=3	N=4	N=5	N=6	N=7	N=8	N=9	N=10	N=11	N=12
	θ_0	0	0	0	0	0	0	0	0	0	0
	θ_1	-60	-90	-36	-60	-25.7	-45	-20	-36	-16.4	-30
	θ_2	x	x	-144	-180	-102.9	-135	-80	-108	-65.5	-90
	θ_3	x	x	x	x	-231.4	-270	-180	-216	-147.3	-180
	θ_4	x	x	x	x	x	x	-320	-360	-261.8	-300
	θ_5	x	x	x	x	x	x	x	x	-409.1	-450
		BPM Simulation									
Si/SiO_2	θ_j	N=3	N=4	N=5	N=6	N=7	N=8	N=9	N=10	N=11	N=12
	θ_0	0	0	0	0	0	0	0	0	0	0
	θ_1	-58.8	-89.1	-36.6	-59.5	-25.5	-44.4	-19.8	-35.4	-16.4	-30.0
	θ_2	x	x	-144.7	-179.7	-102.3	-134.1	-79.7	-107.7	-64.5	-90.1
	θ_3	x	x	x	x	-230.7	-270.0	-179.6	-215.5	-146.9	-180.3
	θ_4	x	x	x	x	x	x	-319.1	-359.2	-261.3	-299.9
	θ_5	x	x	x	x	x	x	x	x	-408.5	-449.6
		BPM Simulation									
ZPU12-RI (W/O Air Trench)	θ_j	N=3	N=4	N=5	N=6	N=7	N=8	N=9	N=10	N=11	N=12
	θ_0	0	0	0	0	0	0	0	0	0	0
	θ_1	-55.9	-84.8	-34.7	-57.1	-25.3	-44.1	-19.7	-35.8	-16.1	-29.6
	θ_2	x	x	-138.6	-172.3	-100.7	-131.3	-79.6	-105.6	-64.6	-89.5
	θ_3	x	x	x	x	-225.3	-261.4	-176.1	-209.8	-144.6	-177.3
	θ_4	x	x	x	x	x	x	-312.8	-349.4	-254.8	-293.5
	θ_5	x	x	x	x	x	x	x	x	-399.9	-442.3
		BPM Simulation									
ZPU12-RI (W/ Air Trench)	θ_j	N=3	N=4	N=5	N=6	N=7	N=8	N=9	N=10	N=11	N=12
	θ_0	0	0	0	0	0	0	0	0	0	0
	θ_1	-57.4	-87.0	-35.3	-57.1	-25.4	-43.1	-19.7	-35.7	-16.5	-29.9
	θ_2	x	x	-142.2	-176.5	-101.0	-132.2	-79.8	-108.5	-65.9	-89.8
	θ_3	x	x	x	x	-227.8	-266.2	-179.7	-215.1	-148.0	-179.5
	θ_4	x	x	x	x	x	x	-317.8	-359.0	-262.3	-299.1
	θ_5	x	x	x	x	x	x	x	x	-407.0	-448.6

Proof I: Proof for even N

In the case of $N = 2K$ and $K \in Z$, we need to show

$$\sum_{m=0}^{M/2} C_{2m}\phi_{2m}(y)\exp\left[j\frac{m(m+1)}{N}\pi \right] = \frac{2\exp(j\frac{N-2}{4N}\pi)}{\sqrt{N}} \sum_{m=0}^{M/2} C_{2m}\phi_{2m}(y) \times \sum_{q=0}^{N/2-1} \exp\left(-j\frac{q(q+1)}{N}\pi \right)\cos\left(\frac{(2m+1)(2q+1)\pi}{2N} \right). \quad (17)$$

Note that y in (17) is an independent variable. Therefore, in order to prove (17), we need to show that for every m, the coefficients of $C_{2m}\varphi_m(y)$ on the left and right sides of (17) are equal. Thus, we need to prove

$$\exp\left[j\frac{m(m+1)}{N}\pi \right] = \frac{2\exp(j\frac{N-2}{4N}\pi)}{\sqrt{N}} \times \sum_{q=0}^{N/2-1} \exp\left(-j\frac{q(q+1)}{N}\pi \right) \cos\left(\frac{(2m+1)(2q+1)\pi}{2N} \right), \tag{18}$$

which simplifies to

$$\frac{2\exp(j\frac{N-2}{4N}\pi)}{\sqrt{2K}} \sum_{q=0}^{K-1} \exp\left(-j\frac{q(q+1)+m(m+1)}{2K}\pi \right) \cos\left(\frac{(2m+1)(2q+1)\pi}{4K} \right) = 1 \tag{19}$$

Let us simplify the left hand side of (19):

$$\frac{2\exp(j\frac{K-1}{4K}\pi)}{\sqrt{2K}} \times \{ \sum_{q=0}^{K-1} \exp\left(-j\frac{2q(q+1)+2m(m+1)-(2m+1)(2q+1)}{4K}\pi \right) \exp\left(-j\frac{2q(q+1)+2m(m+1)+(2m+1)(2q+1)}{4K}\pi \right) \} = 1 \tag{20}$$

which further simplifies to

$$\frac{2\exp(j\frac{1}{4}\pi)}{\sqrt{2K}} \sum_{q=0}^{K-1} \{ \exp\left(-j\frac{(m-q)^2}{2K}\pi \right) + \exp\left(-j\frac{(m+q+1)^2}{2K}\pi \right) \}. \tag{21}$$

Now note that

$$\sum_{q=0}^{K-1} \{ \exp\left(-j\frac{(m-q)^2}{2K}\pi \right) + \exp\left(-j\frac{(m+q+1)^2}{2K}\pi \right) \} = \sum_{q=m+1-K}^{m+K} \exp\left(-j\frac{q^2}{2K}\pi \right). \tag{22}$$

Consider a set of integer numbers {m-K+1, m-K+2…,m+K}. Regardless of m, this set imodules 2K is exactly the same as {0, 1…,2K-1}mod(2K). it can be easily shown that if $a \equiv b \bmod(2K)$, then

$a^2 \equiv b^2 \bmod(4K)$, hence $\exp(-j2\pi a^2/4K) = \exp(-j2\pi b^2/4K)$ or $\exp(-j2\pi a^2/4K) = \exp(-j2\pi b^2/K)$. Therefore, the expression in (22) is independent of m as follows,

$$\sum_{q=m+1-K}^{m+K} \exp\left(-j\frac{q^2}{2K}\pi\right) = \sum_{q=0}^{2K-1} \exp\left(-j\frac{q^2}{2K}\pi\right). \tag{23}$$

From the abovementioned statements we can also conclude

$$\sum_{q=0}^{2K-1} \exp\left(-j\frac{q^2}{2K}\pi\right) = \sum_{q=1}^{2K} \exp\left(-j\frac{q^2}{2K}\pi\right) = \sum_{q=2K+1}^{4K} \exp\left(-j\frac{q^2}{2K}\pi\right), \tag{24}$$

which leads to

$$\sum_{q=m+1-K}^{m+K} \exp\left(-j\frac{q^2}{2K}\pi\right) = \frac{1}{2}\sum_{q=1}^{4K} \exp\left(-j\frac{q^2}{2K}\pi\right). \tag{25}$$

Using the reciprocity law for quadratic Gauss sums defined as

$$G(N;M) = \sum_{q=1}^{M} \exp(j2\pi Nq^2/M), \tag{26}$$

we can write the results as follows

$$G(N=1;M) = \sum_{q=1}^{M} \exp(j2\pi q^2/M) = \frac{1}{2}\sqrt{M}(1+j)[1+\exp(-j\pi M/2)], \tag{27}$$

which is equal to $(1+j)\sqrt{M}$ if $M \equiv 0 \bmod(4)$. Comparing (25) and (27) we can conclude that

$$\begin{aligned} &\sum_{q=m+1-K}^{m+K} \exp\left(-j\frac{q^2}{2K}\pi\right) = \frac{1}{2}G^*(1,4K) = \\ &\frac{1}{2}(1-j)\sqrt{4K} = (1-j)\sqrt{K} = \exp(-j\frac{\pi}{4})\sqrt{2K}, \end{aligned} \tag{28}$$

where, G* is the complex conjugate of G. Consider (19), (22), (23) and (28), we can write

$$\frac{2\exp(j\frac{N-2}{4N}\pi)}{\sqrt{2K}}\sum_{q=0}^{K-1}\exp\left(-j\frac{q(q+1)+m(m+1)}{2K}\pi\right)\cos\left(\frac{(2m+1)(2q+1)\pi}{4K}\right)=$$
$$\frac{e^{j\pi/4}}{\sqrt{2K}}\sum_{q=0}^{2K-1}\exp(-j\frac{q^2}{2K}\pi)=\frac{e^{j\pi/4}}{\sqrt{2K}}\times\exp(-j\frac{\pi}{4})\sqrt{2K}=1.$$

Therefore, we have proved (18) and consequently (17).

Proof II: Proof for odd N

In the case of $N=2K+1$ and $K\in Z$, we need to show

$$\sum_{m=0}^{M/2}C_{2m}\phi_{2m}(y)\exp\left[j\frac{m(m+1)}{N}\pi\right]=$$
$$\frac{\exp(j\frac{N-1}{4N}\pi)}{\sqrt{N}}\sum_{m=0}^{M/2}C_{2m}\phi_{2m}(y)\times\left(1+2\sum_{q=1}^{(N-1)/2}\exp\left(-j\frac{q^2}{N}\pi\right)\cos\left(\frac{(2m+1)q\pi}{N}\right)\right). \quad (29)$$

Similar to the case of even N, since y in (17) is an independent variable, in order to prove (29), we need to show that for every m, the coefficients of $C_{2m}\varphi_m(y)$ on the left and right sides of (29) are equal. Thus, we need to prove

$$\exp\left[j\frac{m(m+1)}{N}\pi\right]=$$
$$\frac{\exp(j\frac{N-1}{4N}\pi)}{\sqrt{N}}\left(1+2\sum_{q=1}^{(N-1)/2}\exp\left(-j\frac{q^2}{N}\pi\right)\cos\left(\frac{(2m+1)q\pi}{N}\right)\right), \quad (30)$$

or equivalently,

$$\frac{\exp(j\frac{2K}{4(2K+1)}\pi)}{\sqrt{2K+1}}\{\exp\left[-j\frac{m(m+1)}{2K+1}\pi\right]+ \\ 2\sum_{q=1}^{K}\exp\left(-j\frac{q^2+m(m+1)}{2K+1}\pi\right)\cos\left(\frac{(2m+1)q\pi}{2K+1}\right)\}=1, \tag{31}$$

Consider the left-side of (31)

$$\frac{\exp(j\frac{2K}{4(2K+1)}\pi)}{\sqrt{2K+1}}\{\exp\left[-j\frac{m(m+1)}{2K+1}\pi\right]+ \\ \sum_{q=1}^{K}\exp\left(-j\frac{q^2+m(m+1)-(2m+1)q}{2K+1}\pi\right)+\exp\left(-j\frac{q^2+m(m+1)+(2m+1)q}{2K+1}\pi\right)\}, \tag{32}$$

which simplifies to

$$\frac{\exp(j\frac{2K}{4(2K+1)}\pi)}{\sqrt{2K+1}}\{\exp\left[-j\frac{m(m+1)}{2K+1}\pi\right]+ \\ \sum_{q=1}^{K}\exp\left(-j\frac{(q-m-1/2)^2-1/4}{2K+1}\pi\right)+\exp\left(-j\frac{(q+m+1/2)^2-1/4}{2K+1}\pi\right)\}, \tag{33}$$

and further simplies to

$$\frac{\exp(j\frac{1}{4}\pi)}{\sqrt{2K+1}}\{\exp\left[-j\frac{(m+1/2)^2}{2K+1}\pi\right]+ \\ \sum_{q=1}^{K}\exp\left(-j\frac{(q-m-1/2)^2}{2K+1}\pi\right)+\exp\left(-j\frac{(q+m+1/2)^2}{2K+1}\pi\right)\}. \tag{34}$$

Note that

$$\exp\left[-j\frac{(m+1/2)^2}{2K+1}\pi\right]+\sum_{q=1}^{K}\{\exp\left(-j\frac{(q-m-1/2)^2}{2K+1}\pi\right)+ \\ \exp\left(-j\frac{(q+m+1/2)^2}{2K+1}\pi\right)\}=\sum_{q=-K}^{K}\exp\left(-j\frac{(2q+2m+1)^2}{4(2K+1)}\pi\right). \tag{35}$$

Consier $q = n(2K+1) + r$, $-K \le q \le K$ and $0 \le r \le 2K$. Then, $\{q+m\} \bmod(2K+1) \equiv \{q\} \bmod(2K+1)$ with the same set of residuals {r}, for every integer m. In addition, $\{2q+2m+1\} \bmod(2K+1)$ is the set of {2r+1}. Therefore, $\forall m \in Z$ and $\forall q \in \{q\}$, $\exists r \in \{q\}$ so that 2m+2q+1=2p(2K+1)+(2r+1) for some integer p. Thus, we can write

$$(2m+2q+1)^2 = 4p(2K+1)[p(2K+1)+(2r+1)] + (2r+1)^2 \tag{36}$$

Also not that p[p(2K+1)+(2r+1)] is always ever. Thus, $(2m+2q+1)^2 = 8s(2K+1)+(2r+1)^2$ for some interger s. and

$$\sum_{q=-K}^{K} \exp\left(-j\frac{(2q+2m+1)^2}{4(2K+1)}\pi\right) = \sum_{r=0}^{2K} \exp\left(-j\frac{(2r+1)^2}{4(2K+1)}\pi\right) = \exp\frac{-j\pi}{2(2K+1)} \sum_{r=0}^{2K} \exp\frac{r^2+r}{2K+1}\pi. \tag{37}$$

Now consider the Gauss Quadratic Reciprocity law $\forall a,b,c,z \in Z$, $ac \neq 0$ and even $ac+b$

$$\sum_{z=0}^{|c|-1} \exp\left(j\pi\frac{az^2+bz}{c}\right) = \sqrt{|c/a|}\exp\left(j\pi\frac{|ac|-b^2}{4ac}\right) \sum_{z=0}^{|a|-1} \exp\left(j\pi\frac{cz^2+bz}{a}\right). \tag{38}$$

Let $a,b=1, z=r$ and $c=2K+1$, we can say $ac+b=2K+2$ is always even, therefore, we can use the Gauss Quadratic Reciprocity law as follows

$$\exp\frac{-j\pi}{2(2K+1)} \sum_{r=0}^{2K} \exp\frac{r^2+r}{2K+1}\pi. = \exp\frac{-j\pi}{2(2K+1)} \times \sqrt{2K+1}\exp\left(-j\pi\frac{2K}{4(2K+1)}\right) = \sqrt{2K+1}\exp(-\frac{\pi}{4}). \tag{39}$$

From (34) and (39) we conclude

$$\frac{\exp(j\frac{1}{4}\pi)}{\sqrt{2K+1}}\{\exp\left[-j\frac{(m+1/2)^2}{2K+1}\pi\right]+$$
$$\sum_{q=1}^{K}\exp\left(-j\frac{(q-m-1/2)^2}{2K+1}\pi\right)+\exp\left(-j\frac{(q+m+1/2)^2}{2K+1}\pi\right)\}= \quad (40)$$
$$\frac{\exp(j\frac{1}{4}\pi)}{\sqrt{2K+1}}\times\sqrt{2K+1}\exp(-j\frac{1}{4}\pi)=1$$

Therefore, we have proved (30) and consequently (29).

References

1. J. S. Yu, J. Y. Moon, S. M. Choi, and Y. T. Lee, "Fabrication of 1x8multimode-interference optical power splitter based on inp using ch4/h2 reactive ion etching," Japanese Journal of Applied Physics, vol. 40, no. Part 1, No. 2A, pp. 634–639, 2001.
2. X. Wang and R. T. Chen, "Image enhanced polymer-based multimode interference coupler covering c and l bands using deeply etched air trenches," Applied Physics Letters, vol. 90, no. 11, p. 111106, 2007.
3. L. Soldano and E. Pennings, "Optical multi-mode interference devices based on self-imaging: principles and applications," Lightwave Technology, Journal of, vol. 13, no. 4, pp. 615–627, Apr 1995.
4. X. Chen, W. Jiang, J. Chen, L. Gu, and R. T. Chen, "20 db-enhanced coupling to slot photonic crystal waveguide using multimode interference coupler," Applied Physics Letters, vol. 91, no. 9, p. 091111, 2007.
5. Y.-J. Chang, T. K. Gaylord, and G.-K. Chang, "Pulse response of multimode interference devices," J. Lightwave Technol., vol. 24, no. 3, p. 1462, 2006.
6. J. Xia, J. Yu, Z. Wang, Z. Fan, and S. Chen, "Low power 22 thermooptic soi waveguide switch fabricated by anisotropy chemical etching," Optics Communications, vol. 232, no. 1-6, pp. 223 – 228, 2004.
7. M. Paiam and R. MacDonald, "A 12-channel phased-array wavelength multiplexer with multimode interference couplers," Photonics Technology Letters, IEEE, vol. 10, no. 2, pp. 241–243, Feb 1998.
8. M. Rajarajan, B.Rahman, T. Wongcharoen, and K. Grattan, "Accurate analysis of MMI devices with two-dimensional confinement," Lightwave Technology, Journl of, vol. 14, no. 9, pp. 2078–2084, Sep 1996.

9. J. Huang, R. Scarmozzino, and J. Osgood, R.M., “A new design approach to large input/output number multimode interference couple rsand its application to low-crosstalk WMD routers,” Photonics Technology Letters, IEEE, vol. 10, no. 9, pp. 1292–1294, Sep 1998.
10. R. Ulrich and T. Kamiya, “Resolution of self-images in planar optical waveguides,” J. Opt. Soc. Am., vol. 68, no. 5, pp. 583–592, 1978.
11. R.M.Lorenzo, C. Llorente, and E. J. A. M. Lopez, “Improved self-imaging characteristics in i x n multimode couplers,” IEE Proc.-Oproelectron, vol. 145, no. 1, pp. 65–69, 1998.
12. R. Yin, X. Jiang, J. Yang, and M. Wang, “Structure with improved self imaging in its graded-index multimode interference region,” J. Opt. Soc. Am. B, vol. 19, no. 6, pp. 1301–1303, 2002.
13. M. Jarrahi, R. F. W. Pease, D. A. B. Miller, and T. H. Lee, “Optical switching based on high-speed phased array optical beam steering,” Applied Physics Letters, vol. 92, no. 1, p. 014106, 2008.
14. M. Jarrahi, R. F. W. Pease, and T. H. Lee, “Spatial quantized analog-to-digital conversion based on optical beam-steering,” J. Lightwave Technol., vol. 26, no. 14, pp. 2219–2226, 2008.
15. R. F. P. M. Jarrahi, D. A. Miller, and T. H. Lee, “An overview of optical phased array technology and status,” Applied Physics Letters, vol. 92, no. 014106, 2008.
16. T. Rasmussen, J. Rasmussen, and J. Povlsen, “Design and performance evaluation of 1-by-64 multimode interference power splitter for optical communications,” Lightwave Technology, Journal of, vol. 13, no. 10, pp. 2069–2074, Oct 1995.
17. Z. Li, Y. Zhang, and B. Li, “Terahertz photonic crystal switch in silicon based on self-imaging principle,” Opt. Express, vol. 14, no. 9, pp. 3887– 3892, 2006.

Chapter 4: 1xN Multimode Interference Beam Splitter Design Techniques for On-Chip Optical Interconnections

Introduction

On-chip optical interconnections are being considered as a solution for the looming interconnection bottlenecks of limited bandwidth and large latencies. A network of on-chip optical interconnects in integrated photonic circuits (PICs) needs efficient optical beam splitting and beam shaping components as building blocks.

The self-imaging properties of multimode optical waveguides have been utilized in NxM multimode interference (MMIs) couplers. The theory of self-imaging in multimode optical waveguides has been the subject of several studies [1-6]. The resolution and contrast of the images formed in the multimode waveguide determine the uniformity and insertion loss (or equivalently the total transmitted power) of MMI splitter devices [1]. It has been shown that 1xN MMI couplers with large number of outputs (N) normally result in poor output uniformity and high insertion loss [2]. It has been shown that optimizing the core/cladding index contrast [2, 3] can improve the MMI performance.

A design methodology is required for on-chip high performance MMIs for which the choice of tuning index contrast is not an option. Additionally, despite the advances in computer aided design (CAD) tools for integrated electronic components, there has been little work on design tools for on-chip optical components. We aim to find design rules

that can be reliably used for on-chip efficient beam splitters without the need for time-consuming and computationally expensive simulations for each individual component. By analyzing the phase errors in symmetrically excited 1xN MMIs due to deviations in the high order mode dispersion relations from those required for ideal self- imaging, we derive a relation for the maximum number of output channels for a given MMI width that can still result in an acceptable MMI performance.

Silicon nanomembrane based optical devices in silicon-on-insulator (SOI) substrates can be integrated with silicon electronics using techniques such as localized substrate removal [7]. Localized Oxidized Silicon-On-Insulator from bulk silicon has been also used as potential platform to integrate silicon photonics and electronics [8]. We designed and fabricated several MMIs based on silicon nanomembrane rib waveguides. Experimental results show that the analytical formulas derived in this paper can be used as guidelines for on-chip MMI designs. Therefore, the presented design methodology can be easily implemented in computer aided design (CAD) tools.

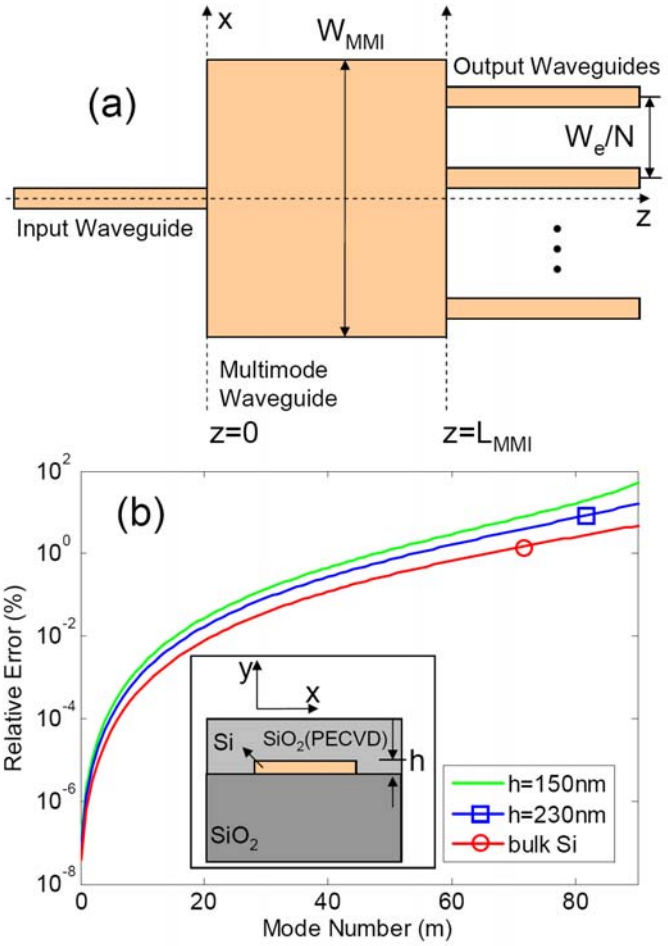

Fig. 4.1, (a) A schematic of a 1xN MMI beam splitter. Inset is a cross sectional schematic of the SOI waveguiding structure. n_{Si}=3.47, n_{SiO2}=1.45, $n_{SiO2(PECVD)}$=1.46. (b) Relative modal propagation constant (β_m) when evaluated using Equation (2) for W_{MMI}=30μm and λ_0=1.55μm for different silicon nanomembrane thicknesses (h) and bulk silicon (infinite h). A schematic of the waveguide structure cross-section is shown in the inset.

Maximum Number of Output Channels

Figure 4.1 shows a schematic of a 1xN MMI splitter. The multimode waveguide section consists of a W_{MMI} wide and L_{MMI} long core with refractive index n_c. In the case of

channel waveguides, an equivalent 2D representation can be made by techniques such as the effective index method or the spectral index method [7]. Assume that n_{eff} is the effective index of the fundamental mode of an infinite slab waveguide with same thickness and claddings. For each mode p ($0 \le p \le M$) of a MMI, that can support (M+1) modes, the dispersion relation is given as [1]

$$\beta_m^2 + \kappa_{xp}^2 = \left(\frac{2\pi n_{\text{neff,1D}}}{\lambda_0} \right)^2, \tag{1}$$

where, β_m is the propagation constant of the m^{th} mode, λ_0 is the free-space wavelength. K_{xm} is the lateral wavenumber of the m^{th} mode given as $\kappa_{xm} = \pi(m+1)/W_e$, where W_e is the effective width including the penetration depth due to the Goose-Hahnchen shift [4]. We use the effective width for generality, however, due to the high index contrast, $W_e = W_{MMI}$ is a good approximation in silicon photonics. $n_{eff,1D}$ is the effective index of the fundamental mode of an infinite slab waveguide with same thickness and claddings from the effective index method. In the theory of self imaging, β_m is approximated from Equation (1) as [1]

$$\beta_m \approx \beta_0 - \frac{m(m-2)}{3L_\pi}, \tag{2}$$

where, $L_\pi = \pi/(\beta_0 - \beta_1) \approx 4 n_{eff,1D} W_e^2 / 3\lambda_0$. In the case of symmetric excitation, such as a 1xN coupler excited by the fundamental mode of the input waveguide, using the approximation in Equation (2), one can show that the required length for such a coupler is $L_{M\text{MI}} = 3iL_\pi/4N$, where i is an integer.

This approximation results in errors as shown in Fig. 4.1(b). Interestingly, as the thickness of the silicon nanomembranes is reduced, the error approximation becomes less accurate. Therefore, addressing the induced phase errors is more critical in rib silicon waveguides than in the case of ridge waveguides, such as the ones investigated in [9].

When using Equation (2), the error in the calculated propagation constant can be estimated by the third term in the Taylor Expansion of β_m, given by Equation (1) as $\Delta\beta_m \approx 2(\kappa_{xm}\lambda_0/4\pi n_{eff,1D})^4$. After propagating along the MMI, the resulting modal phase errors at the output are given as

$$\Delta\varphi_m = \Delta\beta_m L_{MMI} = \frac{\pi\lambda_0^{\,2}(m+1)^4}{64 N n_{\mathrm{neff,1D}}^{\,2} W_e^{\,2}}. \tag{3}$$

For a high quality image, we restrict the maximum $\Delta\varphi_m$ to $\pi/2$, which gives q, which is the maximum allowed mode number (p). In this way, we eliminate the modal phase errors that result in modal field signs. We choose W_w so that the highest order mode excited in the multimode region can satisfy this restriction. To do so, we pick W_w to be equal to the lateral wavelength ($2\pi/\kappa_{xq}$) of the highest allowed mode given by $\Delta\varphi_m < \pi/2$. This also guarantees negligible excitation of all higher order modes since several periods of these modes fall within the input excitation field and the resulting overlap integrals are thus small. By equating $W_{w,min} = 2\pi/\kappa_{xq}$ we get

$$W_{w,\min} = \frac{1}{\sqrt[4]{2N}} \sqrt{\frac{\lambda_0 W_e}{n_{\mathrm{neff,1D}}}}. \tag{4}$$

The $W_{w,min}$ decreases as N increases. This is due to the fact that MMI's length decreases linearly with increasing N. Therefore, the accumulated phase errors $\Delta\varphi_m = L_{MMI}\Delta\beta_m$ are

also reduced with increasing N. Increasing access waveguide width for improving MMI performance was proposed in [9] without any notes on how wide the access waveguides should be. Equation (4) gives the minimum W_w for an acceptable MMI performance in terms of the insertion loss and output uniformity.

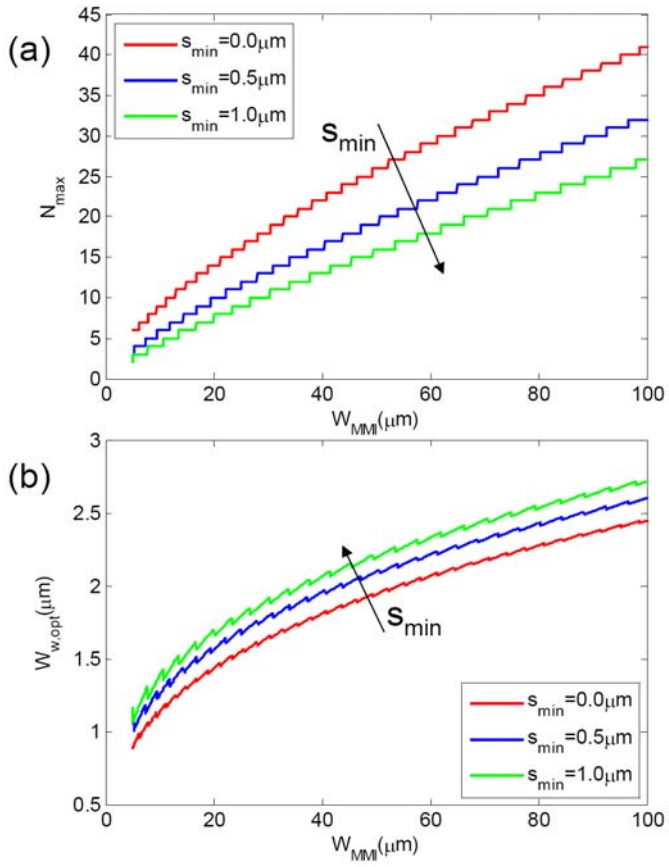

Fig. 4.2, (a) Variation of the maximum number of the output channels versus MMI width. (b) Variations of the optimum channel width for 1xN_{max} MMIs versus MMI width.

We note that that the output channel-to-channel spacing is W_e/N. Therefore, we can derive an upper bound on the maximum number of channels for which the image quality is still acceptable by $W_{w,min} < W_e/N$ given as

$$N_{\max} \le \left\lfloor \sqrt[3]{\frac{2n_{\text{neff,1D}}{}^{2} W_e{}^{2}}{\lambda_0{}^{2}}} \right\rfloor. \tag{5}$$

The result is quite general (optimistic) and gives an upper bound for N_{max} for any waveguiding structure. For more realistic N_{max} , one needs to consider

$$N_{\max} \le \left\lfloor \frac{W_e}{W_{w,\min} + s_{\min}} \right\rfloor, \tag{6}$$

where s_{min} depends on the waveguiding structure and is the minimum required side-to-side spacing between the output waveguides to avoid channel-to-channel coupling and/or required by the geometrical restrictions of the devices connected to the MMI's output channels, as well as the limitations of the fabrication technique.

Figure 4.2(a) shows N_{max} as a function of W_{MMI} for s_{min}=0 [Equation (5)], s_{min}=0.5μm and s_{min}=1.0μm. $n_{eff,1D}$=2.85, which corresponds to h=230nm at λ_0=1.55μm in Fig. 4.1(b) inset. The s_{min}=1.0μm is chosen to avoid optical coupling in thin silicon rib waveguides of the MMIs' outputs and also to minimize the effects of the proximity effect during the e-beam writing as presented. Fig. 4.2(b) demonstrates variations of $W_{w,min}$ versus W_{MMI} for an MMI with N_{max} output channels.

From Equation (5), N_{max} is a sub-linear function of the W_{MMI} even in the most optimistic case, where s_{min}=0. This is also evident from Fig. 4.2. In other words, if an MMI design with W_{MMI} and N results in a good MMI performance, in general, an MMI design with RW_{MMI} and RN does not necessary exhibit a good performance, where R is an integer number equal or greater than 2. This is an important consideration for scalability of MMI based devices.

Equations (4) and (5) guarantee good MMI performance without a need to apply the other performance enhancing techniques such as index contrast tuning [2, 10], multimode section input taper [3], or L_{MMI} and output access waveguide position optimization [11]. We will investigate this claim using eigenmode decomposition based simulations in Section III and rib waveguide MMIs' in Section IV.

Table 4.1, 1xN MMI based optical beam splitters' length and channel width dimensions for h=230nm at λ_0=1.55μm. L_{MMI} values are calculated using $L_{MMI} = 3rL_\pi/4N$.

N	**W_{MMI}** (μm)	**L_{MMI}** (μm)	**$W_{w,min}$** (μm)	**W_w** (μm)
6	30	276	2.16	2.16
8	30	207	2.02	2.02
10	30	166	1.91	1.91
12	30	138	1.83	1.50
14	30	118	1.76	1.14
16	30	104	1.70	0.88

Simulations and Discussions

In order to investigate the effect of W_w on the quality of the N-fold self-imaging we used the eigenmode expansion (EME) simulator in the FIMMPROP™ module from Photon Design. The EME method is based on a rigorous solution of Maxwell's Equations, and therefore the results approach the exact solution for a large number of modes in the expansion. The algorithm is inherently bi-directional and fully vectorial [13]. We assumed SOI substrate as shown in Fig. 4.1 inset, where the thickness of the silicon slab

is h=230nm n_{Si}=3.47, n_{SiO2}=1.45, $n_{SiO2(PECVD)}$=1.46, and $n_{eff,1D}$=2.85. Throughout this paper λ_0=1.55μm.

Let us consider MMIs with W_{MMI}=30μm and with required s_{min}=1.0μm and different N (See Table I). The maximum number of outputs for which [Fig. 4.2(a)] high quality self-imaging of the input is possible is N_{max}=11. For any N>11, the condition $W_{w,min} < W_e/N - s_{min}$ cannot be fulfilled. In other words, W_w is forced to be smaller than the $W_{w,min}$ value from Equation (4), as indicated in Table 4.I.

Figures 4.3(a-f) show the output field [abs(E_x)] profile of 1x6, 1x8, 1x10, 1x12, 1x14, and 1x16 MMIs, respectively. Figures 3(g) and (h) show the insertion loss and the output uniformity, respectively. Insertion loss is the ratio of the total output power to the input power. Uniformity is calculated as $10\log(P_{min}/P_{max})$, where P_{max} and P_{min} are the maximum and minimum power (norm of the fundamental mode) of the MMI output channels, respectively. In our simulations we let 75 modes to propagate in the multimode section. We noticed that increasing the number of modes resulted in less than 0.1% difference in the calculated insertion loss and uniformity values.

Figure 4.3 shows that as N increases, the degradation in the MMI performance is minimal as long as $W_w = W_{w,min}$. However, as W_w becomes increasingly smaller than the required $W_{w,min}$, the MMI performance is rapidly degraded due to increasing phase errors discussed before. One can note that the predicted N_{max}=11 from Equation (6) corresponds to the "knee point" in both the output uniformity and insertion loss versus the number of output channels (N). Therefore, the EME simulations are in good agreement with the theoretical predictions.

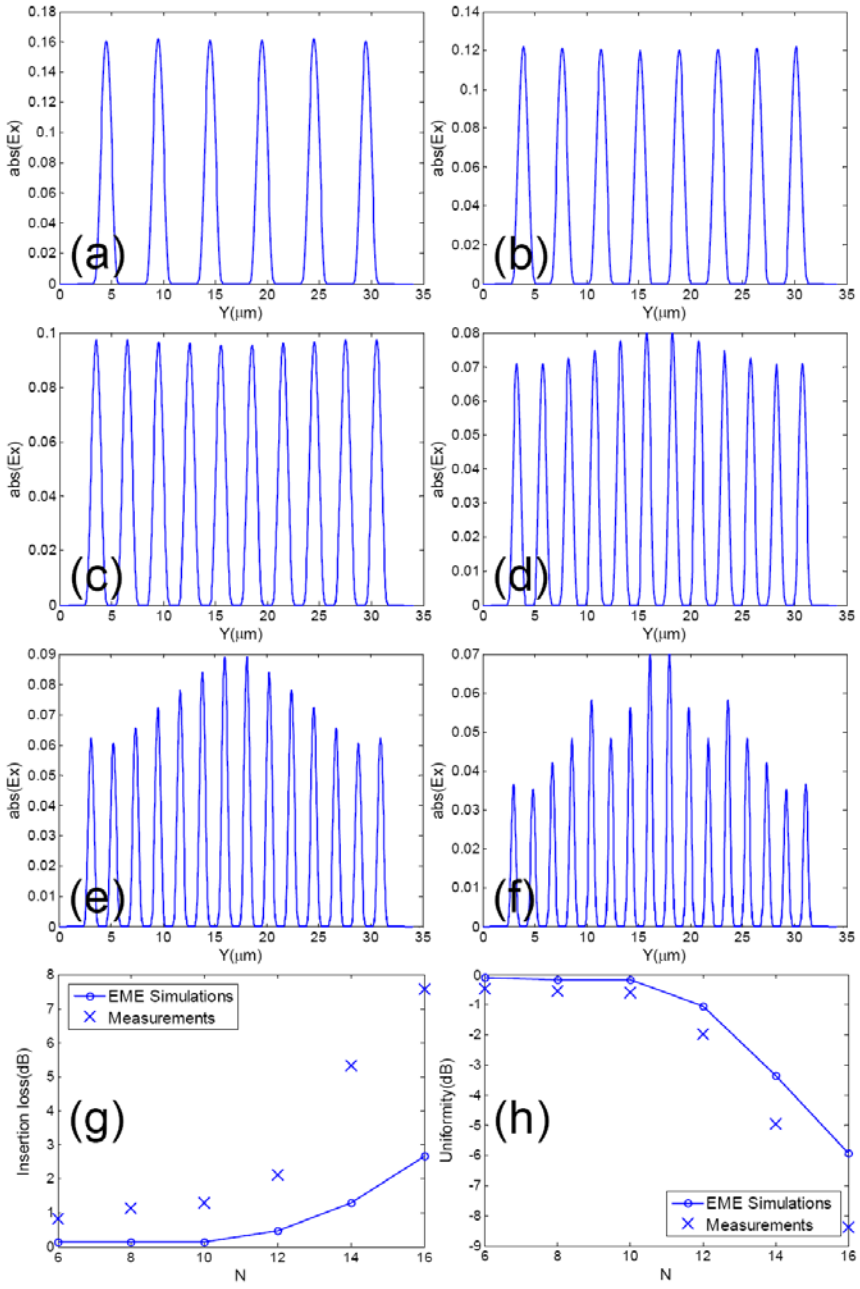

Fig. 4.3, (a-d) abs(E_x) at the MMIs' outputs in the middle of the output channel (height-wise). (e) Total (all channels) output power (normalized with respect to the input power) versus the output channel number (N). (f) Output uniformity versus output channel number.

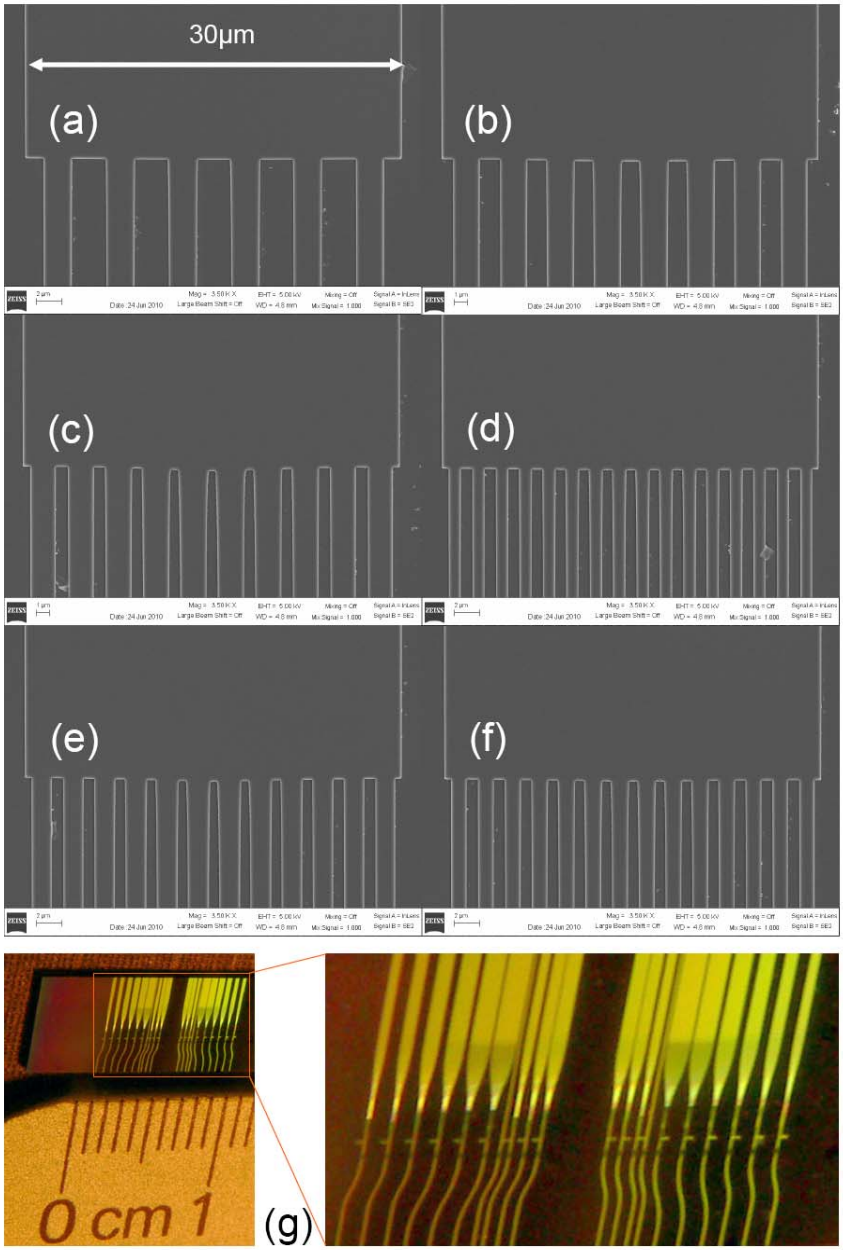

Fig. 4.4, SEM pictures of the fabricated SOI-based MMIs (a) 1x6, (b) 1x8, (c) 1x10, (d) 1x12, (e) 1x14, and (f) 1x16. (g) a picture of the entire chip showing different MMI devices. The input s-bends and the fanned-out output channels are on the bottom and top sides of the chip, respectively.

Experimental Data from Rib Waveguides

We fabricated 1x6, 1x8, 1x10, 1x12, 1x14, and 1x16 MMIs MMIs (W_{MMI}=30μm) with W_w and L_{MMI} values shown in Table I. The MMIs are fabricated on a silicon-on-insulator (SOI) substrate with 3μm buried oxide layer (BOX) and 250nm top silicon layer. Light oxidation creates a 45nm top oxide layer that will serve as an etch mask. This oxidation consumes 20nm of silicon, giving a final silicon layer of 230nm. The MMIs are patterned using a JEOL JBX600 electron beam lithography system, followed by an HBr/Cl_2 based reactive ion etching (RIE) and plasma-enhanced chemical vapor deposition (PECVD) of a 1μm thick silicon dioxide film for the top cladding. The refractive index of this PECVD cladding film was found to be n_{PECVD}=1.46.

All the input and output channels are tapered to 2.50μm to match the output coupling lensed fiber. There is an s-bend before each MMI input to avoid background noise from the input fiber during characterization of the output channels' near field. The output channels are fanned out for 30μm center-to-center separation so that we are able to capture clear images of the near field at the output waveguide facets using a 10X IR lens. SEM pictures of the fabricated MMIs and a picture of the SOI chip are shown in Fig. 4.4. Transverse-electric field from an external cavity tunable laser source is coupled into the input waveguides through a tapered and lensed polarization maintaining fiber (PMF). A CCD camera, connected to a tunable magnification IR lens (max 10X), captured top-

down images of the scattered light at the cleaved output waveguide facets as shown in Fig. 4.5.

In order to characterize the MMIs' performance, a single-mode output fiber is scanned at output side across each output channel cross-section for maximum output coupling. At least two samples of each MMI are tested. The results of the fiber-scanning measurements are summarized in Figs. 4.3(g) and (h).

As shown in Figs. 4.3(g) and (h) and Figs. 4.5(a-f), the MMIs' performance rapidly degrades with the number of output channels for $N>11$. Therefore, experiments also validate the theoretical predictions.

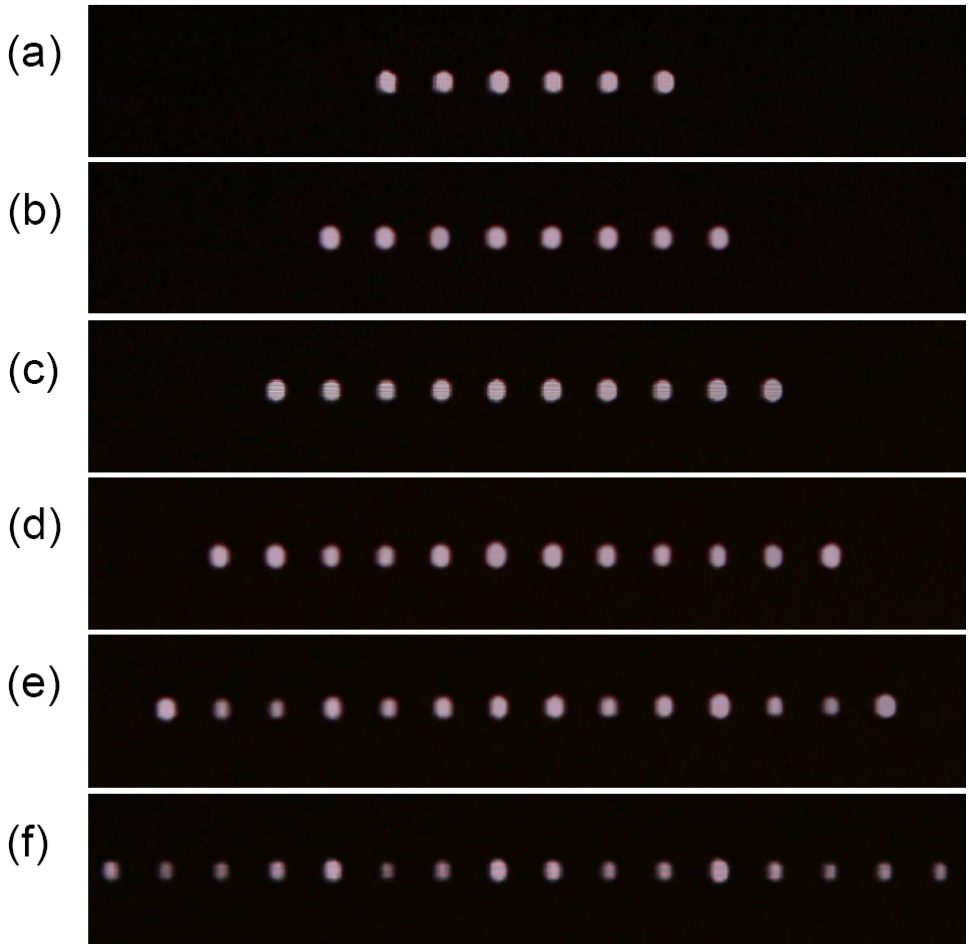

Fig. 4.5, Top-down IR-images of MMI outputs waveguides' facets for (a) 1x6, (b) 1x8, (c) 1x10, (d) 1x12, (e) 1x14, and (f)1x16. The channel-to-channel separations at the output facet is 30μm is all cases.

Summary

We derived a design rule for the maximum number of output channels of multimode interference based beam splitters. Highly accurate eigenmode expansion simulations confirmed the analytical relations for the maximum output channel number. Optical characterization of MMI beam splitter devices fabricated on SOI using silicon

nanomembranes experimentally demonstrate the validity of the theoretical predictions for maximum output channel number. Equations (4-6) can be used as a guideline for high performance on-chip optical beam splitter design.

References

1. R. Ulrich and T. Kamiya, "Resolution of self-images in planar optical waveguides," J. Opt. Soc. Am., vol. 68, pp. 583-592, 1978.
2. J.Z. Huang, R. Scarmozzino, and R.M. Osgood Jr. , "A new design approach to large input/output number multimode interference couplers and its application to low-crosstalk WDM routers ," Photonics Technology Letters, IEEE, vol. 10, no. 9, pp. 1292-1294, 1998.
3. R. M. Lorenzo, C. Llorenle, E. J. Abril, and M. López, "Improved self-imaging characteristics in 1xN multimode couplers," Proc. Inst. Elect.Eng. Optoelectron., vol. 145, no. 1, pp. 65–69, 1998.
4. L. Soldano and E. Pennings, "Optical multi-mode interference devices based on self-imaging: principles and applications," J. Lightwave Technology, vol. 13, no. 4, pp. 615–627, 1995.
5. M. Rajarajan, B.Rahman, T. Wongcharoen, and K. Grattan, "Accurate analysis of MMI devices with two-dimensional confinement," J. Lightwave Technology, vol. 14, no. 9, pp. 2078–2084, 1996.
6. A. Hosseini, D. N. Kwong, C.-Y. Lin, B. S. Lee, and R. T. Chen, "Output Formulation for Symmetrically-Excited one-to-N Multimode Interference Coupler," IEEE Journal of Selected Topics in Quantum Electronics, vol. 6, no. 1, pp. 53-60, 2010.
7. S. Sridaran and S. A. Bhave, "Nanophotonic devices on thin buried oxide Silicon-On-Insulator substrates," Opt. Express, vol. 18, pp. 3850-3857, 2010.
8. N. Sherwood-Droz, A. Gondarenko and M. Lipson, "Oxidized Silicon-On-Insulator (OxSOI) from bulk silicon: a new photonic platform," Opt. Express, vol. 18, pp. 5785- 5790, 2010.
9. Y. Shi, D. Dai, and S. He, "Improved performance of a silicon-on-insulator-based multimode interference coupler by using taper structures," Optics Communications, vol. 253, pp. 276-282, 2005.
10. R. Yin, J. Yang, X. Jiang, J. Li, and M. Wang, "Improved approach to low-loss and high-uniformity MMI devices," Optics Communications, vol. 181, pp. 317-321, 2000.
11. Q. Wang, J. Lu, S. He, "Optimal design of a multimode interference coupler using a genetic algorithm," Optics Communications, vol. 209, pp. 131-136, 2002.

12. D.F.G. Gallagher, T.P. Felici, "Eigenmode Expansion Methods for Simulation of Optical Propagation in Photonics – Pros and Cons." Proc. SPIE, vol 4987, pp.69-82, 2003.

Chapter 5: Silicon-on-Insulator Based Implementation for OPA

Optical Circuit Design and Simulations

The goals of the first phase of the MURI project include demonstration of a silicon nanomembrane based large angle (>60°) optical beam steering. Such steering system requires optical passive components and active phase shifters. Passive optical components have been designed for a silicon-on-insulator (SOI) implementation. The buried oxide layer and the silicon layer are 3μm and 260nm thick, respectively. The optical passive components are

1) 1x12 multimode interference (MMI) coupler

We have completed design, fabrication, and optical characterization of the 1x12 MMI coupler as explained previously (*D. Kwong et al, Elec. Device Lett., 2010*). In summary, this is the first large output MMI demonstrated on silicon nanomembrane (thickness=230nm, MMI width=60μm, MMI Length=553.4μm, access waveguide width=2.6μm). The resulting is a 1x12 MMI with less than 1dB insertion loss and better than 0.7dB output uniformity. The characterization was performed by both near field imaging from the output waveguide facet edges, and output fiber scanning.

2) Multimode-to-singlemode and waveguide tapers

The MMI outputs are 2.6μm. This is the optimum access waveguide width as explained previously. The access waveguides' widths need to be tapered down to 0.5μm for single mode operation (*A. Hosseini et al, Optics Lett., 2010*). After the tapers, the single mod waveguides are elongated to accommodate for the active phase shifters. The passive phase shifters follow next, which compensate for the MMI output phase profile (*A. Hosseini et al, IEEE J. of Sel. Topics in Quant. Elect., vol. 16, no. 1, 61-69, 2010*) and also the output s-bends that change the separation of the uniform waveguide array to that of the non-uniform array at the output.

3) 12-element non-uniform array

For the single layer prototype, we designed a non-uniform design (*A. Hosseini et al, IEEE J. of Sel. Topics in Quant. Elect., vol. 15, no. 5, pp. 1439-1446, 2009*). The first prototype consists of 3 sub-arrays. Each sub-array is a uniform 4-element array. The center-to-center separation in each sub-array is 2λ, 2.5λ and 3.5λ, where λ=1.55μm is the operating wavelength. The total array size is 46.5μm.

In Chapter 2, it was shown that the uniform array enter-elements spacing ($\lambda/2 \sim 800nm$) between adjacent optical waveguide required for large angle beam steering is prohibited by the fact that strong optical coupling between close waveguides severely distorts the signal. Therefore, we switch to a non-uniform array at the penalty of larger side-lobe-levels (SLL). SLL can be decreased by increasing the number of array elements. Here, to start with, we choose N=12, which is the smallest N that can provide SLL better than -6dB at $\theta=0^{\circ}$.

The shortest spacing between the array waveguides is s_1=3.1μm, which has been selected

to be large enough to avoid optical coupling.

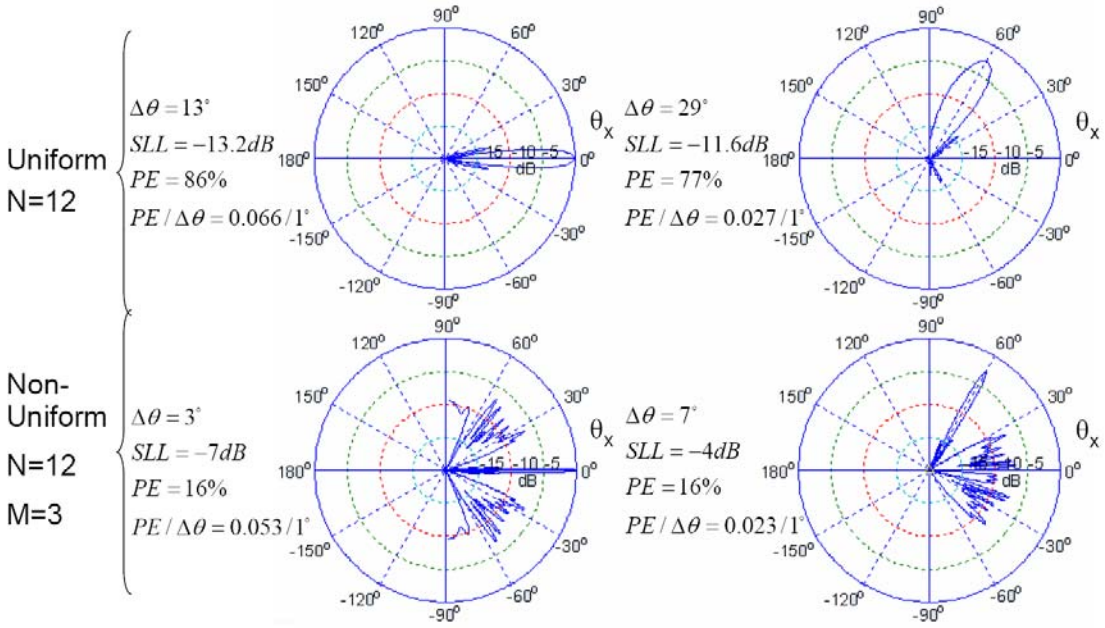

Fig. 5.1, Far-field radiation pattern at $\theta=0^{\circ}$ and $\theta=60^{\circ}$ for a 12-element uniform array of $\lambda_0/2$ spacing and the designed non-uniform array with 3 sub groups of each 4 array elements.

Figure 5.1 compares the array performance of the non-uniform array design with that of a uniform array with the same number of elements (N=12) and spacing of 0.775μm. The uniform array, though physically impossible to be implemented, provides better SLL as expected. It also provides better power efficiency (PE) defined as the ratio of the power inside the main lobe to the power radiated in all the angles. However, the non-uniform array is superior in terms of the beam-width due to its total larger size. An important observation is that although the non-uniform array has a much worse PE compared to that of the uniform array, the power radiated unit length inside the main lobe is almost the

same in both cases due to the much smaller beam width of the non-uniform array.

It is necessary to ensure that whenever no voltage is applied to the phase shifters, the beam is directed at $\theta=0^{\circ}$. This means that without the operation of the phase-shifters, all the channels must be in-phase, or all the array elements must be fed with the same phase.

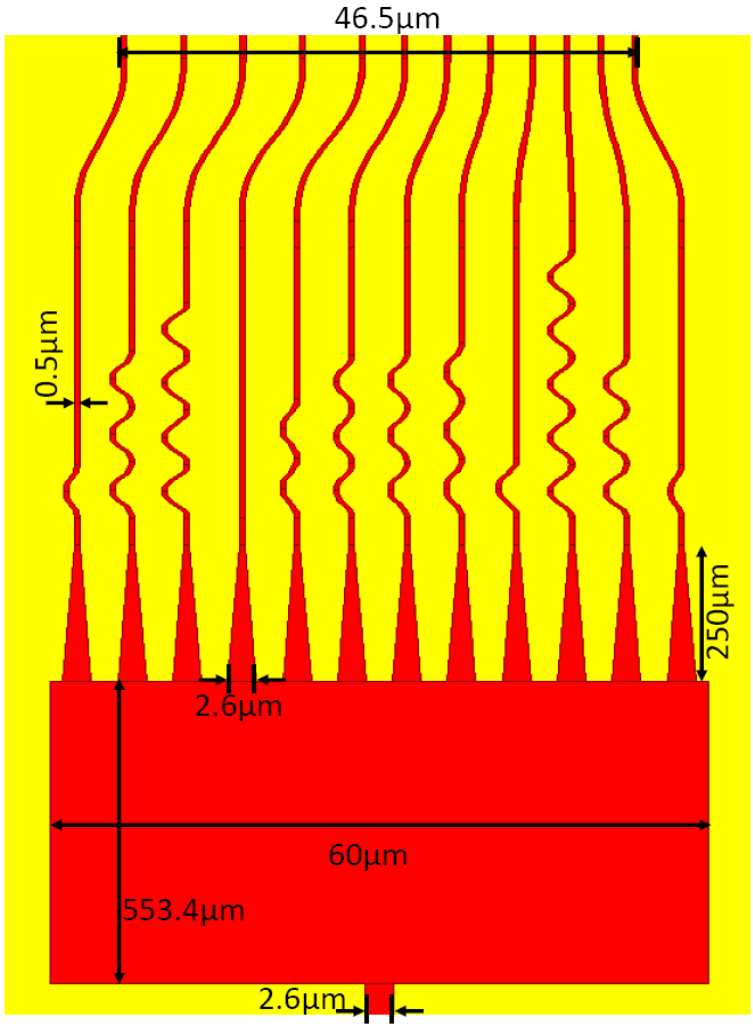

Fig. 5.2, Optical circuit layout.

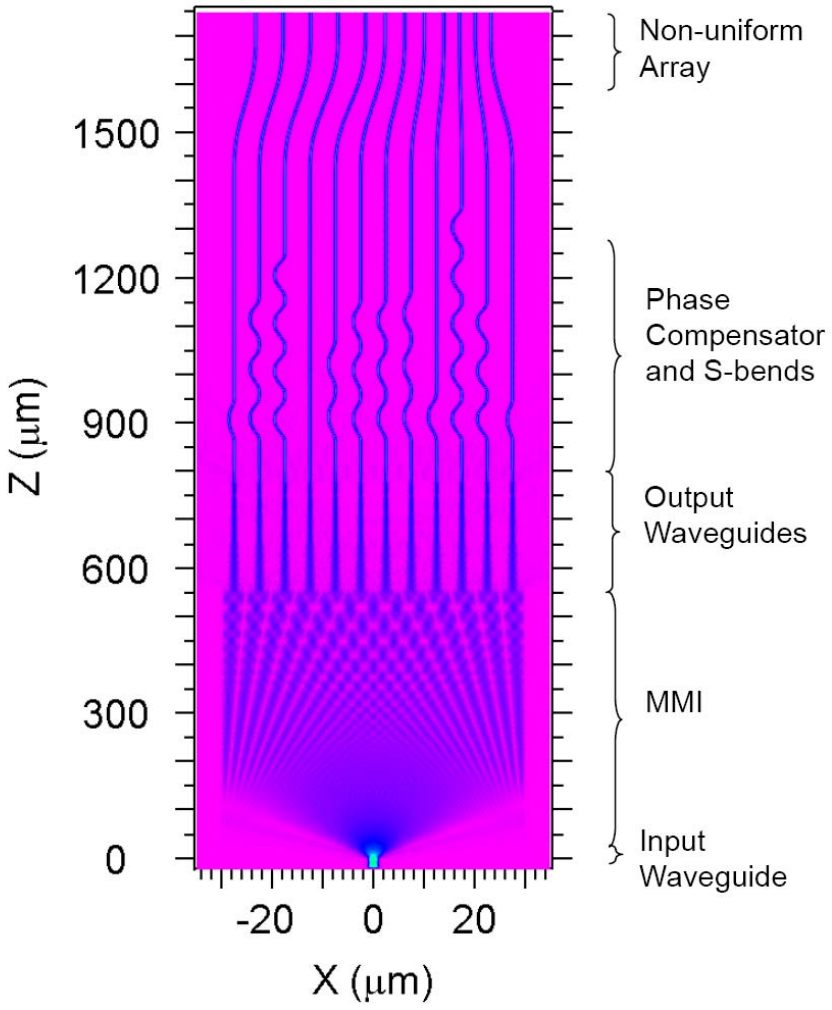

Fig. 5.3, Beam propagation simulation of the optical circuit shown in Fig. 5.2.

The non-uniform array is obviously a non-symmetric structure and this means that no symmetric optical circuit can be used and therefore, and any feasible optical circuit design would feed the array elements without a uniform phase. The extra waveguiding paths added to different channels for in-phase excitation constitute the passive phase shifters.Figure 2 shows the layout of the optical circuit design. The zigzag shaped bends

are passive phase shifters to compensate for the quadratic MMI output phase profile, which was investigated in Chapter 3, and also for the asymmetry in the structure. Figure 3 shows Beam Propagation simulation of the optical circuit using the BeamProb^{TM} from Rsoft Photonics. Different sections of the optical circuit are labeled in Fig. 3. In order to accommodate the phase shifters, the section between the tapered waveguide array and the zigzag S-bends is elongated in the final mask implementation.

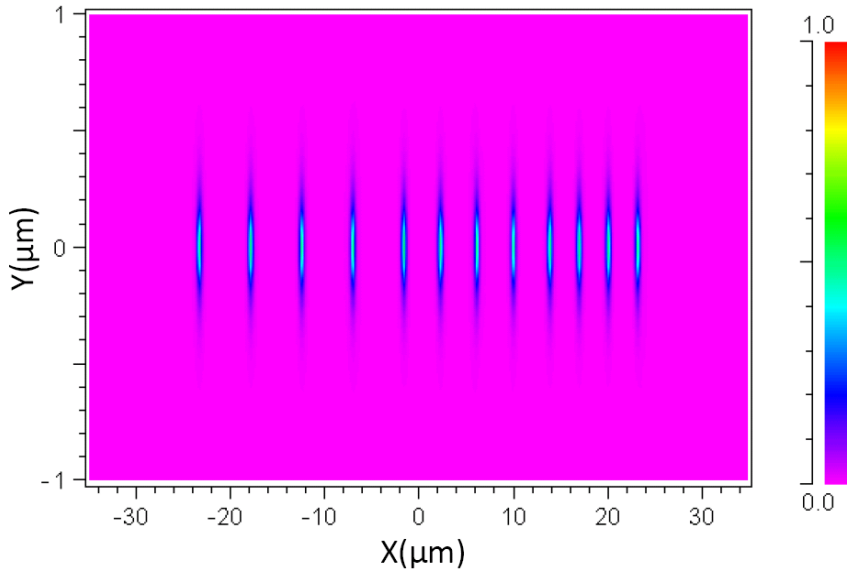

Fig. 5.4, Cross section (X-Y) electric field (E_x) profile at the non-uniform array part of Fig. 5.3.

In order to make sure that the uniformity of the power distribution in all the channels, we investigate the output power in each channel. Figure 4 shows the field profile (E_x) at the output of the non-uniform array section. Uniformity is defined as

$$Uniformity = 10Log\left(P_{\min} / P_{\max}\right). \quad (1)$$

In Fig. 5.4, uniformity is -0.6dB, which confirms that the optical coupling between

channels and the bend losses are negligible. Figure 5 demonstrate the frequency response of the designed OPA in terms of the insertion loss 5.5(a), output power uniformity 5.5(b), and output phase uniformity 5.5(c-d). Note that the insertion loss and output uniformity are determined by the 1x12 MMI coupler. The output phase in determined by both the 1x12 MMI coupler and the s-bends.

Electrical Circuit Design of the phase shifters

The active control of the phase shift in each individual channel can be done is several ways by changing the refractive index and therefore the accumulated phase at the end of each channel. Depending on the waveguiding structure, electro-optic effects (Pockel's effect and Kerr effect, plasma dispersion effect) and thermo-optic effect can be chosen for phase control. In the first phase of the project, we have decided to use the thermo-optic effect because of the ease of fabrication. Each phase shifter is a metallic wire placed near the silicon waveguide to heat it up depending on the voltage applied to its two ends. Also there is no need for doping anymore.

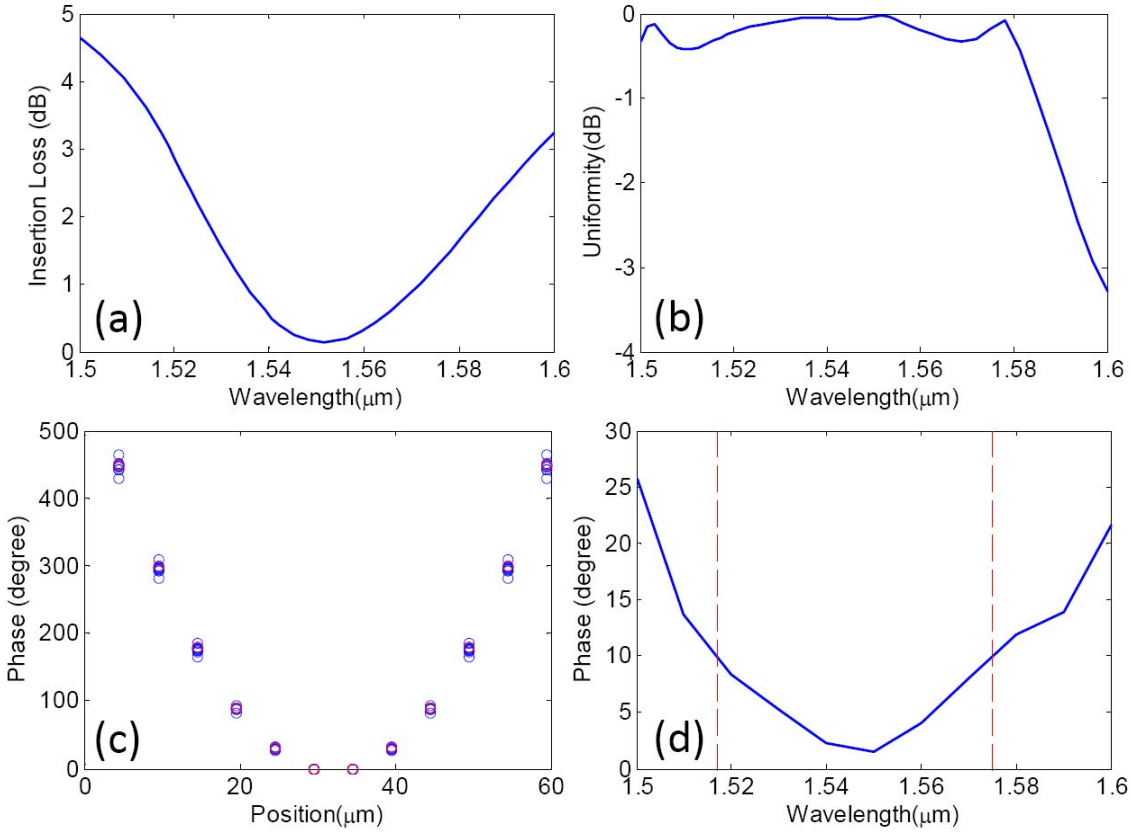

Fig. 5.5, Frequency response analysis of the designed OPA. (a) 1x12 MMI coupler insertion loss versus wavelength, (b) 1x12 MMI coupler output uniformity versus wavelength. (c) variations of the output phase of the 1x12 MMI coupler as the wavelength changes from 1.50μm to 1.60μm for all the output ports. The red circles indicate the ideal output phase values. (d) Variations of the maximum output phase difference versus wavelength. The dashed red lines show the bandwidth over which the maximum output phase difference is within 10°.

Remember from Chapter 2 that in both uniform and non-uniform arrays, the required phase shift for the i^{th} channel ($\Delta\theta i=\theta_i-\theta_0$), where θ_i and θ_0 are the phase values of the i^{th} and 0^{th} channels, respectively, is proportional to position of the i^{th} channel with respect to the 0^{th} channel (d_i). In other words, $\Delta\theta_i/d_i$ is constant. We know that in the case of a uniform array with $\lambda_0/2$ spacing, the required phase shift between the two adjacent array

elements is π. This means that it the case of the non-uniform array design presented in the previous section, the required phase shift between the two channels placed at the two ends is (48μm/0.8μm)×π=60π. This means that if we use only two electrodes to control the phase shift of all the channels, such as the case in [1], where a triangular heater linearly changes the phase of each channel without any reset, the amount of the phase shift required is absolutely prohibitive. That is the reason why in [1] the beam steering angle is far less than its theoretical limit imposed by the inter-element spacing as shown in Chapter 1. In the case of the non-uniform array the problem is significantly more severe due to the large size of the array.

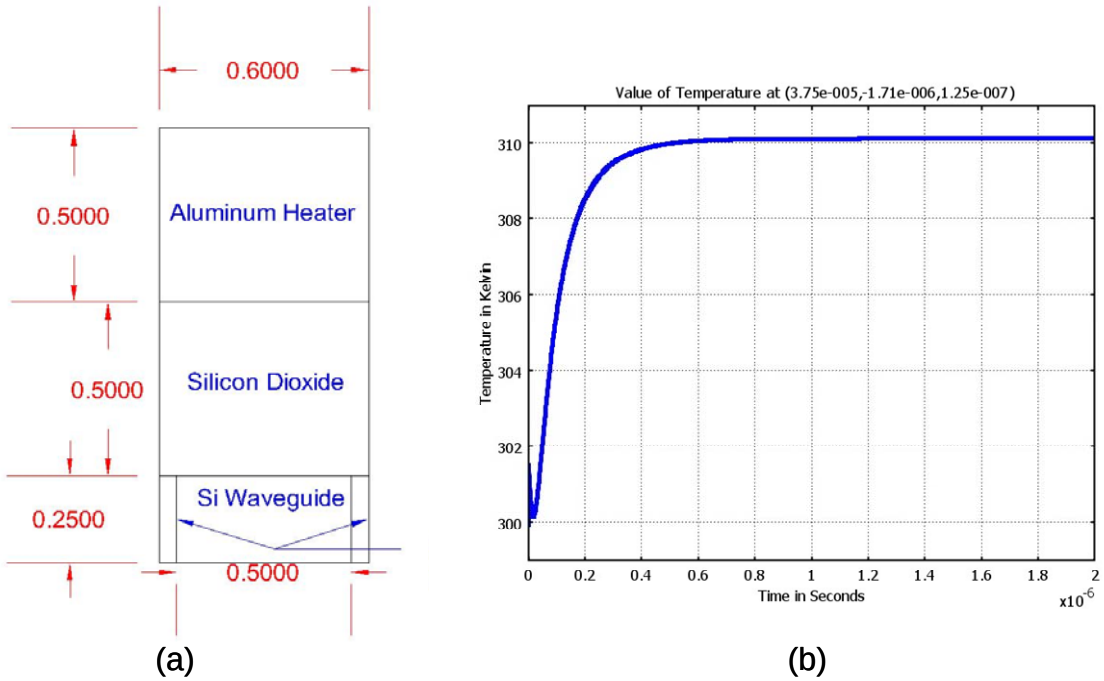

Fig. 5.6, (a) A cross section of the heater, (b) Si waveguide temperature versus time from transient simulations.

However, we notice that 60π phase difference is equivalent to 0rad. Thus, if each phase shifter is independently controllable, the maximum required phase shift is never more than 2π in general, and in our case where $s_0 = \lambda_0/2$, is not more than π, simply because the phase shift can be reset after each additional 2π. Such individual control over the phase shifter associated with each channel significantly reduces the required length of the phase shifter components. However, at least (N+1) electrodes are needed for such full control, and this complicates the fabrication of the electrical circuitry.

The heaters and the electrodes of the phase shifters have been designed and simulated by my colleague, David Kwong. For the sake of completeness I briefly review his design. The thermo-optical phase shifters consist of aluminum heaters shown in Fig. 5.6(a). Aluminum heaters have 600nm×500nm cross-sections. A layer of silicon-oxide separates the heater from the silicon waveguide by 500nm to avoid optical loss by the conductive heater. The two sides of each heater are deeply etched to realize a structure that efficiently directs the generated heart toward the waveguide. Using COMSOL Multi-Physics simulations we estimated that the maximum power required for each heater is about 30mW. The time-transit simulations predicted that the rise time is ~0.5ms as shown in Fig. 5.6(b). The electrode layout including the bonding pads are shown in Fig. 5.7.

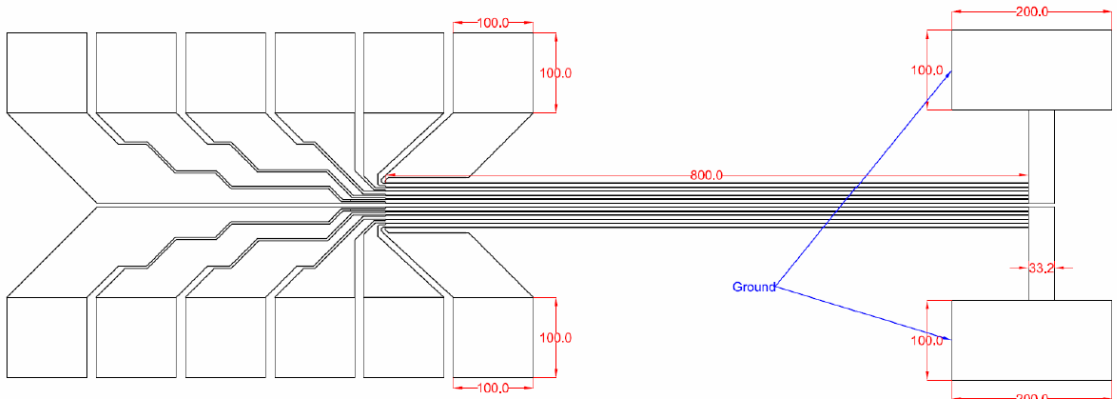

Fig. 5.7, Layout of the electrical circuit.

Fabrication

The MMIs were patterned using a JEOL JBX600 electron beam lithography system (*D. Kwong et al, Elec. Device Lett., 2010*). A nickel liftoff step was used to invert the pattern, and subsequently transferred to the top silicon layer via an HBr/Cl_2 based reactive ion etching (RIE). A subsequent piranha clean has the dual purpose of providing a clean sample, but more importantly, removing the nickel etch mask. Afterwards, a 1µm film of plasma-enhanced chemical vapor deposition (PECVD) silicon dioxide was deposited using the Plasmatherm 790 system for top cladding as well as passivation. The refractive index of the PECVD $Si0_2$ film was found to be $n_{PECVD(Si02)}$=1.46. The whole device including the electrodes and the bonding bands are shown in Figure 5.8.

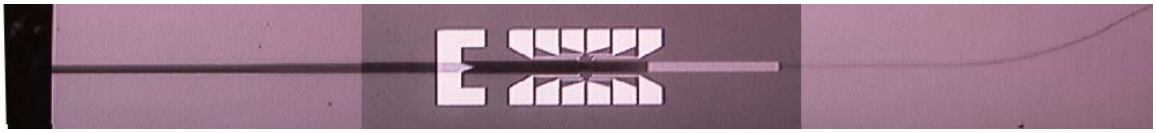

Fig. 5.8, A top-down view of the fabricated photonic circuit of the optical phased array and the electrical circuit of the active phase shifter on top.

Optical Characterization

Because of the small size of the output, we used a 100X IR microscope lens mounted to face the output waveguide facets. The microscope is connected to an IR camera for near field imaging. We used a visible top-down camera to adjust the position of a lensed fiber for input coupling using a six-axis automated aligner system. A second IR camera connected to a variable magnification IR objective lens monitors the position of the output waveguide fields to adjust the 100X IR microscope lens. Figure 5.9 shows the optical test setup. In the input is TE polarized light from a polarization maintaining lensed fiber (PMF) with a 2.5μm output mode diameter.

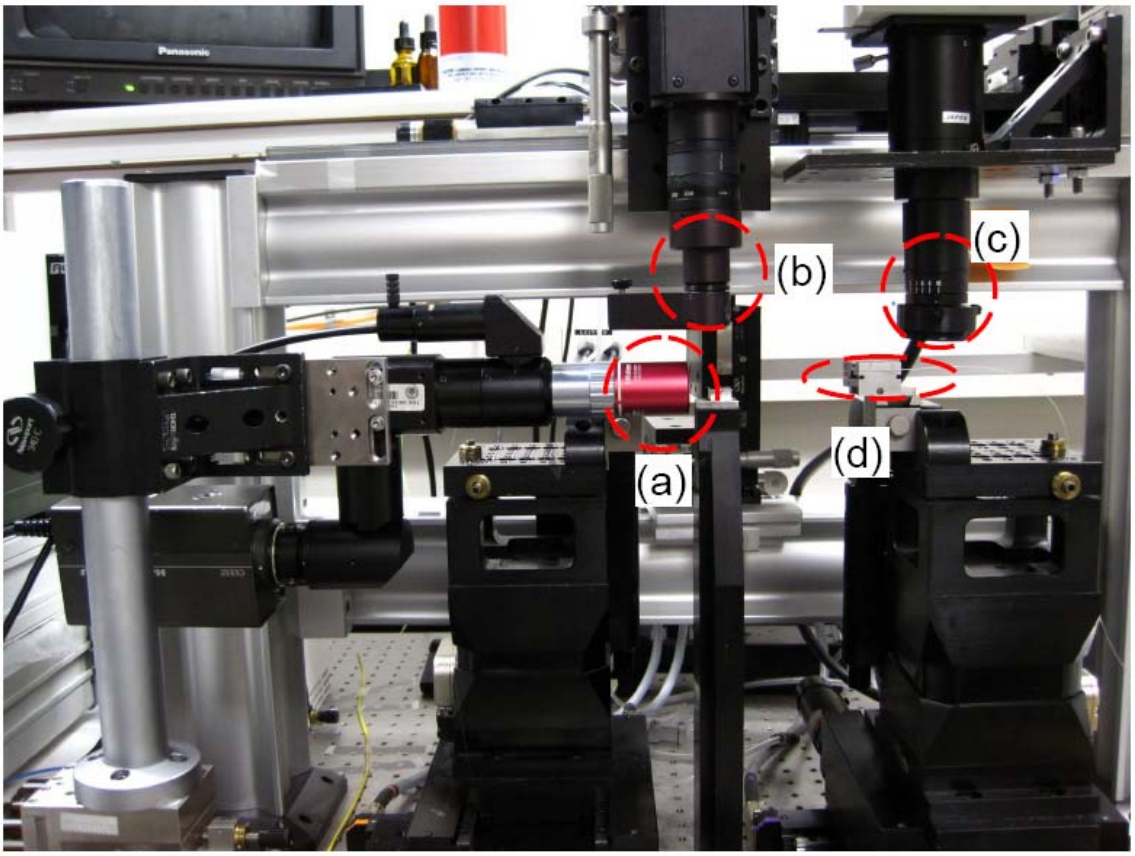

Fig. 5.9, Test setup for silicon nanomembrane optical phased array. (a) 100X objective IR lens, (b) variable magnification visible objective lens, (c) variable magnification IR objective lens, (d) input lensed fiber.

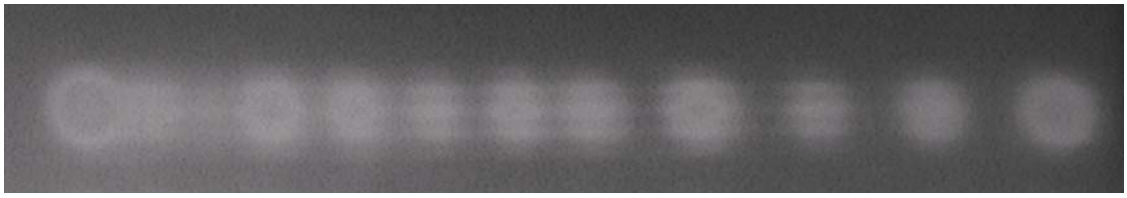

Fig. 5.10, Near field image from the optical phased array waveguide facets.

Figure 5.10 shows the near field image taken by the IR camera connected to the 100X objective lens. The figure shows the non-uniform spacing of the waveguide array outputs. Note that the magnification is not enough to completely resolve the light sports

associated with the sub-array with the smallest spacing (3.1μm). The uniformity of the outputs can be verified by the uniformity of the 1x12 MMI outputs. and the uniformity of the passive phase shifter plus the output s-bend section.

Reference

1. K. Van Acoleyen, W. Bogaerts, J. Jágerská, N. Le Thomas, R. Houdré, and R. Baets, "Off-chip beam steering with a one-dimensional optical phased array on silicon-on-insulator," Opt. Lett., vol. 34, pp. 1477-1479, 2009.

Chapter 6: Theoretical Formulation of Two-dimensional Far-Field and Beam Steering in Slab Waveguide

Two-dimensional far field formulation

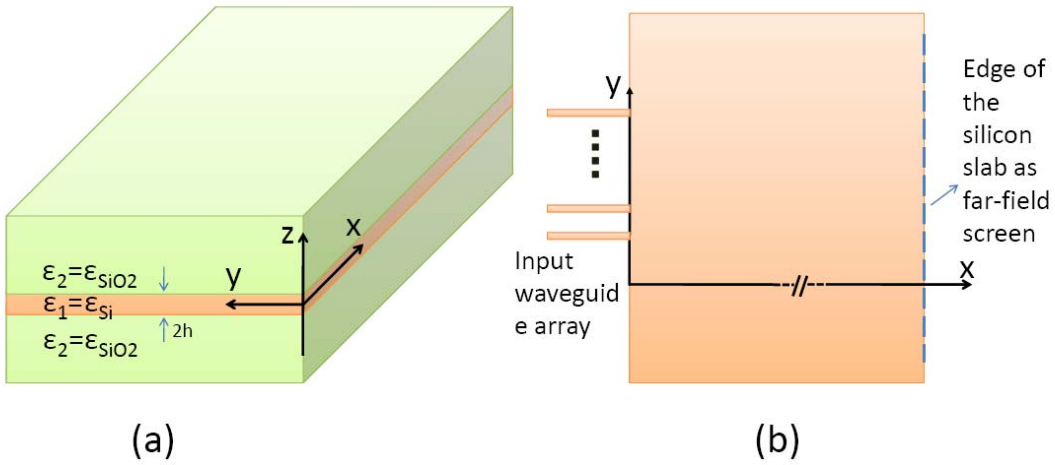

Fig. 6.1, Geometry of the silicon slab waveguide. (b) a schematic of the waveguide array connected to a large slab waveguide.

In this section, we solve for spherical field radiated from a point source in the slab waveguide. The vertically symmetric structure shown in Fig. 6.1 is well-known to support the Transverse Electric (TE, $E_x=E_z=H_y=0$) mode without a thickness cut-off. Thus, we focus on TE-polarized propagations and the point source is given as

$E_y = \cos(\beta_z z)\,\delta(x)\delta(y)$. All the equations are written for the field in the core region, $|z| \ll h$. Consider slab guide TE (E_x=E_z=H_y=0) polarized

$$E_y = \frac{1}{\beta_x}\cos(\beta_z z)\exp\left(-j\beta_y y\right)\exp(-j\beta_x x)$$

where, the dispersion relation is given as $\left(h\sqrt{\varepsilon\mu\omega^2-\beta_\rho^2}\right)\tan\left(h\sqrt{\varepsilon\mu\omega^2-\beta_\rho^2}\right)=\left(-jh\sqrt{\varepsilon_0\mu\omega^2-\beta_\rho^2}\right)$, where $\beta_x^2+\beta_y^2=\beta_\rho^2$. One can show that the abovementioned field can be radiated by an impresses linearly phased line source along the y-axis in the form of

$$E_y = -2j\cos(\beta_z z)\exp\left(-j\beta_y y\right)\delta(x)$$

Since, $\delta(x)\delta(y)=\frac{1}{2\pi}\delta(x)\int_{-\infty}^{+\infty}\exp\left(-j\beta_{1y}y\right)d\beta_y$, the field emitted from a point source in the slab is given as

$$\int_{-\infty}^{+\infty}\frac{j}{4\pi\beta_x}\cos(\beta_z z)\exp\left(-j\beta_{1y}y\right)\exp(-j\beta_x x)\,d\beta_y$$

In order to calculate this integral, we notice that

$$B\mathrm{H}_0^{(2)}(\beta_\rho\rho,\varphi)=\frac{1}{\pi}\int_{\left(\frac{\pi}{2}\right)-j\infty}^{\left(\frac{3\pi}{2}\right)+j\infty}\exp\left[j\beta_\rho\rho\cos(\alpha-\varphi)\right]d\alpha$$

where, (ρ,φ,z) is the cylindrical coordination [1]. By changing variables, $\beta_x=\beta_\rho\sin(\alpha)\rightarrow d\alpha=\frac{d\beta_x}{\sqrt{\beta_\rho^2-\beta_x^2}}$ and $\beta_y=-\beta_\rho\cos(\alpha)$, one can show that [appendix 1],

$$\int_{\beta_y=-\infty}^{\beta_y=+\infty}\exp(-j\beta_x x)\exp\left(-j\beta_y y\right)\frac{1}{\beta_{1x}}d\beta_y=\pi\mathrm{H}_0^{(2)}(\beta_\rho\rho)$$

Therefore,

$$\int_{-\infty}^{+\infty} \frac{j}{4\pi\beta_x} \cos(\beta_z z) \exp\left(-j\beta_{1y} y\right) \exp(-j\beta_x x)\, d\beta_y = \frac{j}{4\pi} H_0^{(2)}\left(\beta_\rho \rho\right) \cos(\beta_z z)$$

The result is also consistent with 2D green function, $G(x,y) = \frac{j}{4\pi} H_0^{(2)}\left(k\sqrt{x^2+y^2}\right)$, which is the solution to $\nabla^2 G + k^2 G = \delta(x,y)$. Therefore, the fundamental spherical waveguide propagation constant (β_ρ) is the same as that of plane waves in the slab.

In order to find the far field radiation of a collection of line sources in the form of $\cos(\beta_z z)\,\delta(x)\delta(y)$, we notice that [2]

$$H_0^{(2)}(\beta_\rho \rho) \sim \sqrt{\frac{2j}{\pi\beta_\rho \rho}} \exp(-j\beta_\rho \rho) \quad \text{for } \beta_\rho \rho \gg 0 \ .$$

$\rho = |\bar{\rho} - \bar{\rho}'| \sim |\bar{\rho}|$ for $|\bar{\rho}| \gg |\bar{\rho}'|$, where, $\bar{\rho}$ and $\bar{\rho}'$ are two position vectors (in the x-y plane) of the observation point and the source, respectively. In the phase term:

$$\rho = |\bar{\rho} - \bar{\rho}'| \sim |\bar{\rho}| - |\bar{\rho}'|\cos(\varphi - \phi) + \frac{|\bar{\rho}'|^2}{2|\bar{\rho}|} \sim |\bar{\rho}| - |\bar{\rho}'|\cos(\varphi - \phi) \quad \text{for } \beta_\rho \frac{|\bar{\rho}'|^2}{2|\bar{\rho}|} \ll 1$$

Therefore, the far field conditions are similar to those of the 3D case:

1- $\beta_\rho \rho \gg 0$, or the effective wavelength should be much smaller than the observation distance

2- $|\bar{\rho}| \gg |\bar{\rho}'|$, or the whole scattering object size (or the array size) should be much smaller than the observation distance.

3- $\beta_\rho \frac{|\bar{\rho}'|^2}{2|\bar{\rho}|} \ll 1$, for the phase condition.

Here, we note that at an observation point in the far field zone the local field appears to be a slab (TE) mode, for which dissimilar to the familiar far field in free space, the orthogonality of the electric, magnetic field and the propagation direction does not hold. In other words, the far field is not a TEM mode, for which $\beta^2 = \omega^2 \mu\varepsilon$. Without lack of generality, let's consider an observation point in the far field zone on the near the x-axis (y<<x, |z|<h). We can represent the propagating field in a transmission line format using a similar approach as in [3]. The transmission line (per unit length) voltage and current are defined as:

$$V = E_y\Big|_{z=0}$$

$$I = -H_x\Big|_{z=0}$$

which satisfy the standard transmission line equations:

$$\frac{dV}{dx} = \frac{\partial E_y}{\partial x}\Big|_{z=0} = -j\omega\mu H_x\Big|_{z=0} = j\omega\mu I$$

$$\frac{dI}{dx} = -\frac{\partial H_x}{\partial x}\Big|_{z=0} = j\omega\varepsilon E_y\Big|_{z=0} - \frac{\partial H_x}{\partial z}\Big|_{z=0} = j\omega\varepsilon_{eff} V$$

where,

$$\varepsilon_{eff} = \varepsilon - \frac{\partial H_x / \partial z\Big|_{z=0}}{j\omega E_y\Big|_{z=0}}$$

Thus, the effective permittivity is modified by presence of the component of the magnetic field parallel to the propagation direction. The dispersion relation for the modes in the far field is given as

$$\beta_n^2 = \omega^2 \mu\varepsilon_{eff} .$$

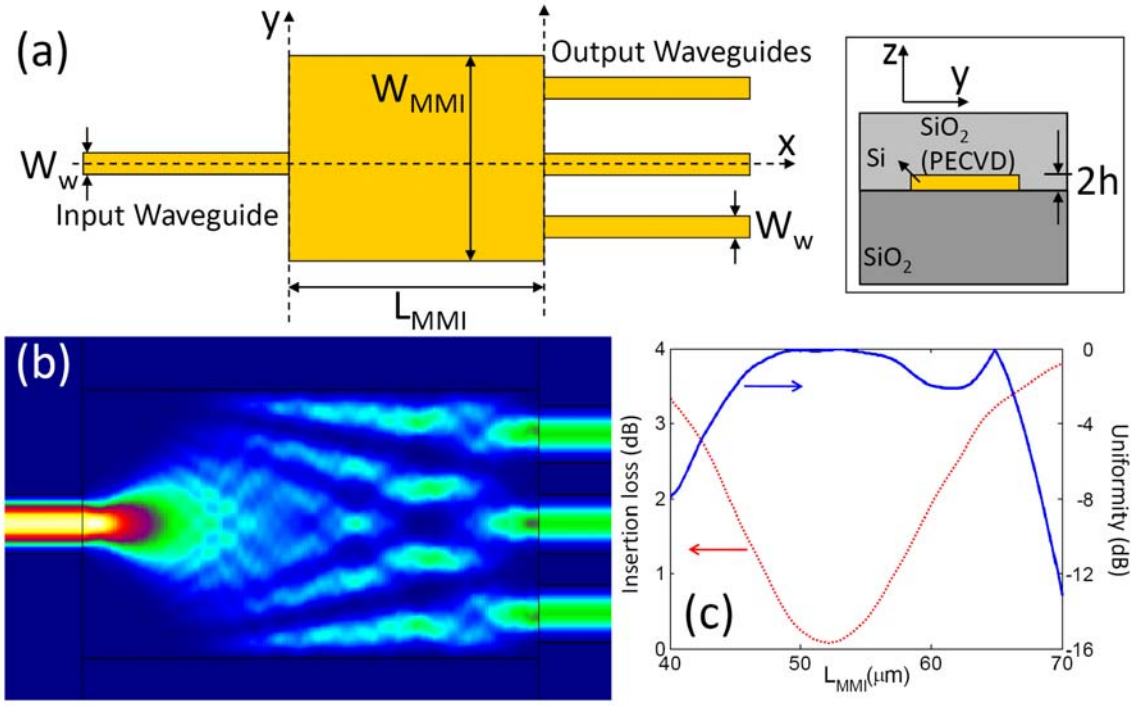

Fig. 6.2, (a) A schematic of the 1x3 MMI used for the far field test. The inset shows the cross section of the waveguiding structure. Access waveguide width W_w=2μm, MMI width W_{MMI}=9.3μm, MMI length L_{MMI}=52.5μm and the MMI thickness 2h=0.23 μm. (b) Eigenmode decomposition based simulation of the designed 1x3 MMI. (c) Calculated output uniformity and insertion loss of the designed MMI.

Experimental observation of 2D far field

In Fig. 6.1(b) At x=0, where the MMI outputs are connected to the slab waveguide, the waveguides' facets can be treated as integration of 2D point sources, and thus, the radiation field of the optical phased array at z=0 can be calculated as:

$$\sum_{n=1}^{N} \int_{-\frac{W_e}{2}}^{+\frac{W_e}{2}} \frac{jA}{4\pi} \exp(-j\varphi_n) H_0^{(2)}\left(\omega\sqrt{\mu\varepsilon_{eff}}\left|\bar{\rho} - \overline{d_n} - y\right|\right) dy$$

where, N is the number of array element, *We* is the effective width of a waveguide including the penetration depth due to the Goose-Hahnchen shift, $\overline{d_n}$ is the position (center) of the array elements, φ_n is the input phase of the n^{th} array waveguide. This can be simplified as explained in the previous section.

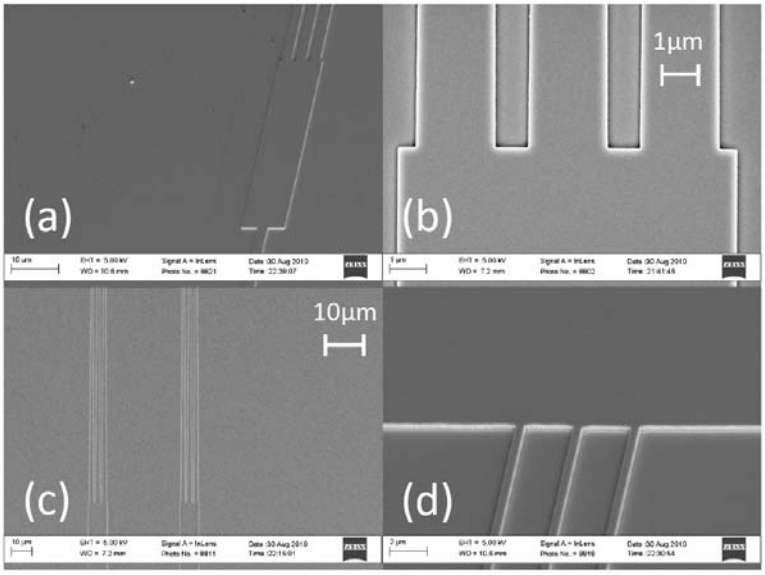

Fig. 6.3, SEM images of (a) 1x3 MMI coupler, (b) 1x3 MMI coupler output, (c) output waveguides width tapers, and (d) MMI outputs connections to the slab waveguide.

In order to validate the theoretical result, we design and fabricate 1x3 multimode interference (MMI) couplers. A schematic of a 1x3 MMI coupler is shown in Fig. 6.2. The input and output access waveguide width are design wide enough to ensure near ideal self-imaging behavior [4]. The MMI output waveguides' phase values are given as $\theta_q = \frac{N-1-4q^2}{4N}\pi$ [5]. where N is the number of MMI output ($N=3$) and q is the port number as shown in Fig. 6.2. For 1x3 MMIs, the middle output waveguide has a 60°

phase lead compated to the two side ones. The MMI output waveguide width are finally tapered to 500nm for single mode operation. Figure 6.2(b) shows the MMI coupler simulations by vectorial eigenmode expansion simulator in the FIMMPROP^{TM}. The variations of the output uniformity and insertion loss are shown as a function of the input wavelength are shown in Fig. 6.2(c).

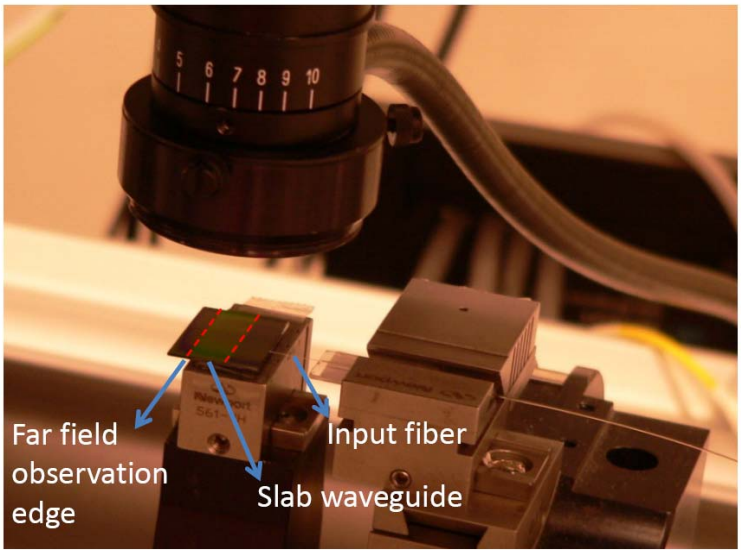

Fig. 6.4, Optical test setup. The slab waveguide region on the chip is 8.0mm long and is indicated by dashed lines.

The MMIs are fabricated on a silicon-on-insulator (SOI) substrate with 3μm buried oxide layer (BOX). The MMIs are patterned using electron beam lithography, followed by reactive ion etching (RIE), lift-off pattern inversion, and plasma-enhanced chemical vapor deposition (PECVD) of a 1μm thick silicon dioxide film for the top cladding. The silicon nanomembrane thickness $2h$=230nm. SEM pictures of the fabricated MMIs are shown in Fig. 6.3.

The MMIs outputs are connected to a wide and long silicon slab waveguide. The resulting far field beam is detectable at the exterior edge of the silicon nanomembrane. The silicon nanomembrane is etched away from the chip edge. This separates the background noise from the light coupled into the silicon substrate. Transverse-electric (TE) field from an external cavity tunable laser source is coupled into the input waveguides through a tapered and lensed polarizations maintaining fiber (PMF). A CCD camera captured top-down images of the scattered light at the etched silicon nonmember as shown in Fig. 6.4.

Figure 6.5 demonstrates the observed to dimensional far field and compares that the theoretical far field.

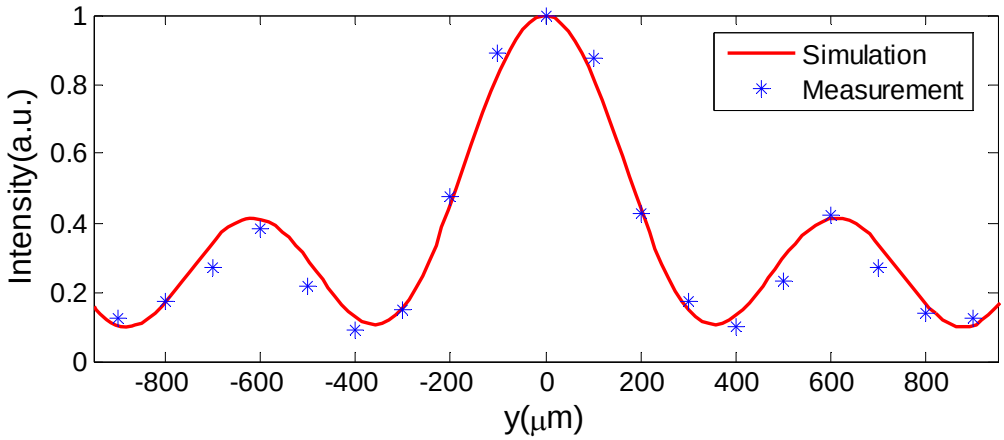

Fig. 6.5, Two-dimensional far field pattern of a 1x3 MMI with 3.1μm separation between the output waveguides.

Summary

We present the far field modeling for two-dimensional (2D) propagation in slab waveguides. The far field conditions and field formulations are derived. Using an analogy

to the transmission line theory, we compare the 2D and 3D far field presentations. In order to experimentally observe the 2D far field pattern, we fabricate a 1x3 multimode interference (MMI) coupler on silicon nanomembrane. The MMI outputs are connected to a slab silicon waveguide and the far field is observed at the edge of the silicon slab. The results can be used in design of optical phased array based optical switches in integrated photonics such as [6].

Proof I

Now, let's consider an integral form for the Hankel function. We know that [1]

$$\mathbf{H}_0^{(2)}(\beta_\rho\rho,\varphi) = \frac{1}{\pi}\int_{(\frac{\pi}{2})-j\infty}^{(\frac{3\pi}{2})+j\infty} \exp\left[j\beta_\rho\rho\cos(\alpha-\varphi)\right]d\alpha = \frac{1}{\pi}\int_{(-\frac{\pi}{2})-j\infty}^{(\frac{\pi}{2})+j\infty} \exp\left[-j\beta_\rho\rho\cos(\alpha-\varphi)\right]d\alpha$$

$$= \frac{1}{\pi}\int_{(0)-j\infty}^{(\pi)+j\infty} \exp\left[-j\beta_\rho\rho\sin(\alpha-\varphi)\right]d\alpha$$

$$= \frac{1}{\pi}\int_{(0)-j\infty}^{(\pi)+j\infty} \exp\left[-j\beta_\rho\rho\sin(\alpha)\cos(\varphi)\right]\exp\left[+j\beta_\rho\rho\cos(\alpha)\sin(\varphi)\right]d\alpha = \frac{1}{\pi}\int_{(0)-j\infty}^{(\pi)+j\infty} \exp\left[-j\beta_\rho x\sin(\alpha)\right]\exp\left[+j\beta_\rho y\cos(\alpha)\right]d\alpha$$

Now, $\beta_{1x} = \beta_\rho\sin(\alpha) \rightarrow d\alpha = \dfrac{d\beta_{1x}}{\sqrt{\beta_\rho^2-\beta_{1x}^2}}$ and $\beta_{1y} = -\beta_\rho\cos(\alpha)$

$$\mathbf{H}_0^{(2)}(\beta_\rho\rho,\varphi) = \frac{1}{\pi}\int_{\alpha=(0)-j\infty}^{\alpha=(\pi)+j\infty} \frac{\exp\left[-j\beta_\rho x\sin(\alpha)\right]\exp\left[j\beta_\rho y\cos(\alpha)\right](d\beta_{1x})}{\sqrt{\beta_\rho^2-\beta_{1x}^2}}$$

$$\pi \ll \alpha \ll (\pi)+j\infty \rightarrow -j\infty \ll \beta_{1x} \ll -j0 \ \ and \ \ \beta_\rho \ll \beta_{1y} \ll +\infty$$

$$\frac{\pi}{2} \ll \alpha \ll (\pi) \rightarrow 0 \ll \beta_{1x} \ll \beta_\rho \ and \ +0 \ll \beta_{1y} \ll \beta_\rho$$

$$0 \ll \alpha \ll \left(\frac{\pi}{2}\right) \rightarrow 0 \ll \beta_{1x} \ll \beta_\rho \ and \ -\beta_\rho \ll \beta_{1y} \ll -0$$

$$(0) - j\infty < \alpha < (0) \rightarrow -j\infty < \beta_{1x} < -j0 \quad and \quad -\infty < \beta_{1y} < -\beta_\rho$$

Thus

$$\beta_\rho$$

$$= \frac{1}{\pi}\int_{\beta_{1y}=-\infty}^{\beta_{1y}=+\infty} \frac{\exp[-j\beta_{1x}x]\exp\left[-j\beta_{1y}y\right](d\beta_{1x})}{\sqrt{\beta_\rho^2 - \beta_{1x}^2}}$$

Therefore, we can conclude:

$$\int_{\beta_{1y}=-\infty}^{\beta_{1y}=+\infty} \exp(-j\beta_{1x}x)\exp\left(-j\beta_{1y}y\right)\frac{1}{\beta_{1x}}d\beta_{1y} = \pi H_0^{(2)}(\beta_\rho\rho)$$

.

References:

1. Sommerfeld, Partial Differential Equations in Physics. New York: Academic (1949).
2. J. Gardner, R. E. Collin, "An accurate closed-form approximate representation for the Hankel function of the second kind," IEEE Transactions on Antennas and Propagation 48(10), 1699-1700 (2000).
3. Alù and N. Engheta, "Optical nanotransmission lines: synthesis of planar left-handed metamaterials in the infrared and visible regimes," J. Opt. Soc. Am. B 23, 571-583 (2006).
4. Hosseini, D. N. Kwong, C.-Y. Lin, B. S. Lee, and R. T. Chen, "Output Formulation for Symmetrically-Excited one-to-N Multimode Interference Coupler," IEEE J. of Sel. Topics in Quant. Elect. 6(1), 53-60 (2010).
5. Hosseini, H. Subbaraman, D. Kwong, Y. Zhang, and R. T. Chen, "Optimum access waveguide width for 1×N multimode interference couplers on silicon nanomembrane," Opt. Lett. 35, 2864-2866 (2010).
6. M. Jarrahi, R.F.W. Pease, D.A.B Miller, T. H. Lee, T.H, "Optical Spatial Quantization for Higher Performance Analog-to-Digital Conversion," IEEE Trans. Microwave Theory and Techniques 56(9), 2143-2150 (2008).

Chapter 7: Optical Beam Steering inside Chip

A summary of the final implementation

Traditionally, optical beam steering has been achieved through mechanically controlled MEMS system [1] and liquid crystal (LC) based optical phased arrays (OPAs) [2-4]. While mechanical beam steering provides high steering efficiency and relatively large scanning angle, high precision rotating stages are required, which increase the device complexity and are not potentially fast enough for high speed applications. Optical phased arrays represent an enabling technology that makes possible simple, faster, and lightweight laser beam steering with precise stabilization, random access pointing and programmable multiple simultaneous beams. LC OPAs provide rapid beam steering without expensive and complex mechanical systems but suffer from low steering speed (~10ms) and steering angle (<10º) [4]. Also, increased steering angle causes degradation of the side-lobe level and prohibitively coarse angular resolution [5].

OPAs can also be implemented using waveguide arrays. A GaAs OPA with GHz steering speed was demonstrated with a maximum steering angle of ~6º [6]. A thermo-optically controlled OPA fabricated on Silicon-on-Insulator (SOI) demonstrated steering at an angle of 2.3° at a wavelength of 1550 nm [7]. For uniform OPAs capable of large angle beam steering, an inter-element spacing of about one-half the operating wavelength is required. Despite the promises of phased waveguide arrays, strong coupling between adjacent waveguides imposes a limitation for employing such devices in practical applications if a uniform array is used.

In order to avoid optical coupling between adjacent waveguides at small inter-element spacing ($\lambda/2$, λ=1.55μm) required for large angle beam steering in uniform arrays, we choose a non-

uniform array design described in [5]. The prototype design is based on a non-uniform 12-element array, which consists of 3 four-element uniform sub-arrays, as shown in Figure 7.1(a). The spacing of each sub-array is chosen such that there is no overlap of its far-field grating lobes with those of the other two sub-arrays. Figure 7.1(b) shows the maximum allowable steering angle using linearly phased uniform arrays as a function of the inter-element spacing and also recent OPA based beam steering results.

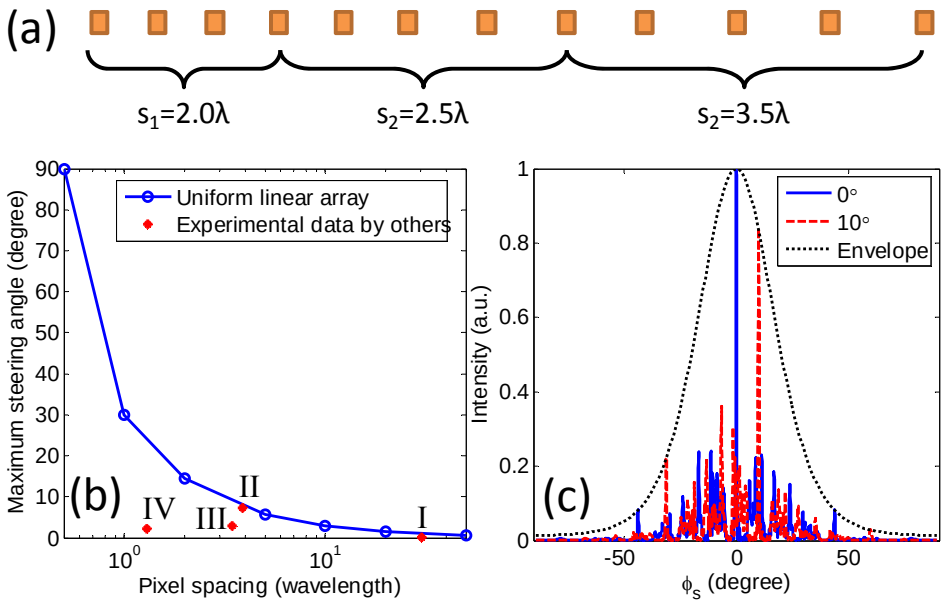

Fig. 7.1, (a) 12-element non-uniform array design with 3 sub-arrays. (b) The maximum allowable steering angle using a linearly phased uniform array as a function of the inter-element spacing. The maximum allowable angle here is defined as the steering angle at which the side-lobe-level=0dB for the first time as the beam is steered from the broadside angle (φ_0=0°). The experimental data points, I, II, III, and IV, are bi-directional beam steering angles demonstrated in [3], [8], [6], and [7], respectively. (c) Theoretical far-field pattern for a non-steered (φ_s=0°, solid blue line) and a steered (φ_0 =10°, dashed red line) beam inside the slab waveguide. The envelope (dotted back line) is the far field pattern of a single 500nm wide and 230nm thick silicon waveguide embedded in silicon dioxide.

A 1cm long silicon slab that is long enough to satisfy the far field conditions for an array size of 46.5μm is used to image the far field interference pattern from the OPA output. The end of the silicon slab serves as the imaging plane. In the far field zone, the beam steering angle inside the silicon slab (φ_s) for a linearly phased array ($\psi_n \Big/ \left|\overline{d_n}\right| = r$ for all n, ψ_n : phase applied to the nth element, $\overline{d_n}$ is the position vector of the nth element, r is a constant) is given as $r = \omega\sqrt{\mu\varepsilon_{eff}}\sin(\varphi_s)$, where ω is the angular frequency. Note that as the beam reaches the end of the slab and enters free space, its direction is changed to φ_0, which using Snell's law is $\sin(\varphi_0) = \left(\omega\sqrt{\mu\varepsilon_{eff}} \Big/ \omega\sqrt{\mu\varepsilon_0}\right)\sin(\varphi_s) = r \Big/ \left(\omega\sqrt{\mu\varepsilon_0}\right)$, where $\varepsilon_{eff} = n_{eff}^2$ and n_{eff} is the effective refractive index of propagation inside the silicon slab. It is not surprising, because this is the angle the beam would be steered at if the optical phased array was radiated into free space instead of the slab waveguide. The theoretical far field patterns for steered and non-steered beams are shown in Figure 7.1(c). Theoretical steering efficiencies are 16% and 15% at φ_0=0° and φ_0=45°, respectively [5].

A schematic of the OPA device is shown in Figure 7.2(a). The input power is uniformly divided into 12 waveguides using a 1x12 Multimode Interference (MMI) beam splitter, which has a width and length of 60μm and 553.4μm, respectively. The input and output access waveguides' widths are 2.6μm, which is the optimum value for high MMI performance [9]. The output access waveguides' widths are linearly tapered down to 0.5μm over 250μm length for single mode operation.

Active phase tuning

There are 12 independently addressed 800nm wide and 500μm long thermo-optic phase modulators to provide continuous phase tuning needed for beam steering. This provides us the advantage of being able to reset after each 2π phase shift, such as in [10], which would reduce the maximum power consumption by the heater while enabling large angle steering.

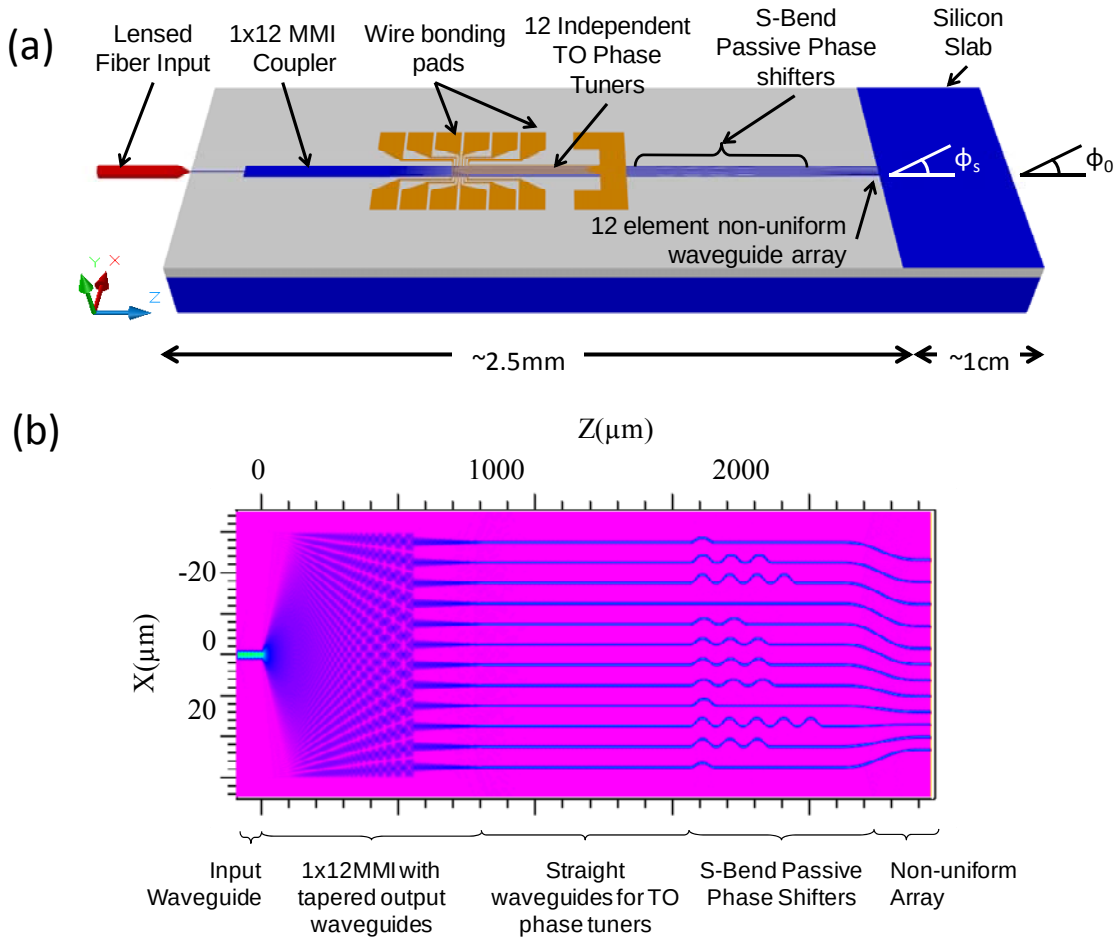

Fig. 7.2, (a) A schematic of the silicon waveguide based optical phased array. (b) Beam propagation simulation of the photonic circuit and core components.

The passive s-bend phase shifters are next, which compensate for the quadratic MMI beam splitter output phase profile [11] and change the separation of the uniform waveguide array to that of the non-uniform array at the output. The s-bend waveguides have a minimum radius of 430μm. Figure 7.2(b) shows the beam propagation simulation of the photonic circuitry.

Fabricated device

We used SOI from SOITEC with 3μm BOX and 250nm top silicon layer, which is oxidized to create an oxide etch mask, leaving a final silicon thickness of 230nm. Electron beam lithography and RIE etching is used to pattern this layer. A 1μm film of plasma-enhanced chemical vapor deposition (PECVD) silicon dioxide was deposited for top cladding. SEM pictures of the 1x12 MMI output before PECVD oxide deposition are shown in Figure 7.3(a) as well as the interface between the unequally spaced optical phased array and silicon nanomembrane slab waveguide in Figure 7.3(b). The MMI coupler was shown to have an insertion loss of 1.13dB, and uniformity of 0.72dB using TE polarized light at 1547nm [12].

After PECVD SiO_2 deposition, the metal heaters are patterned over the waveguides by e-beam lithography and alignment. Thermal evaporation and liftoff of 150nm of Cr/Au [10/140] completes the process. An SEM cross section of one completed microheater over its respective waveguide is shown in Figure 7.3(c). Note that the voids caused by the "bread loafing" of the PECVD oxide film over the waveguide are formed by proper deposition conditions, and while undesirable for electronics fabrication such as in inter-metal dielectrics (IMD), is advantageous

for this application by reducing lateral heat transfer for more efficient waveguide heating. The thermal effect of heater misalignment from the ebeam is minimized by the voids.

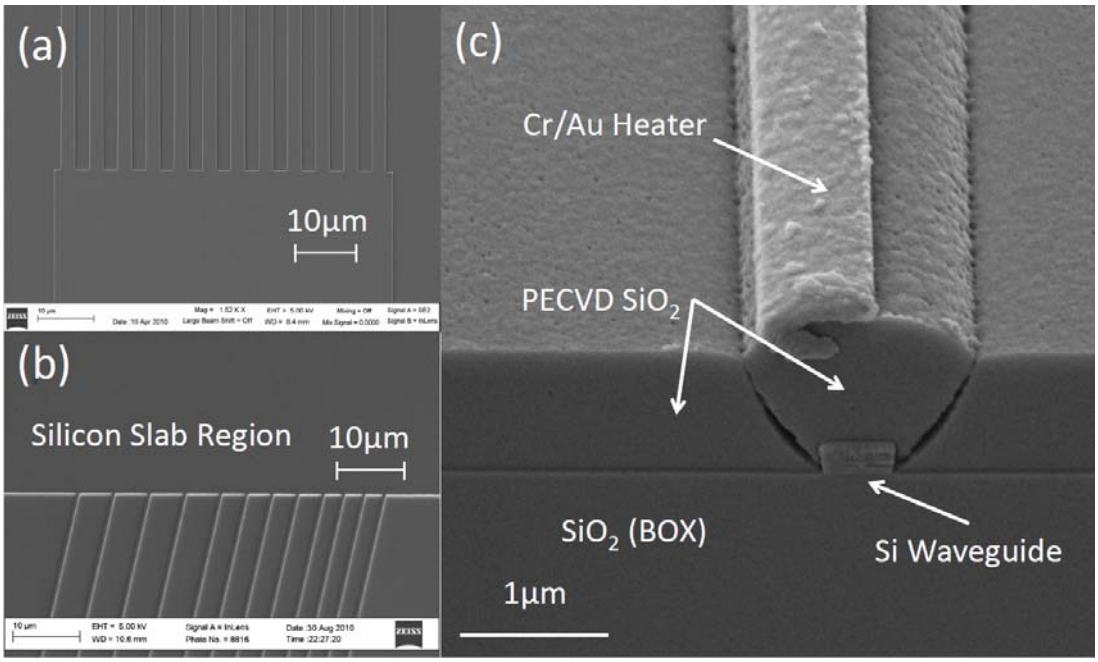

Fig. 7.3, (a) Top down SEM image of the 1x12 MMI output. (b) Tilted SEM view of the unequally spaced OPA output and silicon nanomembrane slab waveguide. (c) SEM cross section of a heater over its waveguide.

Optical test

An optical microscope picture of the heaters aligned over the output waveguides and 12 bonding pads is shown in Figure 7.4(a) and the chip carrier with the cleaved and wire-bonded device on the optical stage is shown in Figure 7.4(b).

In order to apply the correct phase shift using the thermo-optic phase shifters during active beam steering, we fabricated Mach-Zehnder (MZ) modulators to determine P_{π}, with dimensions

identical to the OPA with regard to waveguide and heater geometry and determined a switching power of P_π=12.4mW, as shown in Figure 7.5(c), along with a switching time of ~10μs.

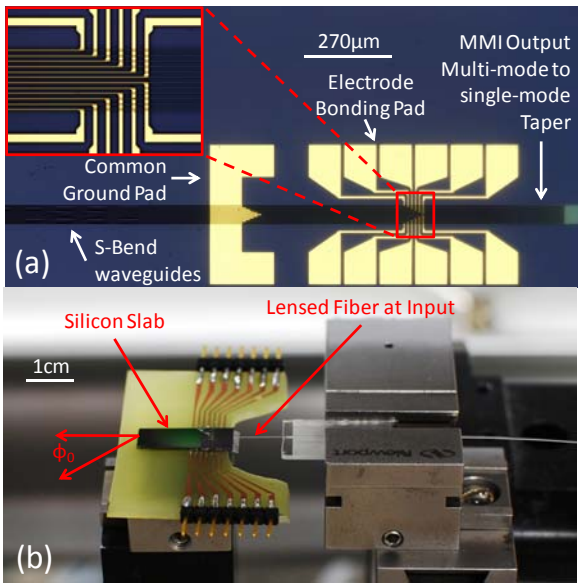

Fig. 7.4, (a) Optical microscope picture of the 12 thermo-optic heaters with bonding pads. (b) Completed device wire-bonded to chip carrier and mounted on optical stage.

TE polarized light at 1550nm from a polarization maintaining lensed fiber (PMF) with a 2.5μm output mode diameter was coupled into the waveguide input. An IR CCD camera connected to a variable objective lens captured the top-down far field image at the end of the silicon slab. Figure 7.5(a) shows such an image without any voltage applied to the heaters.

The voltage is distributed linearly proportional to the waveguide spacing from a multi-channel voltage source that can provide 12 independently controlled outputs. Figure 7.5(d) demonstrates the measured beam steering angle at the edge of the silicon slab when linear phase shift values are applied to the array element, along with the theoretical steering angles as a function of the input power to the outermost array element, which needs the largest phase shift, and are calculated

using the phase shift data from the MZ test. Despite the highly efficient thermo-optic phase shifters, the power required for beam steering becomes prohibitively large for our voltage source and limits us to steering angles of about 2.5degree inside the silicon slab.

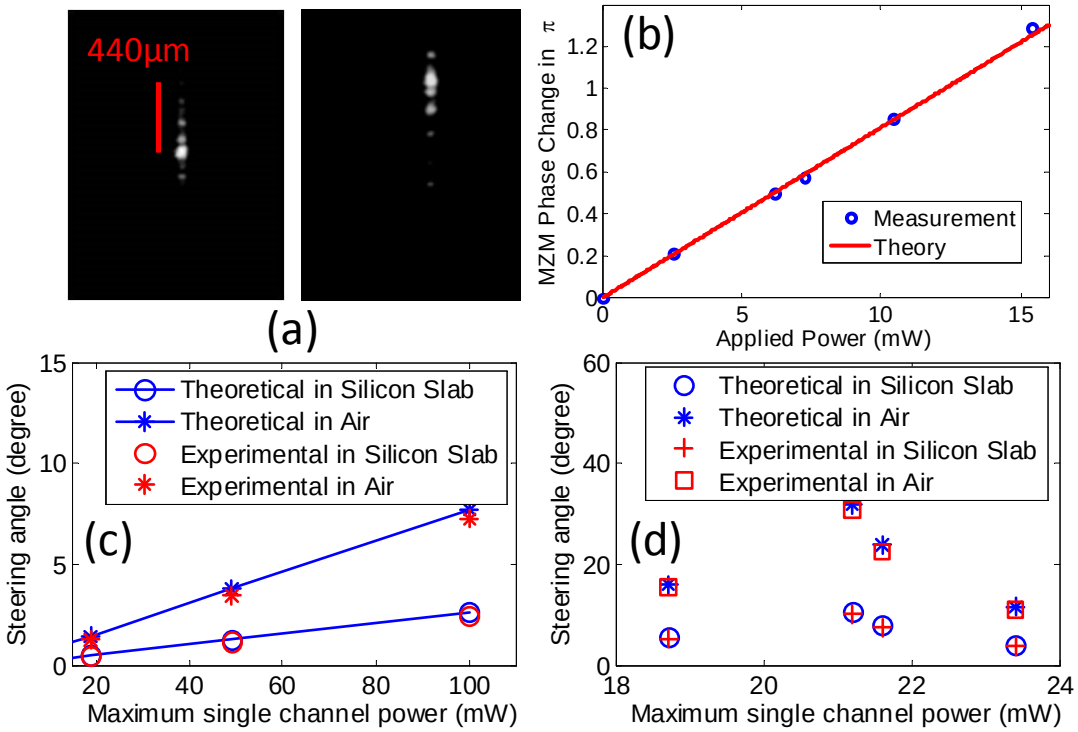

Fig. 7.5, Top down IR images of the far field viewed at the end of the silicon nanomembrane slab (a) non-steered beam, (b) beam steered at 2.5degree. (c) Electrical power vs phase change in MZM showing Pπ value of 12.4mW. Steering angle vs maximum power applied in a single channel for both the silicon slab and in air (d) without reset and (e) with reset.

A top-down IR image of the steered beam at 2.5degree is shown in Figure 7.5(b). Figure 7.5(e) shows beam steering angles achieved by applying modulo 2π phase shifts to the independently controlled electrodes. We were able to steer the beam at 10.5degee inside the silicon slab with side-lobe-level (SLL) better than 3dB, while limiting the maximum power per channel to less than P2π=24.8mW. Theoretically, we expect 3.8dB SLL at 10.5º. We believe the degradation in

the performance is due to the variation in P2π of the micro-heaters, which results in increasing inaccuracies in the applied power as the number of resets increases at larger steering angles. Note that as the beam couples out of the silicon slab into air, the steering angle is changed according to Snell' Law, where neff=2.9, as shown in Figure 7.5(d) and 7.5(e). From this, we determine that a steering angle in free space of over 30º has been achieved, which to our knowledge, is the largest reported to date using single-stage phased array systems.

Summary

In summary, we have demonstrated large angle optical beam steering in free space of over 30º using a silicon nanomembrane based unequally spaced optical phased array that relaxes the strict waveguide spacing requirement for large angle beam steering. Our optical beam steering system is fabricated on SOI using CMOS compatible processes. Phase modulation is achieved thermo-optically via the use of thin-film metal heaters that are independently controlled.

References

1. Petremand Y., Clerc P.-A., Epitaux M., Hauffe R., Noell W. and de Rooij N. F., Proc. SPIE 6715, 671502(2007).
2. McManamon P. F., Dorschner T. A., Corkum D. L., Friedman L. J., Hobbs D. S., Holz M., Liberman S., Nguyen H. Q., Resler D. P., Sharp R. C. and Watson E. A, Proc. IEEE 84(2), 268–298 (1996).
3. Wang X., Wang B., Pouch J. J., Miranda F. A., Anderson J. E. and Bos P., Opt. Eng. 43, 2769-2774 (2004).

4. Wang X., Wang B., Bos P., McManamon P. F., Pouch J. J., Miranda F. A., and Anderson J. E., J. Appl. Phys. 98, 073101 (2005).

5. Hosseini A., Kwong D. N., Zhao Y., Chen Y.-S., Crnogorac F., Pease R. F. W. and Chen R. T., IEEE J. Sel. Topics Quant. elect. 15(5), 1439-1446 (2009).

6. Jarrahi M., Pease R. F. W., Miller D. A. B. and Lee T. H., J. Vac. Sci. Technol. B 26, 2124-2126 (2008).

7. Acoleyen K. V., Bogaerts W., Jágerská J., Le Thomas N., Houdré R. and Baets R., Opt. Lett. 34, 1477-1479 (2009).

8. Gu, L., Chen, X., Jiang, W., Howley, B., and Chen, R.T., Appl. Phys. Lett., (87), 201106, 2005.

9. Hosseini A., Subbaraman H., Kwong D. N., Zhang Y. and Chen R. T., Opt. Lett. 35, 2864-2866 (2010).

10. Soganci, I.M., Tanemura, T., Williams, K.A., Calabretta, N., de Vries, T., Smalbrugge, E., Smit, M.K., Dorren, H., Nakano, Y., IEEE Photonics Technology Letters, 22(3), 143-145 (2010).

11. Hosseini A., Kwong D. N., Lin Ch.-Y., Lee B. S. and Chen R. T., IEEE J. Sel. Topics Quant. elect. 16(1), 61-69 (2010).

12. Kwong D. N., Zhang Y., Hosseini A. Liu Y. and Chen R. T., IET Electronics Letters, 46(18), 1281-1283, (2010).

Chapter 8: On the Role of Evanescent Modes and Group Index Tapering in Slow Light Photonic Crystal Waveguide Coupling Efficiency

Slow light in photonic crystal waveguides (PCWs) has been extensively studied for potential on-chip applications such as optical buffers and enhanced non-linearity due to increased light-matter interaction [1, 2]. The enhanced light-matter interaction provided by the slow light operation can be exploited, resulting in ultra-compact on-chip photonic devices [3]. Recently, over 40GHz modulation speed using the slow light mode in slot photonic crystals refilled with electro-optic (EO) polymer has been demonstrated [4]. However, the issue of large insertion losses due to strong impedance mismatch between strip waveguides and the PCW slow light mode needs to be addressed before integration of several slow light PCW devices is feasible.

Different approaches were proposed to enhance the coupling efficiency between strip waveguides and the PCW slow light mode. Optimization of the PCW termination at its interface with the access waveguides was presented in [5]. However, this approach does not enhance light coupling into the modes near the band-edge, where slow light based devices and other band-edge devices (such as [6]) operate. Demonstration of enhanced coupling by inserting a low group index (n_g) PCW between the strip waveguide and the slow light PCW (high n_g) was first presented in [7], where over 100μm of low n_g PCW

was used for efficient light coupling. Adiabatic tapering of the group index for efficient coupling was suggested [8, 9] and experimentally demonstrated [10, 11]. In these types of structures, a PCW taper is used as the coupler with its group index band engineered to change from that of the high n_g (>20) PCW to a much smaller value (n_g=4~8) over several (4~16) periods, which gives a relatively short coupler. The operating principle relies simply on reducing the light reflectance (R) at discontinuities based on the effective medium approximation $R = \left(n_{g1} - n_{g2}\right)^2 / \left(n_{g1} + n_{g2}\right)^2$, where, n_{g1} and n_{g2} are group indices of the two PCWs at either side of the discontinuity. However, using this relation in the case of hexagonal lattices (with air holes), which is the most common on-chip structure for PCWs, leads to significant underestimation of the coupling efficiency values reported before (e.g. n_{g1}=5, n_{g2}=100, T=1-R=80% [12]). It has been argued that the high transmission is due to the excitation of an evanescent mode on the high n_g side of the interface [12, 13]. The evanescent mode has amplitude comparable to that of the fundamental propagating mode, and its phase is such that it results in a small total field at the interface with the low n_g PCW to satisfy the boundary conditions. Away from the interface, however, the evanescent mode decays and the total field amplitude increases to its maximum. Note that the final field amplitude in the high n_g PCW is much larger than that in the low n_g PCW due the slow down effect. In this letter, we compare the effect of evanescent modes and group index tapering on the total coupling efficiency from a strip waveguide to a high n_g PCW. We numerically investigate the effect of PCW taper (see Fig. 8.1(a)) with different lengths and tapering profiles, including a step profile. We also

present experimental results of fabricated PCWs on a Silicon-on-Insulator (SOI) substrate.

Numerical investigation

A schematic of a strip waveguide to a high n_g PCW structure with an intermediate low n_g PCW coupling structure is shown in Fig. 8.2(a). The high n_g PCW is a W1.0 PCW ($d_0 = a\sqrt{3}$), where a=395nm is the lattice constant. Hole radii for both the PCWs is the same, r=0.26a. The width of the line defect in the PCW taper changes from d_{t1} at the interface with the high n_g PCW to d_{tN}, which is set to be $a(\sqrt{3}+0.2)$ at the interface with the strip waveguide. N is the number of periods in the PCW taper. SOI with silicon device layer thickness of 230nm is assumed. In the case of a step taper, the line defect width is constant throughout the taper, also d_{t1}= d_{t2}… =d_{tN}. In the case of adiabatic tapers, d_{ti} values assume either a linear or a parabolic profile from d_0 to d_{tN}. In the case of split tapers, $d_{t1} = ... = d_{t,N/2} = a(\sqrt{3}+0.1)$ and $d_{t,N/2+1} = ... = d_{tN} = a(\sqrt{3}+0.2)$. Note that the step taper is the same as the hetero-group velocity PCWs investigated in [7], with the difference that we consider much shorter low n_g PCW tapers (N≤16, PCW taper length <7μm).

In order to calculate the group index, we simulate the PCW band structure using 3D Plane Wave Expansion (PWE) method. Figure 8.1(b) inset shows the band structure for a W1 PCW. Figure 8.1(b) shows variations of n_g as a function of wavelength for PCWs

with various line defect widths. A gradual increase in the line defect width can be used for adiabatic tapering for the group index based on the same technique used in [9, 10, 11]. Note that further widening the line defect width [more than $a(\sqrt{3}+0.2)$] does not significantly reduce the group index in the bandwidth of interest ($20<n_g<100$).

We use 3D Finite Difference Time Domain (FDTD) simulations to calculate the coupling efficiency. In order to isolate the effect of the PCW taper from the Fabry Perot oscillations due to reflection at the input and output ports, we only simulate one port (one strip waveguide-PCW taper- high n_g PCW) as shown in Fig. 1(a). In the FDTD simulations, 12 periods of the high n_g PCW are used. We simulate the coupling transmission for step, linear, parabolic and split tapers for N=4, 8 and 16, as shown in Fig. 2. We observe that for any number of periods, the step taper results in highest transmission almost throughout the slow light region. As the number of periods in the taper increases or as the group index increases, all the taper types result in similar performance. Interestingly, the linear taper and the step taper show similar behavior in the slow light region for all N values. For N=16, when n_g>80, both linear and split tapers show a slightly better performance (~with 5%) compared to the step taper. For N=16, very close to the band edge (λ=1562.5nm), the parabolic taper outperforms the step taper.

It has been known that backscattering loss in PCWs increases as n_g^2 [14]. Furthermore, both adiabatically increasing group index in a chirped PCW on SOI substrate [15] and the transmission spectrum of GaAs PCW membranes [16] have shown that the disorder-induced scattering completely disrupt transmission for n_g>30. Therefore, for PCW based

slow-light devices, in the range of power-law governed transmission, the step taper outperforms the adiabatically and split tapered ones. From the 3D FDTD simulation results we found that step tapering for a small number for periods in the taper (N<8) has the highest coupling efficiency. The adiabatic tapers only outperform the step taper at n_g values not supported by current state of art fabrication technology, and only at longer tapers, which are not desirable in case of compact slow light PCW based devices, which are typically ~10μm long [4, 6].

Since group index tapering is not present in the step taper, the only explanation for high coupling efficiency between highly group index mismatched PCWs is provided by the existence of evanescent modes at the interface, which helps satisfy the boundary conditions without need for high reflection [13]. So, we can conclude that the effect of the evanescent mode in coupling between low n_g and high n_g PCW is more dominant than the effect of the group index tapering for practical compact devices. Note that, the possibility of reactive energy storage through the evanescent modes at the low n_g PCW and high n_g PCW interface is provided by the dramatic difference between the fundamental index guided and gap guided mode field profiles similar to the conditions of super coupling [17].

Experimental results

In order to confirm the above claim, we fabricated PCWs on SOI (SOITEC) with a 250nm top silicon layer and a 3μm buried oxide layer. A 50nm oxide layer was thermally

grown as an etching mask, consuming 20nm silicon. The length of the high n_g PCW section is 100μm in order to suppress the Fabry-Perot effect on the transmission. The pattern was transferred to the SOI through electron beam lithography system, followed by reactive ion etching. SEM pictures of fabricated devices are shown in Fig. 8.3.

The photonic crystal waveguide was tested on a Newport six-axis auto-aligning station. The light from a broadband amplified spontaneous emission (ASE) source, covering 1520~1620 nm, was TE-polarized with an extinction ratio of over 20dB and butt coupled into/out through a polarization maintaining lensed fiber with a mode diameter of 2.5μm. Transmitted light was analyzed by an optical spectrum analyzer with 0.05 nm resolution. Figure 8. 4 shows the transmission spectra of direct coupling between strip waveguide and PCW, and also coupling through step and linear PCW tapers with 8 and 16 periods. The oscillation amplitude for the direct coupling is 6dB (full swing), while it is about 3dB for coupling with either step or linear tapers, N=8 and 16. The transmission spectra are blue-shifted by about 20nms, which is due to 15nm expansion in the hole diameter. Similar to the 3D FDTD results, the step tapers slightly outperform the linear tapers in both N=8 and 16 cases. Also, as the N increases, the performance of the step and linear taper converge together.

Summary

In summary, by comparing the effect of different PCW taper profiles on transmission in the slow light region, we investigated whether group index tapering or existence of

evanescent modes at the boundary of a low n_g and a high n_g PCW has a dominant role in enhancing light coupling between strip waveguide and a PCW operating in the slow-light region. Numerical analysis and experimental measurements showed that the use of short low n_g PCW as an intermediate coupler, in which group index tapering is absent, is advantageous over adiabatically tapered PCW coupler. Our results also indicate that for an efficient coupling, a low n_g PCW coupler much shorter (compared to over 100s of microns of low n_g PCW coupler in [7]) than previously demonstrated is sufficient.

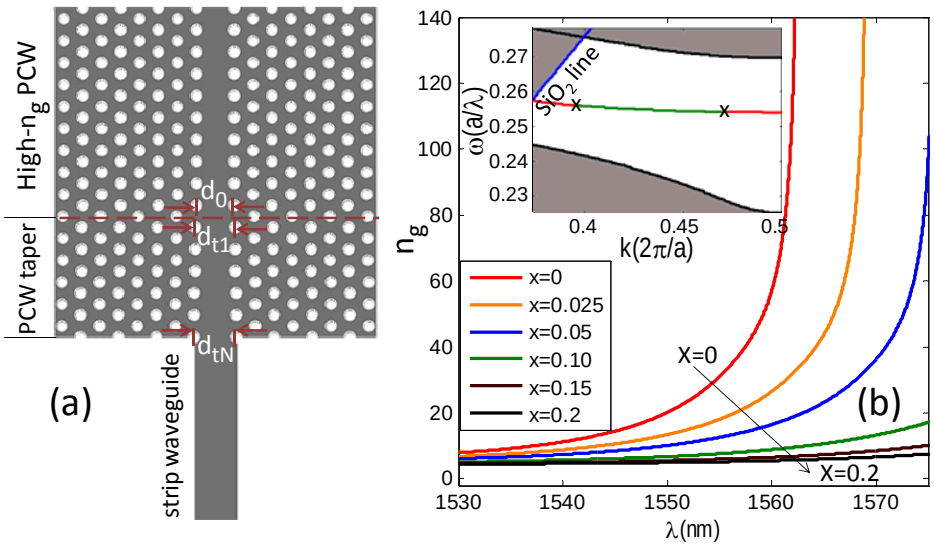

Fig. 8.1, (a) A schematic of the strip waveguide to high n_g photonic crystal waveguide coupling structure. The PCW on the right side of the interface is assumed to support high n_g propagation at the wavelength of operation. (b) Group index vs. wavelength for infinitely long PCW with different defect line widths, $d_0 = a(\sqrt{3} + x)$. The inset shows band structure for W1 PCW, r=0.26a, slab thickness=230nm, n(SiO_2)=1.45, n(Si)=3.47. The highlighted (green) section is the bandwidth over which the 20<n_g<100.

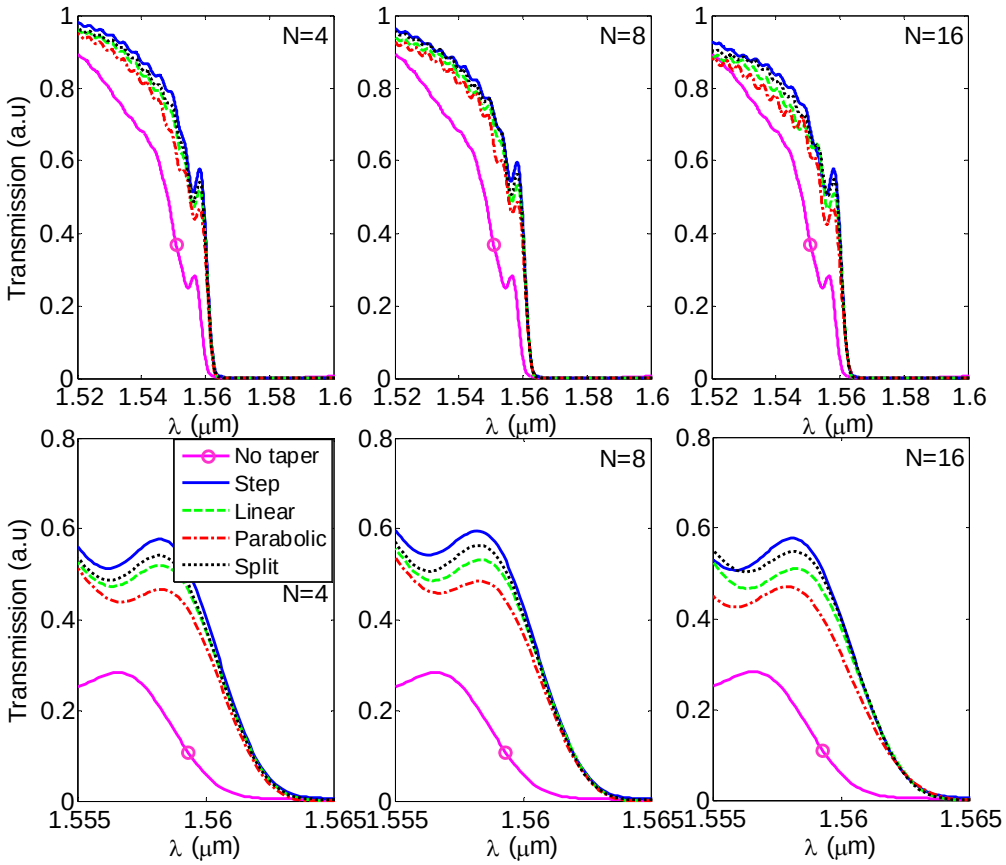

Fig. 8.2, 3D FDTD simulation results for direct coupling of strip waveguide and PC slab waveguide (no taper) and coupling through PCW tapers, with step, linear, parabolic and split profiles, for *N*=4, 8 and 16. The lower row graphs were zoomed at the band-edge region.

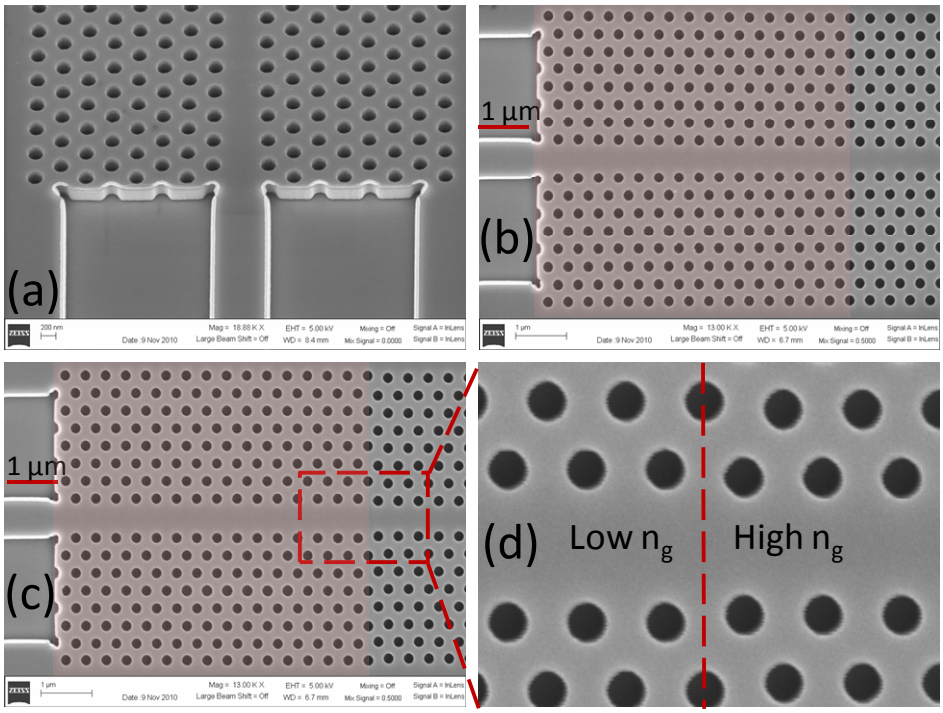

Fig. 8.3, SEM picture of fabrication PCWs butt coupled to strip waveguides, (a) a tilted view showing the silicon slab PCW, (b) 16-period linear taper, (c) 16-period step taper, and (d) interface of step taper with high n_g PCW.

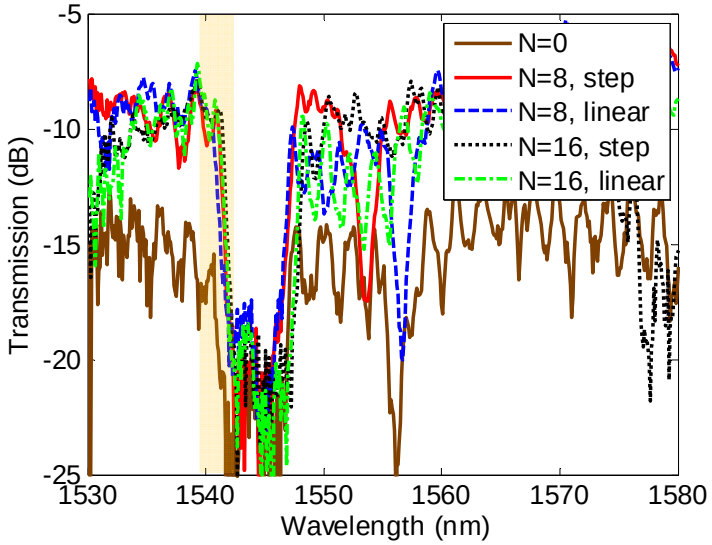

Fig. 8.4, Measurement results, transmission vs. wavelength for direct coupling of strip waveguide and PC slab waveguide (no taper) and coupling through PCW tapers, with step and linear profiles, for *N*=8 and 16. The near band-edge wavelength (slow light region is highlighted).

References

1. Robert W. Boyd, Daniel J. Gauthier, and Alexander L. Gaeta, Optics & Photonics News 17, 18 (2006).

2. Y. A. Vlasov, M. O'Boyle, H. F. Hamann, and S. J. McNab, Nature 438, 65 (2005).

3. L. Gu, W. Jiang, X. Chen, and R. T. Chen, IEEE J. Sel. Top. Quantum Electron. 14, 1132 (2008).

4. Jan Hendrik Wülbern, Stefan Prorok, Jan Hampe, Alexander Petrov, Manfred Eich, Jingdong Luo, Alex K.-Y. Jen, Martin Jenett, and Arne Jacob, Opt. Lett. 35, 2753 (2010).

5. Yurii A. Vlasov and Sharee J. McNab, Opt. Lett. 31, 50 (2006).

6. Yonghao Cui, Ke Liu, Duncan L. MacFarlane, and Jeong-Bong Lee, Opt. Lett. 35, 3613 (2010).
7. Nobuhiko Ozaki, Yoshinori Kitagawa, Yoshiaki Takata, Naoki Ikeda, Yoshinori Watanabe, Akio Mizutani, Yoshimasa Sugimoto, and Kiyoshi Asakawa, Opt. Express 15, 7974 (2007).
8. S. G. Johnson, P. Bienstman, M. A. Skorobogatiy, M. Ibanescu, E. Lidorikis, and J. D. Joannopoulos, Physical Review E 66, 066608 (2002).
9. Pierre Pottier, Marco Gnan, and Richard M. De La Rue, Opt. Express 15, 6569 (2007).
10. S. Assefa, F. Xia, W. M. Green, and Y. Vlasov, OSA in Conference on Lasers and Electro-Optics/Quantum Electronics and Laser Science Conference and Photonic Applications Systems Technologies, paper QThJ1 (2008).
11. Che-Yun Lin, Xiaolong Wang, Swapnajit Chakravarty, Beom Suk Lee, Wei-Cheng Lai, and Ray T. Chen, Appl. Phys. Lett. 97, 183302 (2010).
12. J. P. Hugonin, P. Lalanne, T. P. White, and T. F. Krauss, Opt. Lett. 32, 2638 (2007).
13. C. Martijn de Sterke, K. B. Dossou, T. P. White, L. C. Botten, and R. C. McPhedran, Opt. Express 17, 17338 (2009).
14. S. Hughes, L. Ramunno, J. F. Young, and J. E. Sipe, Phys. Rev. Lett. 94, 033903 (2005).
15. R. J. P. Engelen, D. Mori, T. Baba, and L. Kuipers, Phys. Rev. Lett. 101, 103901 (2008).
16. M. Patterson, S. Hughes, S. Combrié, N. V. Tran, A. De Rossi, R. Gabet, and Y. Jaouën, Phys. Rev. Lett. 102, 253903 (2009).
17. Andrea Alù, Mário G. Silveirinha, and Nader Engheta, Phys. Rev. E 78, 016604 (2008).

Chapter 9: Suggestions for Future Work

A summary of the accomplishments

In summary, the building blocks for an optical phased waveguide array based beam steering system were studied, modeled, fabricated and tested:

The array structure was investigated and it was shown that a non-uniform linear waveguide array can outperform liquid based optical phased arrays.

A design methodology for such non-uniform linear waveguide arrays was presented.

Multimode interference (MMI) beam splitters were investigated. Their ideal output phase profile was formulated and compared against realist waveguiding structures for high and low core/cladding index contrast.

A design methodology for on-chip high performance MMI beam splitters was presented. The results were validated by accurate Eigenmode decomposition based simulations and experimental data.

Optical and electrical parts of the OPA were designed, fabricated and characterized.

A novel far field characterization procedure for the OPA structure was developed and formulated.

Optical phase tuning using the silicon-thermo effect based was presented. The bread-loafing effect of the PECVD layer was exploited to efficiently direct the heat toward the silicon waveguides.

A complete one-dimensional OPA far field test and demonstration of large angle beam steering were presented by applying modulo-2π re-set phase shifts.

Also, a numerical and experimental investigation of the mechanism of fast light to photonic crystal waveguide slow light coupling was presented. Our results confirmed that

no group index tapering is required for an efficient coupling between two photonic crystal waveguides with large group index mismatch.

To continue this work one can demonstrate 2D optical beam steering based on multilayer optical phased arrays.

Fabrication techniques for 3D Optical phased arrays

Nanomembrane transfer printing

Transfer of semiconductor materials configured in nanoscale geometries (nanomembranes, nanoribbons, and others) can be achieved through application of rate-dependent printing techniques and suitable choice of a light interlayer adhesive [1, 2]. To affect nanomembrane transfer, following chemical undercut etching schemes designed to release the membrane from the SOI source material, an elastomeric polydimethylsiloxane-spell out (PDMS) stamp is brought into conformal contact with the nanomembrane. The stamp is rapidly retracted ($v > 1$ cm/s) off the host wafer surface, bringing the nanomembrane with it; the stamp surface can be either a flat, bulk stamp or have molded features of relief such as a line and space grating pattern [3]. Different adhesive layers such as polyimide (PI) or photodefinable epoxy (SU8) can also be used to coat the substrate and stamp [4]. After partially curing the adhesive under UV illumination, the PDMS stamp is slowly brought out of contact using micropositioning stages, transferring the nanomembrane to the substrate.

Large area silicon nanomembranes, which after lithographic patterning serve as waveguiding components in multidimensional optical phase arrays (OPA), have been

fabricated from commercially available silicon-on-insulator (SOI) source materials. SOI wafers (Soitec) having a 260nm top silicon device layer thickness, 2μm buried oxide layer, and 400μm handle layer were coated with a photoactive polymer resist (AZ 5214, 1.5μm) through spin casting at 3000 RPM for 30 seconds, followed by a 60 second bake at 110°C on a hotplate to remove residual solvent. Photolithographic patterning and development of the SOI defined the nanomembrane sheets (rectangles, 500μm × 6000μm). Optimized etch holes 10μm in diameter spaced 100μm in a square packing arrangement were patterned in the nanomembrane interior for optimized undercut release schemes. Following development, brief reactive ion etching (RIE, PlasmaTherm) utilizing SF_6 chemistries etched the exposed top layer of silicon. Control of dry etching times and plasma power are critical when fabricating nanomembrane structures to avoid notching effects in the silicon that commonly occur as a result of over-exposure to the plasma. The presence of notches in the silicon device layer can lead to crack formation or film fracture during retrieval with a bulk elastomeric stamp.

After plasma etching, the original photoresist mask was removed via sonication in acetone for 3 minutes and a brief (3 minute) piranha solution treatment. Photoresist was reintroduced to the surface using the same conditions as above and patterned to serve as an anchor and reinforcing layer during undercut etch. Wet etching with concentrated HF (49%) removed the buried oxide layer, causing the nanomembrane to sag into light contact with the remaining handle layer of silicon. Figure 9.1 provides a schematic of nanomembrane fabrication and optical images following dry etching, but prior to undercutting.

Fabricated and released nanomembranes were retrieved from the SOI substrate by bringing a piece of PDMS into conformal contact and rapidly peeling away from the surface. The non-specific van der Waals interactions between the PDMS elastomer and silicon nanomembrane were sufficient to bond the two together for removal from the substrate with high efficiency. Figure 9.2 provides optical micrographs of a nanomembrane adhered to a bulk stamp. Contacting the PDMS/Si element to a clear substrate with a light adhesive layer (Norland Optical Adhesive 61, Norland Products), curing under UV illumination, and slowly peeling back the PDMS affected transfer.

Printing efficiency was enhanced through the use of molded relief features on the bulk stamp. In the case of nanomembrane transfer, we introduced a simple line and space grating structure to the surface (30μm line width, 20μm spacing) which reduces the contact area between the stamp and silicon, corresponding to a reduction in the adhesive strength of the interface. These stamps were fabricated using well-established casting and curing techniques of soft lithography. A master template was fabricated by patterning via lithography with a photodefinable epoxy (SU-8 25, MircroChem Corp., 25μm thick) which provided the grating structure. Functionalizing the patterned surface with a vapor deposited trichlorosilane (United Chemical Technology) and thermally curing (70°C for > 2 hours) the silicone elastomer poly(dimethylsiloxane) against the template generated the desired stamp surface. A representative illustration and cross-section of a microstructured stamp with grating features is shown in Figure 9.3.

Multilayer nanomembrane stacks for device structures

One of the primary challenges in creating a multi-layered OPA is overlay error between multiple layers after the distortion of wafer that manifests due to various fabrication steps. For the OPA, the overlay error needs to be of the order of 50-100nm over a length of 500μm.

Sequential inking and printing steps following the technique prescribed above can be utilized to fabricate multilayer stacks of nanomembranes which may prove crucial for flexible manufacturing and rapid prototyping of the systems with the targeted 3D layouts. Figure 9.4 presents a proposed process flow for fabrication of complex multilayer stacks designed for OPA devices. Initially, a silicon nanomembrane (500μm × 6000μm) is transfer printed onto a target substrate which will serve as the support structure for the multilayer stacks. Deposition of a SiO_2 dielectric layer (250nm thick) via plasma-enhanced chemical vapor deposition (PECVD) provides the waveguide cladding for the first layer. Next, lift-off photolithographic patterning can be employed to generate metallic thermo-optic heating pads and electrical interconnection points. For this step, photoresist is patterned to define larger pads along the perimeter of the nanomembrane which will act as wire bonding points for external connection. Blanket electron-beam evaporation of a Ti/Au (1/150nm; Ti provides adhesion layer) and subsequent rinsing in acetone provides the metallic pads and interconnect lines to the silicon nanomembrane structure. A spin on dielectric, such as spin-on glass or polyimide, 1.5μm thick, is then coated onto the silicon/cladding/metal stack to serve as a separation layer and interlayer adhesive. Transfer printing a second silicon nanomembrane and curing the adhesive

completes the first level of OPA stack. Anisotropic dry etching of the dielectric using O_2 and CF_4 chemistries defines openings through which to contact the metallic thermal pads. Additional device layers can be constructed following sequential deposition of dielectric and metal films with lift-off patterning to define contact pads. External connection pads of each fabricated layer should not overlap with the previous layer; a minimum 250μm offset separation between pads in adjacent layers has been incorporated into these designs. After completion of multilayer assembly and patterning, electron beam lithography (EBL) can be used to define waveguides 500 nm wide and 6 mm long on top of the stack surface. Low molecular weight polymethyl methacrylate (PMMA) acts as both a photopolymer and etch mask during the waveguide formation. After development in a 1:2 solution of methyl isobutyl ketone (MIBK), anisotropic dry etching can be used to define the waveguide structures through out the various layers in the OPA stack. Cycles of reactive ion etching with different gas chemistries can be utilized to etch different materials: SF_6 plasma for silicon etching, CF_4 for oxide etching, O_2 for polymer or dielectric etching, and Cl chemistries for gold etching. Following waveguide definition throughout the stacked structure, PECVD-deposited SiO_2 can used to infill channels between the waveguides, providing structural stability, optimum device isolation, and completion of cladding layers surrounding the waveguide edges. Once infill is complete, a final photoresist patterning step and brief dip in concentrated HF allows access to the metallic connection pads which undergo wire bonding to external electrical control.

The proposed fabrication scheme is advantageous for generating self-aligned waveguides, achieving the sub-20 nm interlayer overlay registration required for high-performance device operation while minimizing potential registration errors that can occur due to limitations of traditional positioning stages in automated printing tools. Efforts are continuing to fabricate and print these multilayer stacks, configured into device format for phase array functionality.

Challenges and future efforts

Printer positioning accuracy

To address several of the fabrication and printing challenges posed by the severe alignment requirements of the stacked OPA devices, continuing efforts are focused on quantifying the limits of positioning accuracy of the automated printing tool and identifying non-visual based alignment protocols during printing. The commercially available linear stages (Aerotech, ALS20000 series) provide rated positioning accuracy and repeatability at ~500nm. However, linear encoding through control systems can reduce this motion to below the 20nm positioning requirements for overlay printed stacks. To experimentally test the accuracy of the encoder commands and resulting stage motion, a series of capacitive coupling experiments are being developed which entail direct measuring of capacitive change between high-sensitivity probes mounted in the printer toolbit. Two fixed probes (one for each x-, y- direction) provide a reference point for relative motion of additional probes tethered to the x/y-stages. Adjusting displacement of the probe distance in the ±x, ±y directions registers as small changes in

probe capacitance which can be measured and, after comparison to a calibration standard, a true distance extracted. Experiments will chart the actual distance of stage travel compared to commanded distance or position ranging from nanoscale up to micron range displacements. Independent confirmation of the travel distance will be obtained through a series of imprinting studies in which ultra-sharp (sub-micron curvature) micro-machined tips will be indented into a soft polymer or foam surface prior to and after commanded motion. Surface mapping of the substrate via scanning electron microscopy (SEM) or profilometry can measure imprint offset distances.

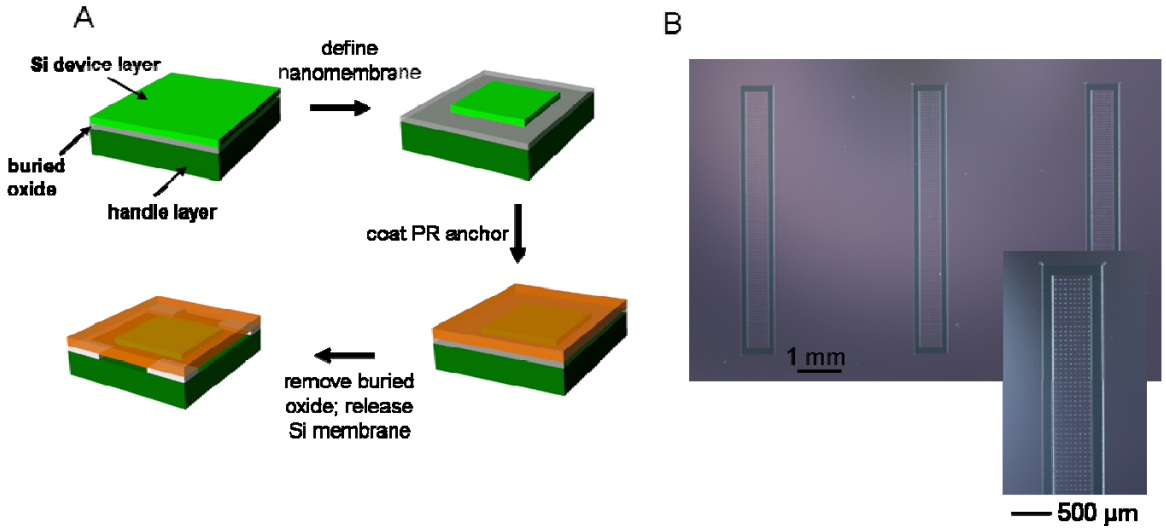

Fig. 9.1, (a) Process flow for silicon nanomembrane fabrication from an SOI source wafer. (b) Nanomembranes after dry etching, but prior to photoresist anchor and HF undercut etching.

Alignment and overlay of Si nanomembranes

Related to positioning accuracy of the automated transfer printing tool, alignment demand for each printed layer is continuing to be addressed. Current alignment protocols

depend primarily upon visual assessment and manual alignment of stages to account for position and tip/tilt accuracy. However, diffraction limited optics limits repeatable accuracy detection to ~2μm, well above the rated machine motion and waveguide design tolerances. New types of alignment procedures are being investigated for integration into the system. One such area that has attracted attention is through the incorporation of Moire pattern-based fiducial markings on the substrate or elastomeric stamps. In the simplest embodiment, arrays of fine, nanoscale parallel lines can be patterned onto a receiver substrate prior to printing the first OPA stack layer. A second set of parallel lines having the same geometry, but inclined at a slight angle can be molded into the stamp used for retrieval and printing of membranes. Proper alignment of the stamp and substrate features generate Moire patterns of alternating visible bands which can be viewed with the existing optics integrated in the printer tool, indicating alignment of the current nanomembrane with the previous layer. More advanced patterns can be utilized in similar modes for challenging printing steps.

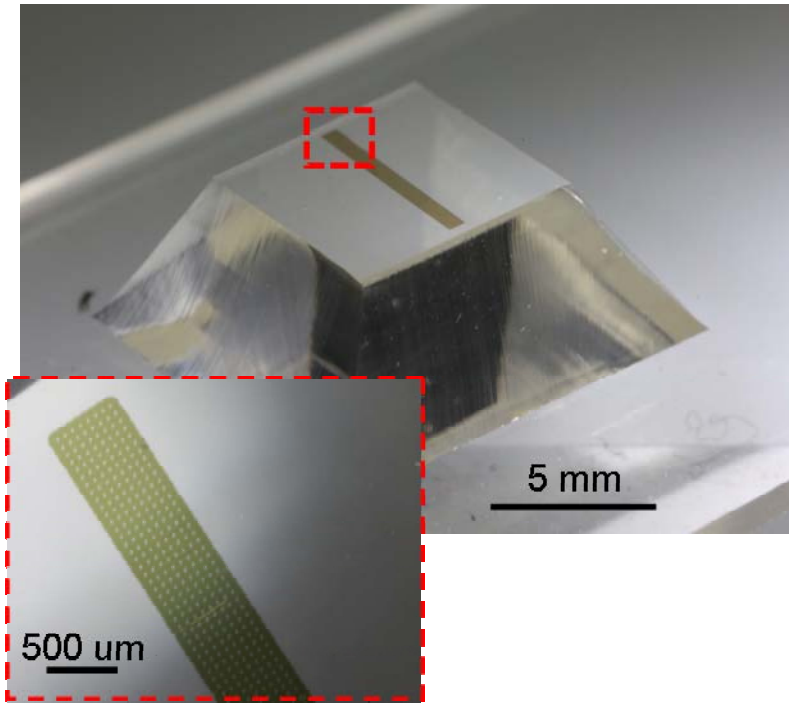

Fig. 9.2, Macro image of a retrieved nanomembrane (500 x 6000µm) on a bulk PDMS stamp.

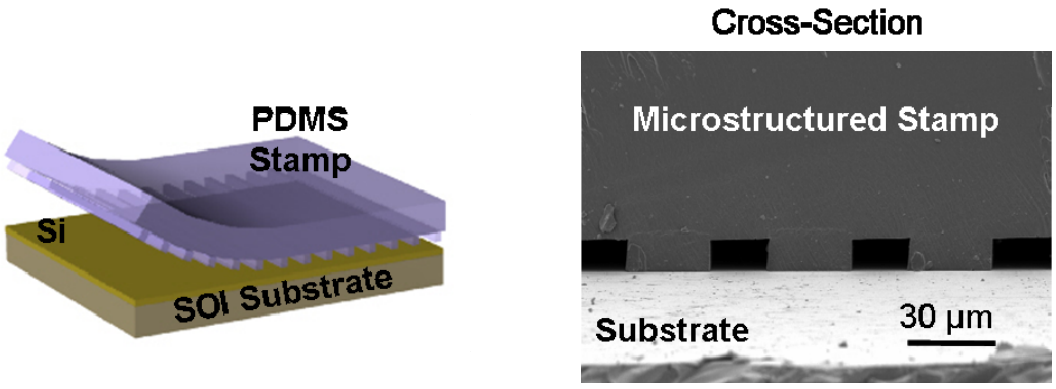

Fig. 9.3, Microstructured stamps used to enhance transfer printing featuring line and space molded surface features (30µm line width, 20µm spacing).

For the more general problem of dealing with distortion due to processing and the overlay error propagated thereby, a novel approach of adaptive nanoimprint lithography can be

pursued. In this approach, the wafer is locally heated in an optimal fashion at multiple points to correct for the distortion in real time by obtaining feedback of existing distortion. The real time system is possible to achieve by means of microchannel heat sinks using which thermal constants as low as 10ms have been demonstrated [5].

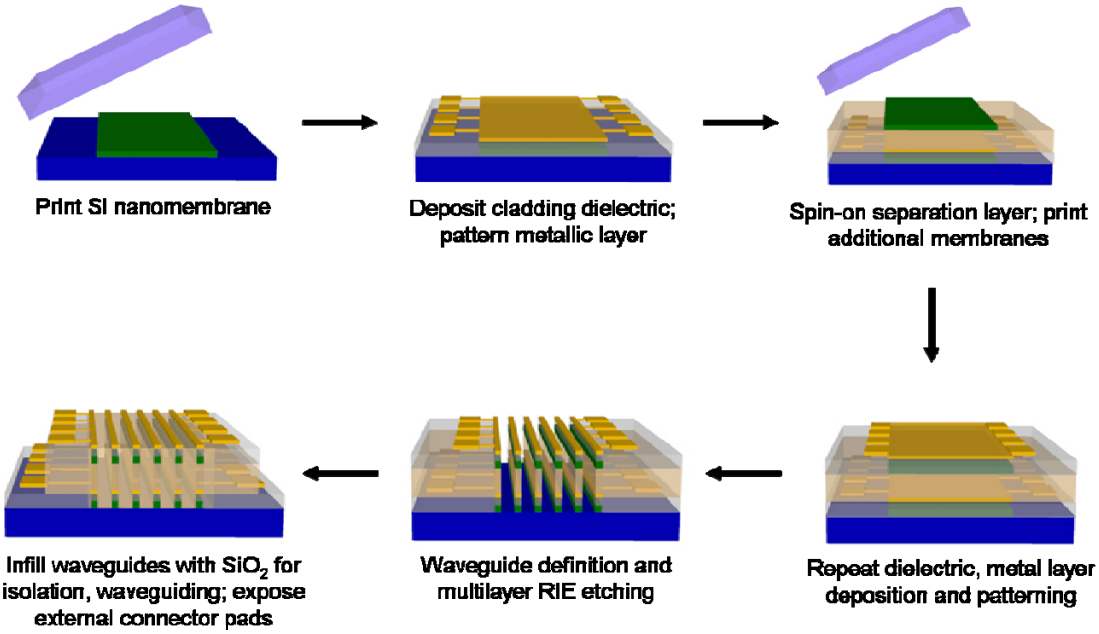

Fig. 9.4, Process flow for generating silicon nanomembrane-based device stacks for multilayer OPA structures. Process shows fabrication of a two stack device

A schematic of this novel approach is depicted in Figure 9.5. The number of microscopes needed to accurately estimate the distortion can be determined by finding the bandwidth of the distortion in spatial frequency space. The relative displacement between the wafer and the stamp can be monitored using geometric Moiré which have been shown to achieve resolution as low as 7nm [6]. The optimal heating of the wafer in order to minimize the overlay error was discussed in [7] and the results have been summarized in

Figure 9.6. Asserting the linearity of heat equation, one can consider each heater's effect separately and record the displacement (α(x,y), b(x,y)) arising from thermal expansion in the area of interest. The optimal heat inputs q_i can be obtained by solving the convex optimization problem (Figure 9.6(a)):

$$\min[\text{Squared Error}] = \min\left[\int_{\text{Area of Interest}} \left(X(x,y) + \sum_i \alpha_i q_i\right)^2 + \left(Y(x,y) + \sum_i \beta_i q_i\right)^2 dxdy\right]$$

$$\text{subject to}: q_{\text{i-heaters}} > 0$$

Figure 9.6(b) summarizes the thermal and mechanical boundary conditions used to solve the above optimization problem in the Finite Element Method (FEM) simulations. Figure 9.6(c) depicts an example of correction of an overlay error in the form of second harmonic shear strain. As the result of the strain, the RMS displacement in area of interest is 27nm and is reduced to 9nm by optimal heating of the wafer.

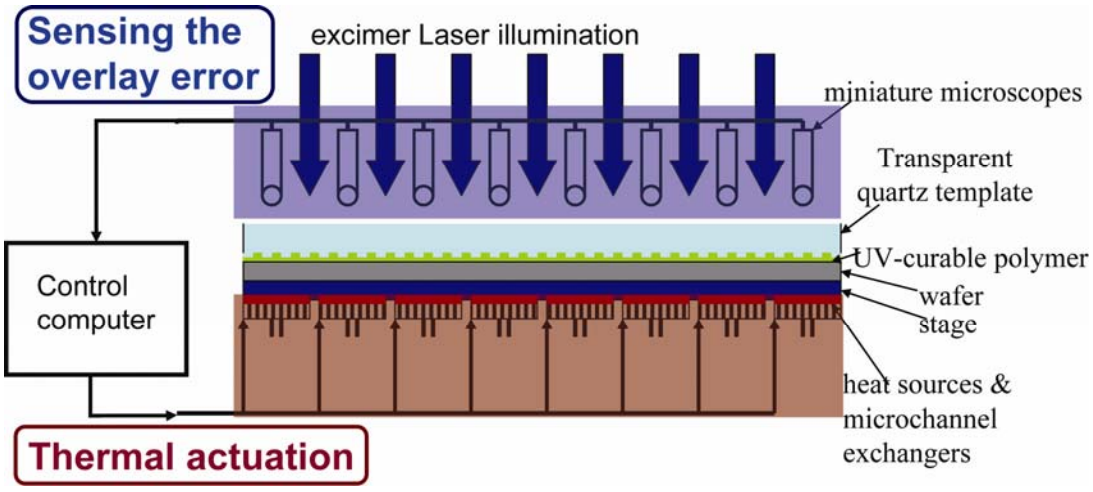

Fig. 9.5, Adaptive nanoimprint system consisting of thermal actuation and sensing subsystems. This approach takes advantage of the transparent nature of quartz template and the polymer.

Note that the output phase values can be electronically corrected. However, poor layer-to-layer alignment results in large "static" power consumption. In this case, even when the optical beam is not being steering in any direction, large power is consumed for phase correction; otherwise, large side-lobe-levels would result in extremely poor diffraction efficiency (the ratio of the power directed in the desired to the power directed in all directions). Therefore, although an electronic phase correction can be used to partially relax the layer-to-layer alignment requirement, it won't an option to fix large errors for low-power optical phased arrays, which are our targets.

Multilayer self-aligned waveguides

The process flow for waveguide self-alignment is advantageous for relaxing the overlay requirements for printing nanomembranes onto layers that have already undergone extensive fabrication and waveguide definition. However, significant engineering challenges are presented in the fabrication and etching through an as-stacked structure, as shown in the penultimate panel of Figure 9.4. The most challenging of these obstacles is expected to be the optimized etching cycles to define waveguides through all the assembled layers. Etching will create mechanically fragile structures which may not be robust to the necessary patterning and masking steps required to protect other layers of the system. Appropriate mask materials and strategies must also be developed so as to protect top device layers from continuous exposure to the different plasma etching conditions. Additionally, interlayer materials must be optimally matched for thermal and optical properties to minimize stress buildup during high temperature processing

(PECVD) and ensure good waveguideing properties. Figure 9.7 shows the results of preliminary efforts to create self-aligned waveguides. We already have the capability of bonding of single crystal silicon to create the multiple device layers [8]. Starting from a multi-bonded SOI, which has silicon, silicon nitride or silicon dioxide layers of the appropriate thicknesses [Figure 9.7(a)], vertically-aligned waveguides are fabricated through multiple cycles of etching [Figure 9.7(b)]. We have observed undercutting, especially in the silicon layers. We also noticed different waveguiding cross-section profiles in different layers. Design work and initial fabrication steps are underway to investigate and address these issues.

Summary

In this paper we presented and discussed fabrication of 3D optical phased array (OPA) devices for large angle optical beam steering. Fabrication of a single layer OPA device was presented. Potential approaches to full 3D OPA devices and our recent progresses were discussed. At the end, we reviewed the challenges and potential solutions to realization of 3D OPA devices.

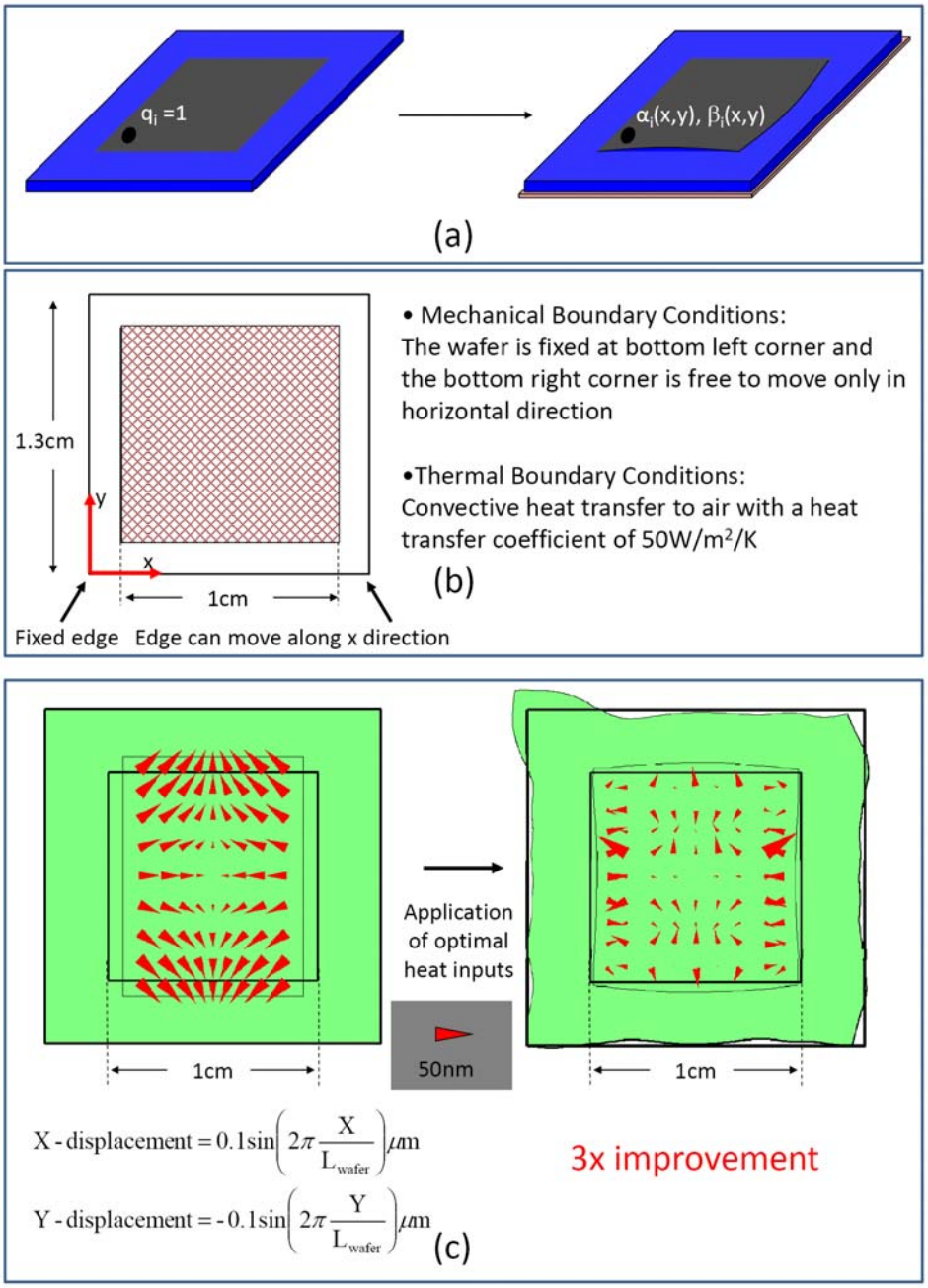

Fig. 9.6, FEM simulation results for optimal heat inputs at various localized regions on the wafer show that substantial improvement in overlay error can be achieved even in the case of shear strain. (a) The optimal heat inputs are obtained by solving a constrained convex optimization problem. (b) the boundary conditions used in the FEM simulation (c)-(e) various cases of simulated strain and the reduction achieved after application of the optimal heat inputs.

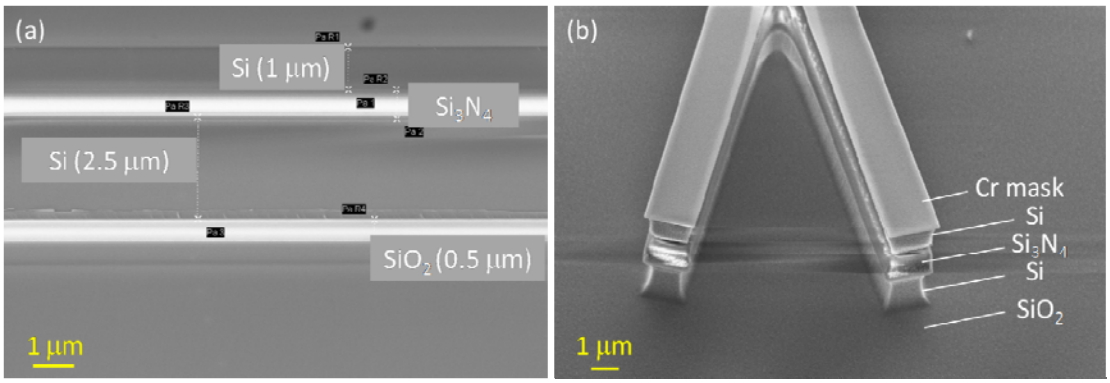

Fig. 9.7, (a) Cross sectional scanning electron micrograph (SEM), or a double bonded SOI wafer. The top dielectric is a Si_3N_4 layer, while the second is SiO_2. (b) Cross sectional SEM of a splitter realized using DBSOI wafers.

References

1. M. A. Meitl, Z.-T. Zhu, V. Kumar, K. J. Lee, X. Feng, Y. Y. Huang, I. Adesida, R. G. Nuzzo, and J. A. Rogers, "Transfer printing by kinetic control of adhesion to an elastomeric stamp." Nat. Mater. 5, 33 (2006).

2. A. J. Baca, J.-H. Ahn, Y. Sun, M. A. Meitl, E. Menard, H.-S. Kim, W. M. Choi, D.-H. Kim, Y. Huang, and J. A. Rogers, "Semiconductor wires and ribbons for high-performance flexible electronics," A ngew. Chem. Int. Ed. 47, 5524 (2008).

3. T.-H.; Kim, A. Carlson, J.-H. Ahn, S. M. Won, S. Wang, Y. Huang, J. A. Rogers, "Kinetically controlled, adhesiveless transfer printing using microstructured stamps," Appl. Phys. Lett. 94, 113502 (2009).

4. H. C. Ko, A. J. Baca, J. A. Rogers, "Bulk quantities of single-crystal silicon micro-/nanoribbons generated from bulk wafers," Nano Lett. 6, 2318 (2006).

5. D.B. Tuckerman and R.F.W. Pease, "High-performance heat sinking for VLSI," IEEE Electron Dev. Lett. 2, 126–129 (1981).
6. L. Nianhua, W. Wu, and S. Y. Chou, "Sub-20-nm Alignment in Nanoimprint Lithography Using Moiré Fringe," Nano Letters 6(11) 2626-2629 (2006).
7. S. Chandorkar and R. F. Pease, "Theoretical Analysis of Thermal Actuator Based Nanoimprint Lithography," Nanoimprint and Nanoprinting Technology Symposium (NNT), San Jose, CA, (2009).
8. F. Crnogorac and R. F. Pease, "Bonding of Semiconductor Islands for 3-D Monolithic Integrated Circuits," International Symposium on Electron, Ion and Photon Beam Technology and Nanofabrication (EIPBN), Anchorage, AK, (2010).

Publications

Accepted/Published Journal Papers

- A. Hosseini, Xiaochuan Xu, H. Subbaraman, D. Kwong, W. Jiang, and R. T. Chen, "On the Role of Evanescent Modes and Group Index Tapering in Slow Light Photonic Crystal Waveguide Coupling Efficiency," Applied Physics Letters, vol. 98, no. 3, pp. 031107, 2011
- A. Hosseini, D. Kwong, Y. Zhang, H. Subbaraman, Xiaochuan Xu, R. T. Chen, "1xN Multimode Interference Beam Splitter Design Techniques for On-Chip Optical Interconnections," IEEE Journal of Selected Topics in Quantum Electronics, to appear 2011
- A. Hosseini, V. Shabro, "Electromigration-Aware Dynamic Routing Algorithm for Network-on-Chip Applications", Int. J. of High Performance Systems Architecture, vol. 3, no. 1, pp. 56, 2011
- A. Hosseini, D. Kwong, Y. Zhang, S. A. Chandorkar, F. Crnogorac, A. Carlson, B. Fallah, S. Bank, E. Tutuc, J. Rogers, R. F. W. Pease, and R. T. Chen, "Three Dimensional Silicon-on-Insulator based Optical Phased Array for Agile and Large Angle Laser Beam Steering Systems," Journal of Vacuum Science and Technology B, vol. 28, C6O1, 2010
- A. Hosseini, H. Subbaraman, D. Kwong, Y. Zhang, R. T. Chen, "Optimum Access Waveguide Width for 1xN Multimode Interference Couplers on Silicon Nanomembrane," Optics Letters, vol. 35, no. 2864-2866, 2010
- A. Ghaffari, A. Hosseini, X. Xu, D. Kwong, H. Subbaraman, and Ray T. Chen, "Transfer of Micro and Nano-photonic Silicon Nanomembrane Waveguide Devices on Flexible Substrates," Optics Express, vol. 18, no. 19, pp. 20086-2009, 2010

- D. Kwong, Y. Zhang, A. Hosseini, R. T. Chen "1x12 Even Fanout Using Multimode Interference Optical Beam Splitter on Silicon Nanomembrane," Electronics Letters, vol. 46, no. 18, pp. 1281-1283, 2010
- A. Hosseini, J. Covey, D. N. Kwong, and R. T. Chen, " Tapered Multi-mode Interference Couplers for High Order Mode Power Extraction," Journal of Optics, vol. 12, pp. 075502, 2010
- A. Hosseini, D. N. Kwong, C.-Y. Lin, B. S. Lee, and R. T. Chen, "Output Formulation for Symmetrically-Excited one-to-N Multimode Interference Coupler," IEEE Journal of Selected Topics in Quantum Electronics, vol. 16, no. 1, pp. 61-69, 2010
- A. Hosseini, V. Shabro, "Temperature-Dependence Performance Evaluation for Single-Walled Carbon Nanotube-based Interconnects," Journal of Microelectronics Engineering, vol. 87, no. 10, pp. 1955-1962, 2010
- A. Hosseini, D. N. Kwong, and R. T. Chen, "Unequally Spaced Waveguide Arrays for Silicon Nanomembrane-Based Efficient Large Angle Optical Beam Steering," IEEE Journal of Selected Topics in Quantum Electronics, vol. 15, no. 5, pp. 1439-1446, 2009
- Y. Zhao, Y.-S. Chen, A. Hosseini, D. N. Kwong and R. T. Chen, "Delay Time Enhanced Flat Band Photonic Crystal Waveguides with Capsule-shaped Holes on Silicon Nanomembrane," IEEE Journal of Selected Topics in Quantum Electronics, vol. 15, no. 5, pp. 1510-1514, 2009
- H. Zandi, S. Khorasani, A. Hosseini, K. Mehrany, B. Rashidian and A. Adibi, "Plasmonic propagation modes of a structured two-dimensional conducting interface," Journal of Optics A: Pure and Applied Optics, vol. 10, pp. 02520, 2008

- A. Nieuwoudt, A. Hosseini, and Y. Massoud, "On the Design of Dielectric Strip Plasmonic Structures for Subwavelength Waveguiding Applications," Nanotechnology, IEEE Transactions on , vol.7, no.2, pp.189-196, 2008
- A. Hosseini, H. Nejati, and Y. Massoud, "Triangular lattice plasmonic photonic band gaps in subwavelength metal-insulator-metal waveguide structures," Applied physics letter, vol. 92, no. 1, pp. 013116, 2008
- A. Hosseini, H. Nejati, and Y. Massoud, "Modeling and design methodology for metal-insulator-metal plasmonic Bragg reflectors," Opt. Express, vol. 16, pp. 1475-1480, 2008
- A. Hosseini and Y. Massoud, "A Nano-Scale Surface Plasmon Based Resonator using Rectangular Geometry," Applied Physics Letters, vol. 90, pp. 181102, 2007
- A. Hosseini, H. Nejati, and Y. Massoud, "Design of a maximally flat optical low pass filter using plasmonic nanostrip waveguides, "Optics Express, vol. 15, pp. 15280-15286, 2007
- A. Hosseini and Y. Massoud, "Optical Range Microcavities and Filters Using Multiple Dielectric Layers in Metal-Insulator-Metal Structures," Journal of Optical Society of America A, vol. 24, no. 1, pp. 221-224, 2007
- A. Hosseini, A. Nieuwoudt, and Y. Massoud, "Optimizing Dielectric Strips Over a Metallic Substrate for Subwavelength Light Confinement," Photonics Technology Letters, IEEE , vol.19, no.7, pp.522-524, 2007
- A. Hosseini and Y. Massoud, "A Low-loss Metal-Insulator-Metal Plasmonic Bragg Reflector," Optics Express, vol .14, pp. 11318-11323, 2006

- A. Hosseini, A. Nieuwoudt, and Y. Massoud, "Efficient Simulation of Subwavelength Plasmonic Waveguides Using Implicitly Restarted Arnoldi," Optics Express, vol. 14, pp. 7291-7298, 2006

Conference Papers

- (Invited) A. Hosseini, D. N. Kwong, Y. Zhang, and Ray T. Chen, "Large Angle Beam Steering on Silicon Nanomembrane," IEEE Winter Topicals, to appear, 2011
- A. Hosseini, D. N. Kwong, Y. Zhang, and Ray T. Chen, "Far-field approximation in two-dimensional slab-waveguides," SPIE Photonics West, to appear, 2011
- Xiaochuan Xu, Harish Subbaraman, Daniel Pham, Amir Hosseini, Cheyun Lin, Yang Zhang, Xiaohui Lin, Xinyuan Dou, Ray T. Chen "Transfer and characterization of silicon nanomembrane based photonic devices on flexible polyimide substrate" SPIE Photonics West, to appear, 2011
- D. N. Kwong, Y. Zhang, A. Hosseini, and Ray T. Chen, "Integrated optical phased array based large angle beam steering system fabricated on silicon-on-insulator," SPIE Photonics West, to appear, 2011
- A. Hosseini, D. N. Kwong, H. Subbaraman, and Ray T. Chen, "Demonstration of Compact 2x2 Multimode Interference coupler on Silicon Nanomembrane, IEEE Group IV Photonics GPF 2010, Beijing, P1.25, 2010
- A. Hosseini, D. N. Kwong, and R. T. Chen, "On the Design of 1xN Multimode Interference Coupler for Photonic Integrated Circuits", IEEE/LEOS summer Topicals Meeting Series, pp. 195-196, 19-21 July 2010

- D. N. Kwong, Yang Zhang, A. Hosseini, Yazhao Liu, and R. T. Chen, "Demonstration of Rib Waveguide Based 1x12 Multimode Interference Optical Beam Splitter on Silicon-on-Insulator" IEEE/LEOS summer Topicals Meeting Series, pp. 221-222, 19-21 July 2010
- A. Hosseini, D. N. Kwong, Yang Zhang, Yazhao Liu, and R. T. Chen, "On the Optimum Design for 1xN Multimode Interference Coupler based Beam Splitters," OSA/IEEE Integrated Photonics Research, Silicon and Nano Photonics (IPR), paper JTuB9, 2010
- A. Hosseini, J. Covey, and R. T. Chen, " Mode Order Converter Using Tapered Multimode Interference Couplers", OSA/IEEE Integrated Photonics Research, Silicon and Nano Photonics (IPR), paper IWB2, 2010
- A. Hosseini, D. N. Kwong, Yazhao Liu, and R. T. Chen, "On the Design of Highly Dispersive Photonic Crystal Waveguides for Optical Delay Lines," IEEE/LEOS Winter Topicals Meeting Series, pp.120-121, 2010
- A. Hosseini, D. N. Kwong, and R. T. Chen, "Analytical formula for output phase of symmetrically excited one-to-N multimode interference coupler," SPIE Photonics West, 7607, 760718, 2010
- D. N. Kwong, Y.-Z. Liu, A. Hosseini, C.-Y. Lin, B. S. Lee, and R. T. Chen, "Silicon-integrated photonic circuit for a single-stage large-angle beam steering optical phased array," SPIE Photonics West, 7607, 760713, 2010
- N. Yasrebia, S. Khorasani, H. Karami-Taheria, B. Rashidiana, A. Hosseini, "Stable Semi-analytical Method for Analysis of Plasmonic Propagation on Periodically Patterned Metal Plates," SPIE Photonics West, 7609, 76091E, 2010

- A. Hosseini, D. N. Kwong and R. T. Chen, “Low dispersion slow light in silicon-on-insulator photonic crystal waveguide,” SPIE Photonics West, 7609, 76091A, 2010
- Y.-S. Chen, A. Hosseini, Y. Zhao, D. N. Kwong and R. T. Chen, “Modified Slab Photonic Crystal Structure for Delay Time Enhancement Using Capsule Shaped Holes”, 14th IEEE OptoElectronics and Communications Conference (OECC), 2009
- A. Hosseini, D. N. Kwong and R. T. Chen, “Wide steering angle optical phased array based on silicon nanomembrane,” SPIE Photonics West, 7221, 72210T, 2009
- A. Hosseini, Y.-S. Chen, D. N. Kwong and R. T. Chen “Silicon nano-membranes for efficient large angle optical beam steering,” IEEE/LEOS Winter Topicals Meeting Series, pp. 104-105, 2009
- A. Hosseini, T. Ragheb and Y. Massoud, “A fault-aware dynamic routing algorithm for on-chip networks,” Circuits and Systems, 2008. ISCAS 2008. IEEE International Symposium on, pp. 2653-2656, 2008
- A. Hosseini, H. Nejati and Y. Massoud, “An Analytical model for characteristic impedance in nanostrip plasmonic waveguides,” Circuits and Systems, 2008. ISCAS 2008. IEEE International Symposium on , pp. 2346-2349, 2008
- A. Hosseini and Y. Massoud, "Subwavelength Plasmonic Bragg Reflector Structures for On-chip Optoelectronic Applications," Circuits and Systems, 2007. ISCAS 2007. IEEE International Symposium on , pp.2283-2286, 2007

- A. Hosseini, H. Nejati, Y. Massoud, “Subwavelength three-dimensional Bragg filtering in integrated slot plasmonic waveguides,” Nanotechnology, 2007. IEEE-NANO 2007. 7th IEEE Conference on , pp.502-505, 2007
- A. Hosseini and Y. Massoud, “A rectangular metal-insulator-metal based nanoscale plasmonic resonator,” Nanotechnology, 2007. IEEE-NANO 2007. 7th IEEE Conference on , pp. 81-84, 2007
- M. Alam, A. Hosseini, Y. Massoud, “Impedance formulation of single oscillating nanospheres at optical frequencies,” IEEE Circuits and Systems, 2007. MWSCAS 2007. 50th Midwest Symposium on, pp. 1249-1252, 2007
- A. Hosseini, H. Nejati, Y. Massoud, “Analyzing fundamental propagation modes in V-groove plasmonic waveguides,” Nanotechnology, 2007. IEEE-NANO 2007. 7th IEEE Conference on , pp. 686-689, 2007
- A. Hosseini, H. Nejati, and Y. Massoud, “A Metal-Insulator-Metal based two-dimensional triangular lattice photonic band-gap structure, ” IEEE Circuits and Systems, 2007. MWSCAS 2007. 50th Midwest Symposium on, pp. 1253-1256, 2007
- A. Hosseini, H. Nejati, and Y. Massoud, “Design of optical range third-order Chebychev low-pass filter using plasmonic nanostrip waveguides,” IEEE Circuits and Systems, 2007. MWSCAS 2007. 50th Midwest Symposium on, pp. 1245-1248, 2007
- H. Nejati, T. Ragheb, A. Hosseini, and Y. Massoud, “A programmable input-pulse dependent chaotic oscillator,” IEEE Circuits and Systems, 2007. MWSCAS 2007. 50th Midwest Symposium on, pp. 173-176, 2007

- A. Hosseini, A. Nieuwoudt, and Y. Massoud, , “Optimizing Dielectric Strip Plasmonic Waveguides for Subwavelength On-Chip Optical Communication,” Nano-Networks and Workshops, 2006. NanoNet '06. 1st International Conference on, pp. 1-5, 2006
- A. Hosseini, A. Nieuwoudt, and Y. Massoud, “Efficient Simulation of Subwavelength Plasmonic Waveguides Using Implicitly Restarted Arnoldi,” Nanotechnology, 2006. IEEE-NANO 2006. Sixth IEEE Conference on , pp. 437-440, 2006
- A. Nieuwoudt, A. Hosseini and Y. Massoud, “On the Design of Integrated Waveguides using a Dielectric-Metal Substrate Structure for On-Chip Optical Communication,” Wireless and Microwave Technology Conference, 2006. WAMICON '06. IEEE Annual, pp. 1-5, 2006
- A. Hosseini and Y. Massoud, “Tunable Omnidirectional Resonance in Metal-Insulator-Metal Structures,” Microwave Symposium Digest, 2006. IEEE MTT-S International, pp. 1484-1487, 2006

PhD Program of Work

Sem and Year Taken	5-Digit Unique #	Dept and Course #	Official Course Title	Professor	Letter grade
Fall 08	17395	EE396K	Organic Polymer Semiconductor Devices	Prof. Ananth Dodabalapur	A
Spring 09	16755	EE383P	Optoelectronic Devices	Prof. Seth R. Bank	A
Fall 09	17270	EE383V	Nonlinear Optics	Prof. Mikhail Belkin	A
Fall 09	17265	EE383N	Theory of Electromagnetic Fields: Electrodynamics	Prof. Andrea Alu	A
Spring 10	16390	EE296K	VLSI Fabrication Techniques	Prof. Sanjay Banerjee	A
Fall 11	17015	EE383V	Electromagnetic Metamaterials	Prof. Andrea Alu	A

Bibliography

1. P. McManamon, T. Dorschner, D. Corkum, L. Friedman, D. Hobbs, M. Holz, S. Liberman, H. Nguyen, D. Resler, R. Sharp, and E. Watson, “Optical phased array technology,” Proceedings of the IEEE, vol. 84, no. 2, pp. 268–298, 1996.
2. X. Wang, B. Wang, J. Pouch, F. Miranda, J. E. Anderson, and P. J. Bos, “Performance evaluation of a liquid-crystal-on-silicon spatial light modulator”, Opt. Eng., vol. 43, pp. 2769, 2004.
3. M. Jarrahi, R. Fabian W. Pease, D. A. B. Miller, and T. H. Lee, “Optical switching based on high-speed phased array optical beam steering”, Appl. Phys. Lett., vol. 92, pp. 014106, 2008.
4. K. Van Acoleyen, W. Bogaerts, J. Jágerská, N. Le Thomas, R. Houdré, and R. Baets, “Off-chip beam steering with a one-dimensional optical phased array on silicon-on-insulator,” Opt. Lett., vol. 34, pp. 1477-1479, 2009.
5. L. Gu, X. Chen, W. Jiang, B. Howley, and R. T. Chen, “Fringing-field minimization in liquid-crystal-based high-resolution switchable gratings”, Appl. Phys. Lett., vol. 87, pp. 201106, 2005.
6. Y. Petremand, P.-A. Clerc, M. Epitaux, R. Hauffe, W. Noell, and N. F. de Rooij, “Optical beam steering using a 2D MEMS scanner”, Proc. SPIE, vol. 6715, pp. 671502, Oct. 2007.
7. P. F. McManamon, T. A. Dorschner, D. L. Corkum, L. J. Friedman, D. S. Hobbs, M. Holz, S. Liberman, H. Q. Nguyen, D. P. Resler, R. C. Sharp and E. A.Watson, “Optical phased array technology,” Proc. IEEE, vol. 84, no. 2, pp. 268–298, Feb. 1996.
8. X. Wang, B. Wang, J. Pouch, F. Miranda, J. Anderson, and P. Bos, “Performance evaluation of a liquid-crystal-on-silicon spatial light modulator,” Opt. Eng., vol. 43, pp. 2769-2774, Nov. 2004.
9. X. Wang, B. Wang, P. Bos, P. F. McManamon, J. J. Pouch, F. A. Miranda, and J. E. Anderson, “Modeling and design of an optimized liquid-crystal optical phased array”, J. Appl. Phys., vol. 98, pp. 073101, Oct. 2005.
10. P. F. McManamon, “Agile Nonmechanical Beam Steering,” Optics & hotonics News, vol.17, pp. 24-29, Mar. 2006.
11. M. Jarrahi, R. Fabian, W. Pease, D. A. B. Miller, and T. H. Lee, “High-speed optical beam-steering based on phase-arrayed waveguides”, J. Vac. Sci. Technol. B, vol. 26, pp. 2124-2126, Dec. 2008.
12. N. R. Smith, D. C. Abeysinghe, J. W. Haus, and J. Heikenfeld, “Agile wide-angle beam steering with electrowetting microprisms," Opt. Exp., vol. 14, pp. 6557-6563, 2006.

13. G. Cocorullo, M. Iodice, “Thermally induced optical beam steering in polymeric slab waveguide”. Fibres and Optical Passive Components, Proc. of IEEE/LEOS, 2005.
14. F. Xiao, W Hu, and A. S. Xu, “Optical phased-array beam steering controlled by wavelength,” App. Opt., vol. 44, no. 26, pp. 5429–543, Sept. 2005.
15. J. H. Abeles and R. J. Deri, “Suppression of sidelobes in the far feld radiation patterns of optical waveguide arrays,” App. Phys. Lett., vol. 53, no. 15, pp. 1375-1377, Oct. 1988.
16. R. J. Mailloux, Phased Array Antenna Handbook, 1993.
17. H. Schift, “Nanoimprint lithography: An old story in modern times? A review”, J. Vac. Sci. Technol. B, vol. 26, pp. 458-480, Mar. 2008.
18. J. A. Dionne, L. A. Sweatlock, H. A. Atwater, and A. Polman, “Plasmon slot waveguides: Towards chip-scale propagation with subwavelength-scale localization”, Phys. Rev. B, vol. 73, 035407, Jan. 2006.
19. Hosseini, A. Nieuwoudt, Y. Massoud, “Optimizing Dielectric Strips Over a Metallic Substrate for Subwavelength Light Confinement”, IEEE photonic Tehnol. Lett, vol. 19, no. 7, pp. 522 – 524, Apr 2007.
20. W. Peng, M. M. Roberts, E. P. Nordberg, F. S. Flack, P. E. Colavita, R. J. Hamers, D. E. Savage, M. G. Lagally, and M. A. Eriksson, "Single-crystal silicon/silicon dioxide multilayer heterostructures based on nanomembrane transfer," Appl. Phys. Lett., vol. 90, 183107, May 2007.
21. C. Maleville, T. Barge, B. Ghyselen, A. J. Auberton, H. Moriceau, and A. M. Cartier, “Multiple SOI layers by multiple Smart-Cut (R) transfers,” Proc. of IEEE International SOI Conference, Wakefield, p. 134, 2000.
22. S. J. Orfanidis, Electromagnetic Waves and Antennas, 2004.
23. Y. Vlasov and S. McNab, “Losses in single-mode silicon-on-insulator strip waveguides and bends,” Opt. Exp. ,vol. 12, pp. 1622-1631, 2004.
24. J. S. Yu, J. Y. Moon, S. M. Choi, and Y. T. Lee, “Fabrication of 1x8multimode-interference optical power splitter based on inp using ch4/h2 reactive ion etching,” Japanese Journal of Applied Physics, vol. 40, no. Part 1, No. 2A, pp. 634–639, 2001.
25. X. Wang and R. T. Chen, “Image enhanced polymer-based multimode interference coupler covering c and l bands using deeply etched air trenches,” Applied Physics Letters, vol. 90, no. 11, p. 111106, 2007.
26. L. Soldano and E. Pennings, “Optical multi-mode interference devices based on self-imaging: principles and applications,” Lightwave Technology, Journal of, vol. 13, no. 4, pp. 615–627, Apr 1995.
27. X. Chen, W. Jiang, J. Chen, L. Gu, and R. T. Chen, “20 db-enhanced coupling to slot photonic crystal waveguide using multimode interference coupler,” Applied Physics Letters, vol. 91, no. 9, p. 091111, 2007.
28. Y.-J. Chang, T. K. Gaylord, and G.-K. Chang, “Pulse response of multimode interference devices,” J. Lightwave Technol., vol. 24, no. 3, p. 1462, 2006.

29. J. Xia, J. Yu, Z. Wang, Z. Fan, and S. Chen, “Low power 22 thermooptic soi waveguide switch fabricated by anisotropy chemical etching,” Optics Communications, vol. 232, no. 1-6, pp. 223 – 228, 2004.
30. M. Paiam and R. MacDonald, “A 12-channel phased-array wavelength multiplexer with multimode interference couplers,” Photonics Technology Letters, IEEE, vol. 10, no. 2, pp. 241–243, Feb 1998.
31. M. Rajarajan, B.Rahman, T. Wongcharoen, and K. Grattan, “Accurate analysis of MMI devices with two-dimensional confinement,” Lightwave Technology, Journl of, vol. 14, no. 9, pp. 2078–2084, Sep 1996.
32. J. Huang, R. Scarmozzino, and J. Osgood, R.M., “A new design approach to large input/output number multimode interference couple rsand its application to low-crosstalk WMD routers,” Photonics Technology Letters, IEEE, vol. 10, no. 9, pp. 1292–1294, Sep 1998.
33. R. Ulrich and T. Kamiya, “Resolution of self-images in planar optical waveguides,” J. Opt. Soc. Am., vol. 68, no. 5, pp. 583–592, 1978.
34. R.M.Lorenzo, C. Llorente, and E. J. A. M. Lopez, “Improved self-imaging characteristics in i x n multimode couplers,” IEE Proc.-Oproelectron, vol. 145, no. 1, pp. 65–69, 1998.
35. R. Yin, X. Jiang, J. Yang, and M. Wang, “Structure with improved self imaging in its graded-index multimode interference region,” J. Opt. Soc. Am. B, vol. 19, no. 6, pp. 1301–1303, 2002.
36. M. Jarrahi, R. F. W. Pease, D. A. B. Miller, and T. H. Lee, “Optical switching based on high-speed phased array optical beam steering,” Applied Physics Letters, vol. 92, no. 1, p. 014106, 2008.
37. M. Jarrahi, R. F. W. Pease, and T. H. Lee, “Spatial quantized analog-to-digital conversion based on optical beam-steering,” J. Lightwave Technol., vol. 26, no. 14, pp. 2219–2226, 2008.
38. R. F. P. M. Jarrahi, D. A. Miller, and T. H. Lee, “An overview of optical phased array technology and status,” Applied Physics Letters, vol. 92, no. 014106, 2008.
39. T. Rasmussen, J. Rasmussen, and J. Povlsen, “Design and performance evaluation of 1-by-64 multimode interference power splitter for optical communications,” Lightwave Technology, Journal of, vol. 13, no. 10, pp. 2069–2074, Oct 1995.
40. Z. Li, Y. Zhang, and B. Li, “Terahertz photonic crystal switch in silicon based on self-imaging principle,” Opt. Express, vol. 14, no. 9, pp. 3887– 3892, 2006.
41. R. Ulrich and T. Kamiya, “Resolution of self-images in planar optical waveguides,” J. Opt. Soc. Am., vol. 68, pp. 583-592, 1978.
42. J.Z. Huang, R. Scarmozzino, and R.M. Osgood Jr. , “A new design approach to large input/output number multimode interference couplers and its application to low-crosstalk WDM routers ,” Photonics Technology Letters, IEEE, vol. 10, no. 9, pp. 1292-1294, 1998.

43. R. M. Lorenzo, C. Llorenle, E. J. Abril, and M. López, “Improved self-imaging characteristics in 1xN multimode couplers,” Proc. Inst. Elect.Eng. Optoelectron., vol. 145, no. 1, pp. 65–69, 1998.
44. L. Soldano and E. Pennings, “Optical multi-mode interference devices based on self-imaging: principles and applications,” J. Lightwave Technology, vol. 13, no. 4, pp. 615–627, 1995.
45. M. Rajarajan, B.Rahman, T. Wongcharoen, and K. Grattan, “Accurate analysis of MMI devices with two-dimensional confinement,” J. Lightwave Technology, vol. 14, no. 9, pp. 2078–2084, 1996.
46. A. Hosseini, D. N. Kwong, C.-Y. Lin, B. S. Lee, and R. T. Chen, “Output Formulation for Symmetrically-Excited one-to-N Multimode Interference Coupler,” IEEE Journal of Selected Topics in Quantum Electronics, vol. 6, no. 1, pp. 53-60, 2010.
47. S. Sridaran and S. A. Bhave, “Nanophotonic devices on thin buried oxide Silicon-On-Insulator substrates,” Opt. Express, vol. 18, pp. 3850-3857, 2010.
48. N. Sherwood-Droz, A. Gondarenko and M. Lipson, “Oxidized Silicon-On-Insulator (OxSOI) from bulk silicon: a new photonic platform,” Opt. Express, vol. 18, pp. 5785- 5790, 2010.
49. Y. Shi, D. Dai, and S. He, “Improved performance of a silicon-on-insulator-based multimode interference coupler by using taper structures,” Optics Communications, vol. 253, pp. 276-282, 2005.
50. R. Yin, J. Yang, X. Jiang, J. Li, and M. Wang, “Improved approach to low-loss and high-uniformity MMI devices,” Optics Communications, vol. 181, pp. 317-321, 2000.
51. Q. Wang, J. Lu, S. He, “Optimal design of a multimode interference coupler using a genetic algorithm,” Optics Communications, vol. 209, pp. 131-136, 2002.
52. D.F.G. Gallagher, T.P. Felici, "Eigenmode Expansion Methods for Simulation of Optical Propagation in Photonics – Pros and Cons." Proc. SPIE, vol 4987, pp.69-82, 2003.
53. K. Van Acoleyen, W. Bogaerts, J. Jágerská, N. Le Thomas, R. Houdré, and R. Baets, “Off-chip beam steering with a one-dimensional optical phased array on silicon-on-insulator,” Opt. Lett., vol. 34, pp. 1477-1479, 2009.
54. Sommerfeld, Partial Differential Equations in Physics. New York: Academic (1949).
55. J. Gardner, R. E. Collin, “An accurate closed-form approximate representation for the Hankel function of the second kind,” IEEE Transactions on Antennas and Propagation 48(10), 1699-1700 (2000).
56. Alù and N. Engheta, “Optical nanotransmission lines: synthesis of planar left-handed metamaterials in the infrared and visible regimes,” J. Opt. Soc. Am. B 23, 571-583 (2006).
57. Hosseini, D. N. Kwong, C.-Y. Lin, B. S. Lee, and R. T. Chen, “Output Formulation for Symmetrically-Excited one-to-N Multimode Interference Coupler,” IEEE J. of Sel. Topics in Quant. Elect. 6(1), 53-60 (2010).

58. Hosseini, H. Subbaraman, D. Kwong, Y. Zhang, and R. T. Chen, "Optimum access waveguide width for 1×N multimode interference couplers on silicon nanomembrane," Opt. Lett. 35, 2864-2866 (2010).
59. M. Jarrahi, R.F.W. Pease, D.A.B Miller, T. H. Lee, T.H, "Optical Spatial Quantization for Higher Performance Analog-to-Digital Conversion," IEEE Trans. Microwave Theory and Techniques 56(9), 2143-2150 (2008).
60. Petremand Y., Clerc P.-A., Epitaux M., Hauffe R., Noell W. and de Rooij N. F., Proc. SPIE 6715, 671502(2007).
61. McManamon P. F., Dorschner T. A., Corkum D. L., Friedman L. J., Hobbs D. S., Holz M., Liberman S., Nguyen H. Q., Resler D. P., Sharp R. C. and Watson E. A, Proc. IEEE 84(2), 268–298 (1996).
62. Wang X., Wang B., Pouch J. J., Miranda F. A., Anderson J. E. and Bos P., Opt. Eng. 43, 2769-2774 (2004).
63. Wang X., Wang B., Bos P., McManamon P. F., Pouch J. J., Miranda F. A., and Anderson J. E., J. Appl. Phys. 98, 073101 (2005).
64. Hosseini A., Kwong D. N., Zhao Y., Chen Y.-S., Crnogorac F., Pease R. F. W. and Chen R. T., IEEE J. Sel. Topics Quant. elect. 15(5), 1439-1446 (2009).
65. Jarrahi M., Pease R. F. W., Miller D. A. B. and Lee T. H., J. Vac. Sci. Technol. B 26, 2124-2126 (2008).
66. Acoleyen K. V., Bogaerts W., Jágerská J., Le Thomas N., Houdré R. and Baets R., Opt. Lett. 34, 1477-1479 (2009).
67. Gu, L., Chen, X., Jiang, W., Howley, B., and Chen, R.T., Appl. Phys. Lett., (87), 201106, 2005.
68. Hosseini A., Subbaraman H., Kwong D. N., Zhang Y. and Chen R. T., Opt. Lett. 35, 2864-2866 (2010).
69. Soganci, I.M., Tanemura, T., Williams, K.A., Calabretta, N., de Vries, T., Smalbrugge, E., Smit, M.K., Dorren, H., Nakano, Y., IEEE Photonics Technology Letters, 22(3), 143-145 (2010).
70. Hosseini A., Kwong D. N., Lin Ch.-Y., Lee B. S. and Chen R. T., IEEE J. Sel. Topics Quant. elect. 16(1), 61-69 (2010).
71. Kwong D. N., Zhang Y., Hosseini A. Liu Y. and Chen R. T., IET Electronics Letters, 46(18), 1281-1283, (2010).
72. Robert W. Boyd, Daniel J. Gauthier, and Alexander L. Gaeta, Optics & Photonics News 17, 18 (2006).
73. Y. A. Vlasov, M. O'Boyle, H. F. Hamann, and S. J. McNab, Nature 438, 65 (2005).
74. L. Gu, W. Jiang, X. Chen, and R. T. Chen, IEEE J. Sel. Top. Quantum Electron. 14, 1132 (2008).
75. Jan Hendrik Wülbern, Stefan Prorok, Jan Hampe, Alexander Petrov, Manfred Eich, Jingdong Luo, Alex K.-Y. Jen, Martin Jenett, and Arne Jacob, Opt. Lett. 35, 2753 (2010).
76. Yurii A. Vlasov and Sharee J. McNab, Opt. Lett. 31, 50 (2006).

77. Yonghao Cui, Ke Liu, Duncan L. MacFarlane, and Jeong-Bong Lee, Opt. Lett. 35, 3613 (2010).
78. Nobuhiko Ozaki, Yoshinori Kitagawa, Yoshiaki Takata, Naoki Ikeda, Yoshinori Watanabe, Akio Mizutani, Yoshimasa Sugimoto, and Kiyoshi Asakawa, Opt. Express 15, 7974 (2007).
79. S. G. Johnson, P. Bienstman, M. A. Skorobogatiy, M. Ibanescu, E. Lidorikis, and J. D. Joannopoulos, Physical Review E 66, 066608 (2002).
80. Pierre Pottier, Marco Gnan, and Richard M. De La Rue, Opt. Express 15, 6569 (2007).
81. S. Assefa, F. Xia, W. M. Green, and Y. Vlasov, OSA in Conference on Lasers and Electro-Optics/Quantum Electronics and Laser Science Conference and Photonic Applications Systems Technologies, paper QThJ1 (2008).
82. Che-Yun Lin, Xiaolong Wang, Swapnajit Chakravarty, Beom Suk Lee, Wei-Cheng Lai, and Ray T. Chen, Appl. Phys. Lett. 97, 183302 (2010).
83. J. P. Hugonin, P. Lalanne, T. P. White, and T. F. Krauss, Opt. Lett. 32, 2638 (2007).
84. C. Martijn de Sterke, K. B. Dossou, T. P. White, L. C. Botten, and R. C. McPhedran, Opt. Express 17, 17338 (2009).
85. S. Hughes, L. Ramunno, J. F. Young, and J. E. Sipe, Phys. Rev. Lett. 94, 033903 (2005).
86. R. J. P. Engelen, D. Mori, T. Baba, and L. Kuipers, Phys. Rev. Lett. 101, 103901 (2008).
87. M. Patterson, S. Hughes, S. Combrié, N. V. Tran, A. De Rossi, R. Gabet, and Y. Jaouën, Phys. Rev. Lett. 102, 253903 (2009).
88. Andrea Alù, Mário G. Silveirinha, and Nader Engheta, Phys. Rev. E 78, 016604 (2008).
89. M. A. Meitl, Z.-T. Zhu, V. Kumar, K. J. Lee, X. Feng, Y. Y. Huang, I. Adesida, R. G. Nuzzo, and J. A. Rogers, "Transfer printing by kinetic control of adhesion to an elastomeric stamp." Nat. Mater. 5, 33 (2006).
90. A. J. Baca, J.-H. Ahn, Y. Sun, M. A. Meitl, E. Menard, H.-S. Kim, W. M. Choi, D.-H. Kim, Y. Huang, and J. A. Rogers, "Semiconductor wires and ribbons for high-performance flexible electronics," A ngew. Chem. Int. Ed. 47, 5524 (2008).
91. T.-H.; Kim, A. Carlson, J.-H. Ahn, S. M. Won, S. Wang, Y. Huang, J. A. Rogers, "Kinetically controlled, adhesiveless transfer printing using microstructured stamps," Appl. Phys. Lett. 94, 113502 (2009).
92. H. C. Ko, A. J. Baca, J. A. Rogers, "Bulk quantities of single-crystal silicon micro-/nanoribbons generated from bulk wafers," Nano Lett. 6, 2318 (2006).
93. D.B. Tuckerman and R.F.W. Pease, "High-performance heat sinking for VLSI," IEEE Electron Dev. Lett. 2, 126–129 (1981).
94. L. Nianhua, W. Wu, and S. Y. Chou, "Sub-20-nm Alignment in Nanoimprint Lithography Using Moiré Fringe," Nano Letters 6(11) 2626-2629 (2006).

95. S. Chandorkar and R. F. Pease, “Theoretical Analysis of Thermal Actuator Based Nanoimprint Lithography,” Nanoimprint and Nanoprinting Technology Symposium (NNT), San Jose, CA, (2009).
96. F. Crnogorac and R. F. Pease, “Bonding of Semiconductor Islands for 3-D Monolithic Integrated Circuits,” International Symposium on Electron, Ion and Photon Beam Technology and Nanofabrication (EIPBN), Anchorage, AK, (2010).